One- and Two-Particle Correlation Functions in the Dynamical Quantum Cluster Approach

vorgelegt von

Stephan Hochkeppel

aus Haan

Würzburg 2008

Eingereicht am: 25. Juli 2008
bei der Fakultät für Physik und Astronomie

1. Gutachter: Prof. Dr. Werner Hanke
2. Gutachter: Prof. Dr. Fakher Assaad
der Dissertation

1. Prüfer: Prof. Dr. Werner Hanke
2. Prüfer: Prof. Dr. Fakher Assaad
3. Prüfer: Prof. Dr. Ralph Claessen
im Promotionskolloquium

Tag des Promotionskolloquiums: 15.09.2008

Doktorurkunde ausgehändigt am:

Abstract

This thesis is dedicated to a theoretical study of the 1-band Hubbard model in the strong coupling limit. The investigation is based on the Dynamical Cluster Approximation (DCA) which systematically restores non-local corrections to the Dynamical Mean Field approximation (DMFA). The DCA is formulated in momentum space and is characterised by a patching of the Brillouin zone where momentum conservation is only recovered between two patches. The approximation works well if k-space correlation functions show a weak momentum dependence.

In order to study the temperature and doping dependence of the spin- and charge excitation spectra, we explicitly extend the Dynamical Cluster Approximation to two-particle response functions. The full irreducible two-particle vertex with three momenta and frequencies is approximated by an effective vertex dependent on the momentum and frequency of the spin and/or charge excitations. The effective vertex is calculated by using the Quantum Monte Carlo method on the finite cluster whereas the analytical continuation of dynamical quantities is performed by a stochastic version of the maximum entropy method. A comparison with high temperature auxiliary field quantum Monte Carlo data serves as a benchmark for our approach to two-particle correlation functions. Our method can reproduce basic characteristics of the spin- and charge excitation spectrum. Near and beyond optimal doping, our results provide a consistent overall picture of the interplay between charge, spin and single-particle excitations: a collective spin mode emerges at optimal doping and sufficiently low temperatures in the spin response spectrum and exhibits the energy scale of the magnetic exchange interaction J. Simultaneously, the low energy single-particle excitations are characterised by a coherent quasiparticle with bandwidth J. The origin of the quasiparticle can be quite well understood in a picture of a more or less antiferromagnetic ordered background in which holes are dressed by spin-excitations to allow for a coherent motion. By increasing doping, all features which are linked to the spin-polaron vanish in the single-particle as well as two-particle spin response spectrum.

In the second part of the thesis an analysis of superconductivity in the Hubbard model is presented. The superconducting instability is implemented within the Dynamical Cluster Approximation by essentially allowing U(1) symmetry breaking baths in the QMC calculations for the cluster. The superconducting transition temperature T_c is derived from

the d-wave order parameter which is directly estimated on the Monte Carlo cluster. The critical temperature T_c is in astonishing agreement with the temperature scale estimated by the divergence of the pair-field susceptibility in the paramagnetic phase. A detailed study of the pseudo and superconducting gap is continued by the investigation of the local and angle-resolved spectral function.

Kurzfassung

In der vorliegenden Arbeit wird das zwei-dimensionale Hubbard Modell im Bereich stark wechselwirkender Elektronen mit Hilfe der Dynamischen Cluster Approximation (DCA) untersucht. Im Rahmen der DCA wird das gegebene Gitter-Problem auf einen Cluster, der selbst-konsistent in einem effektiven Medium eingebettet ist, abgebildet. Somit stellt die DCA eine Erweiterung zur Dynamischen Molekularfeld-Theorie dar, indem nicht-lokale Korrelationen berücksichtigt werden.

Ein Ziel dieser Arbeit stellt die Untersuchung von dynamischen Korrelationsfunktionen für das Hubbard Modell dar. Dazu wird die Dynamische Cluster Approximation auf die Untersuchung von Zwei-Teilchen Korrelationsfunktionen erweitert. Der volle irreduzible Zweiteilchen-Vertex mit drei Impulsen und Frequenzen wird durch einen effektiven Vertex, dessen Impuls und Frequenzabhängigkeit durch das Spin- bzw. Ladungs-Anregungsspektrum gegeben ist, approximiert. Der effektive Vertex wird mit Hilfe der Quanten Monte Carlo Technik auf einem endlichen Cluster bestimmt, wobei die dynamischen Größen durch eine stochastische Version der Maximum Entropie Methode auf die reelle Frequenz-Achse analytisch fortgesetzt werden. Ein Vergleich mit dem gewöhnlichen BSS Quanten Monte Carlo Verfahren dient als Maßstab für unsere Näherung der Zwei-Teilchen Korrelationsfunktionen. Der Vergleich zeigt auf, dass unsere Methode grundlegende Eigenschaften des Spin- und Ladungs-Anregungsspektrums reproduzieren kann. Für optimale bzw. höhere Dotierungen erhalten wir ein übereinstimmendes Gesamtbild zwischen Ladungs-, Spin-, und Ein-Teilchen-Anregungsspektrum: bei optimaler Dotierung und hinreichend niedriger Temperatur tritt eine kollektive Spin-Mode im Spin-Anregungsspektrum auf und zeigt einen Energiezweig mit der Energieskala J, wobei J die magnetische Austauschenergie beschreibt. Gleichzeitig werden die Niederenergie-Anregungen im Ein-Teilchen-Spektrum durch ein Quasiteilchenband mit Bandbreite J beschrieben. Der Ursprung des Quasiteilchens lässt sich durch das Bild eines mehr oder weniger geordneten antiferromagnetischen Hintergrundes erklären, in dem sich Löcher umgeben von einer Wolke von Spin-Anregungen kohärent durch das Gitter bewegen. Bei zunehmender Dotierung verschwinden sowohl im Ein-Teilchen, als auch im Zwei-Teilchen Spin-Spektrum alle Anzeichen, die im Zusammenhang mit der Niederenergie-Skala J und dem oben beschriebenen Spin-Polaron stehen. Die Änderung der Dotierung führt des weiteren zu einem Transfer von spektralem

Gewicht im Ein-Teilchen Spektrum, der sich ebenfalls im Ladungs-Anregungsspektrum bemerkbar macht.

Im zweiten Teil der Arbeit wird eine Analyse über die supraleitenden Eigenschaften des Hubbard Modells präsentiert. Die supraleitende Instabilität wird im Rahmen der Dynamischen Cluster Approximation durch die Implementierung eines $U(1)$-Symmetrie brechenden Mediums in der Monte Carlo Rechnung für den Cluster berücksichtigt. Die supraleitende Übergangstemperatur T_c wird von dem Wert des auf dem Cluster bestimmten d-Wellen Ordnungsparameters abgeleitet. Die kritische Temperatur T_c ist in überraschend guter Übereinstimmung mit der Energieskala, die durch eine Divergenz der Paarfeld-Suszeptibilität in der paramagnetischen Phase bestimmt worden ist. Die Temperaturabhängigkeit der Pseudo- und supraleitenden Lücke wird mit der Bestimmung der Zustandsdichte und der Impuls-aufgelösten Spektralfunktion untersucht. Im Gegensatz zur der Herausbildung einer supraleitenden Lücke unterhalb der Sprungtemperatur, kann die Bildung einer Pseudo-Lücke in der Impuls-abhängigen Spektraldichte nicht aufgelöst werden.

6

Contents

Introduction

1

The theoretical description of strongly correlated electron systems represents one of the greatest challenges in condensed matter theory. Such systems exhibit a variety of phenomena, e.g. stripe phases, high temperature superconductivity, magnetism and Mott metal-insulator transitions. The reason for this manifold behaviour has its roots in the many-body correlation effects between the interacting particles where the interaction strength is of the same magnitude or larger than the kinetic energy. This situation makes a perturbative handling of the interacting states around the non-interacting limit very difficult or even impossible.

In the last few years, many non-perturbative numerical approaches have been formulated and investigated to get to the bottom of the interplay effects in correlated electron systems. A large group of solvers based on the renormalisation group technique have been applied to one dimensional systems. The Density Matrix Renormalisation Group, for example, proves greatly successfully when it is applied to resolve small energy scales. The application of renormalisation techniques to problems in higher dimensions still remains unclear and is a subject of current research. Two dimensional systems represent a wide area of application for exact diagonalisation techniques and Quantum Monte Carlo methods which represent a well-controlled access to many-body problems. Unfortunately, these methods also reveal a down side. Diagonalisation approaches are restricted to very small system sizes (up to 12 sites) because the electronic degrees of freedom grow rapidly with increasing system size. On the other hand, auxiliary field Quantum Monte Carlo studies suffer from the notorious minus sign problem, which prohibits, in general, the investigation of the low-temperature physics of correlated electron systems. Both methods are restricted to finite clusters and therefore one has to take finite size effects into account, which corrupt the investigation of the low energy excitations or competing phases in the many-body systems.

A new generation of approaches was initiated by the Dynamical Mean-Field Theory which avoids the above mentioned problems. The so-called quantum cluster theories map the original many-body problem onto a finite size quantum cluster embedded in a self-consistently determined host. The physics on the cluster is treated exactly and correlations on longer

length scales are taken into account at mean-field level. One representative of the quantum cluster theories is the Dynamical Cluster Approximation (DCA).

This thesis is organised as follows:

In chapter 2.1 we introduce the basic concepts of the Dynamical Cluster Approximation (DCA) by considering it as an extension to the Dynamical Mean-Field Theory (DMFT) where the original lattice problem is mapped onto a Periodic Anderson Impurity Model (PAM). The impurity problem can be solved in an exact way by using the Hirsch-Fye quantum Monte Carlo algorithm. For this purpose, we introduce, in section 2.7.1, a Hubbard Stratonovich (HS) field which splits the two-particle interaction term of the impurity sites into one particle operators coupled to the HS field. The summation over the HS field configurations is carried out by the Metropolis algorithm.

The Hirsch-Fye algorithm only provides correlation functions in imaginary time. In order to compare the numerical results with experimental data a method is needed to analytically continue the data from the imaginary time axis to the real frequency axis. This problem boils down to the inversion of a Laplace transformation. A straightforward inversion would lead to inconsistent results due to numerical instabilities. A state of the art technique for this continuation problem is the Maximum entropy method which is presented in chapter 3.

Chapter 4 is dedicated to the tight-binding Hubbard model which is intensively studied in this work. The Hubbard model is one of the simplest models that takes the kinetic energy and the electron-electron repulsion in a many-body system into account. It consists of a kinetic part, where electrons can gain energy by hopping between nearest-neighbour sites, and a Coulomb term, which enforces an energy penalty if two electrons occupy the same site. Although this model has a very simple structure, an analytical solution has only been found in one dimension.

In chapter 5 we investigate the dynamical properties of the Hubbard model within the Dynamical Cluster Approximation. In this sense, we have to extend the Dynamical Cluster Approximation to two-particle response functions in order to achieve a deeper insight beyond the scope of the one-particle level. The idea of our approximation and its application is described in detail.

In chapter 6 we apply the DCA to the Hubbard model and incorporate an instability to a superconducting state. The theoretical investigation of superconductivity in the Hubbard model has been pushed immensely by the discovery of the high-temperature superconductors in 1986 by Bednorz and Müller. Soon after their discovery, theorists and experimentalist have tried to find an explanation of the physics of these materials. But after more than fifteen years, the microscopic mechanism is still an open question. In our investigation, we focus on the temperature and doping dependence of the superconducting phase as well as on the occurrence of a pseudogap.

The thesis finishes with a summary of the main results.

Dynamical Cluster Approximation

<div style="text-align: right; font-size: xx-large;">2</div>

Mean-field theories started their triumphant procession many years ago. In the year 1907, P. Weiss implemented the Curie-Weiss mean-field theory for spin systems by mapping the complex lattice problem onto a magnetic impurity which is self-consistent embedded in an averaged magnetic field produced by the remaining spins. Hereby, non-local fluctuations as well as temporal fluctuations have not been taken into account. The idea of the reduction of a given lattice problem to an impurity problem, which is embedded in a self-consistent bath, was refreshed by spectacular works of Metzner and Vollhardt and Müller-Hartmann as they introduced the so-called Dynamical Mean-Field Approach (DMFA) [1, 2]. The authors showed, that in the limit of infinite dimension, the self-energy becomes purely local and the many body problem can be mapped onto a single site impurity Anderson model (SIAM). The local character of the self-energy yields from the scaling behaviour of the hopping element $t_{ij} \propto D^{-1/2}$ with the dimensionality D. It can be easily shown, that any two-sites in the expansion of the compact diagrams of the self-energy, which are connected at least with two different paths, collapse to a single site in the limit of infinite dimension [3].

Thus, the dynamical mean field approach exhibits an exact solution for infinite dimensional Hubbard-type models. In contrast to the Curie-Weiss mean-field, the DMFA consist of a frequency dependent bath, and therefore, temporal correlations can be taken into account. Nevertheless, spatial fluctuations are beyond its abilities. These correlation are only treated at mean-field level, whereas the local part of the problem (the impurity problem) can be solved exactly via quantum Monte Carlo methods.

The DMFA can be also understood as a coarse graining approximation which can be seen in the language of the diagrammatic expansion of the self-energy. In this context, we consider the Laue function which enforces momentum conservation at each vertex of the diagrammatic expansion:

$$\Delta(\boldsymbol{k}_1, \boldsymbol{k}_2, \boldsymbol{k}_3, \boldsymbol{k}_4) = \sum_{\boldsymbol{r}} \exp[i\boldsymbol{r} \cdot (\boldsymbol{k}_1 + \boldsymbol{k}_2 - \boldsymbol{k}_3 - \boldsymbol{k}_4)], \tag{2.1}$$

where $\boldsymbol{k}_1$ and $\boldsymbol{k}_2$ ($\boldsymbol{k}_3$ and $\boldsymbol{k}_4$) are the incoming (outgoing) momenta at every vertex. In

the limit of infinite dimension, the $\boldsymbol{k}$-dependence of the Laue function breaks down and corrections occur only in the order of $1/D$ [4]:

$$\Delta_{D\to\infty}(\boldsymbol{k}_1, \boldsymbol{k}_2, \boldsymbol{k}_3, \boldsymbol{k}_4) = 1 + \mathcal{O}(1/D). \tag{2.2}$$

The DMFA assumes that $\Delta_{DMFA}(\boldsymbol{k}_1, \boldsymbol{k}_2, \boldsymbol{k}_3, \boldsymbol{k}_4) = 1$ is already valid at finite dimensionality. The consequence is a violation of momentum conservation at each vertex and a collapse of the $\boldsymbol{k}$-dependence of the self-energy, which causes the local character of the self-energy. This implies, that the Green functions are replaced by a coarse-grained Green function averaged over the entire Brillouin zone:

$$\bar{G}(i\omega_m) = \frac{1}{N} \sum_{\boldsymbol{k}} G(\boldsymbol{k}, i\omega_m). \tag{2.3}$$

In the last years, the dynamical mean-field approach has been applied to a broad variety of several spin systems as well as to systems of correlated electrons and bosons [3]. Due to the local character of the theory, a detailed investigation of non-local quantities, i.e. non-local order parameters, localisation in disordered systems or spin waves in spin systems, is impossible. The following section summarises a systematic extension of the DMFA which remains fully causal and takes non-local fluctuations into account [5, 6].

2.1 Formalism

The Dynamical Cluster Approximation (DCA) represents a natural expansion of the DMFA which additionally takes non-local fluctuations into account and systematically restore momentum conservation. It was first proposed by M. Jarrell et al. [7, 8]. In the DCA, the original many-body problem is mapped on a finite size quantum cluster embedded in a self-consistently determined host. The best way to understand the approximation is in the momentum space. The coarse graining of the Green function is, as opposed to the DMFA, only performed on a finite cluster in the first Brillouin zone. A typical clustering is depicted in Fig. 2.1. The reciprocal space, which contains N k-points, is divided into N_c patches, where each patch is labelled by the cluster momentum vector $\boldsymbol{K}$, i.e., in Fig. 2.1 the number of clusters is $N_c = 4$ and L_c determines the linear size of the cluster. An arbitrary momentum vector $\boldsymbol{k}$ can be formulated as a sum of an inter-cluster momentum vector $\boldsymbol{K}$ and an intra-cluster vector $\tilde{\boldsymbol{k}}$. The intra-cluster vectors $\tilde{\boldsymbol{k}}$ represent the reciprocal vectors of $\tilde{\boldsymbol{x}}$ which form a superlattice in real space (see Fig. 2.1) and every real space lattice vector can be decomposed into a superlattice vector $\tilde{\boldsymbol{x}}$ and an intra-lattice vector $\boldsymbol{X}$, i.e. $\boldsymbol{x} = \tilde{\boldsymbol{x}} + \boldsymbol{X}$. The number of lattice sites within a real space cluster is given by N/N_c.

In the limit of $N_c = 1$, the original lattice problem is mapped onto a single impurity problem which is equivalent to the DMFA. Is N_c larger than one, then non-local corrections of the length $\sim \pi/\Delta k$ are introduced. This shows us, that the approximation works well when only correlations on short length scales in real space play the dominant role.
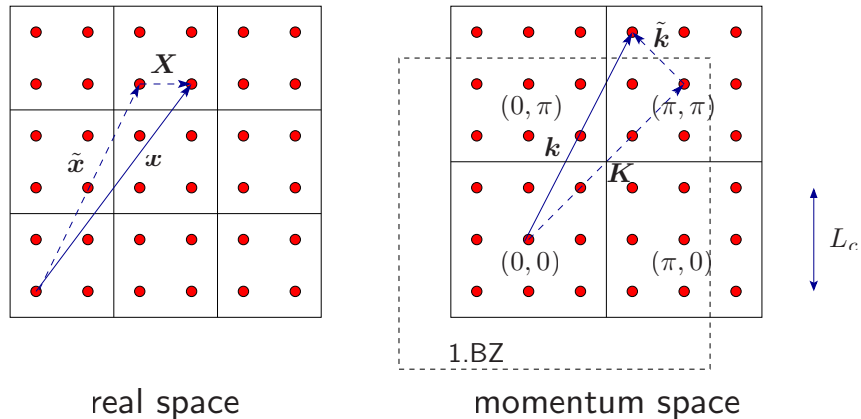
Figure 2.1 *Left: Sketch of DCA cluster patches in real space. Right: division of the Brillouin zone into $N_c = 4$ DCA patches.*

2.2 A diagrammatic derivation

In the following, we are going to present a diagrammatic derivation of the DCA. In Sec. 2.1, we introduced a segmentation of the Brillouin zone in N_c patches of length $\Delta k = 2\pi/aL_c$, where a is the lattice constant. Momentum conservation is now only recovered between two patches, which is the case if the momentum transfer k is larger than Δk. The relaxation of the momentum conservation can be accommodated for by the Laue function $\Delta(\boldsymbol{k}_1, \boldsymbol{k}_2, \boldsymbol{k}_3, \boldsymbol{k}_4)$. Therefore, we consider a function M which maps a given momentum vector $\boldsymbol{k}$ to the corresponding cluster momentum vector $\boldsymbol{K}$:

$$M: \ \mathbb{R}^2 \to \mathbb{R}^2, \ M(\boldsymbol{k}) = \boldsymbol{K} \tag{2.4}$$

Hence, we can rewrite the Laue function in the following form:

$$\begin{aligned}
\Delta(\boldsymbol{k}_1, \boldsymbol{k}_2, \boldsymbol{k}_3, \boldsymbol{k}_4) \quad &\to \quad \Delta_{DCA}(\boldsymbol{k}_1, \boldsymbol{k}_2, \boldsymbol{k}_3, \boldsymbol{k}_4) \\
&= \sum_{\boldsymbol{r}} \exp[i\boldsymbol{r} \cdot (M(\boldsymbol{k}_1) + M(\boldsymbol{k}_2) - M(\boldsymbol{k}_3) - M(\boldsymbol{k}_4))].
\end{aligned} \tag{2.5}$$

In the limit of an infinite number of cluster patches, the function M reduces to the identity function and the DCA becomes exact.

The approximation of the Laue function has an influence of every diagram in the skeleton expansion of the generating functional Φ[1]. In Fig. 2.2, we show a second-order term of the generating functional of the Hubbard model. The undulating lines represent the Coulomb interaction U and the solid lines are lattice (coarse-grained) single-particle Green functions. With the choice of the DCA Laue function Δ_{DCA}, the momenta of each internal leg propagator may be freely summed over the cell momenta. The partial collapse of the

---

[1]Skeletal graph sum over all distinct compact closed connected diagrams constructed from the Green function and the interaction U.
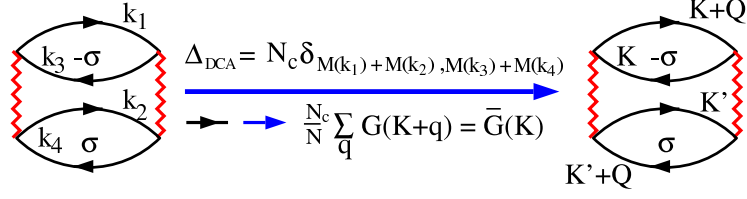
Figure 2.2 *Second-order term of the generating functional of the Hubbard model. The momentum collapse due to the interchange of the Laue function Δ with the DCA Laue function Δ_{DCA} results in the replacement of the lattice Green functions by the coarse-grained Green functions.*

momentum conservation, by applying the Δ_{DCA} to the generating functional Φ, will be demonstrated in the following calculation to which purpose we consider the Feynman rules which can be found in every standard textbook [9]:

$$
\begin{aligned}
2^{\text{nd}}\text{order} - \text{diagram} \quad \equiv \quad & \sum_{\sigma} \sum_{\substack{k_1,k_2,k_3,k_4 \\ \omega_{k_1},\omega_{k_2},\omega_{k_3},\omega_{k_4}}} \frac{1}{\beta^2} \frac{(-1)^s}{h(\Theta)} \frac{U^2}{N^4} (N\delta_{k_1+k_2,k_3+k_4})^2 \\
& \underbrace{(\delta_{\omega_1+\omega_2,\omega_3+\omega_4})^2}_{\delta_{\text{energies}}} \underbrace{\delta_{\sigma_1,\sigma_3}\delta_{\sigma_2,\sigma_4}\delta_{-\sigma_1,\sigma_2}}_{\delta_{\text{spin}}} \\
& (-G_{k_1}(\omega_{k_1}))(-G_{k_2}(\omega_{k_2}))(-G_{k_3}(\omega_{k_3}))(-G_{k_4}(\omega_{k_4})), \quad (2.6)
\end{aligned}
$$

where the sum goes over all internal momenta k_i and frequencies ω_i as well as all spin σ degrees of freedom. $h(\Theta)$ is a topology factor and s determines the number of fermionic loops. The delta functions ensure the accordant conservation laws and the delta function $\delta_{\sigma_i,-\sigma_j}$ guarantees that only electrons with opposite spins undergo the Coulomb interaction. In the next step, we approximate the Laue function in the spirit of the DCA and split off the momentum summation over k_i via Eq. (2.4), which give us:

$$
\begin{aligned}
2^{\text{nd}}\text{order} - \text{diagram} \quad \equiv \quad & \sum_{\sigma} \sum_{\substack{K_1,K_2,K_3,K_4 \\ \tilde{k}_1,\tilde{k}_2,\tilde{k}_3,\tilde{k}_4}} \sum_{\omega_{k_1},\omega_{k_2},\omega_{k_3},\omega_{k_4}} \frac{1}{\beta^2} \frac{(-1)^s}{h(\Theta)} \frac{U^2}{N^4} \delta_{\text{energies}} \, \delta_{\text{spin}} \\
& (N_c \, \delta_{M(K_1+\tilde{k}_1)+M(K_2+\tilde{k}_2),M(K_3+\tilde{k}_3)+M(K_4+\tilde{k}_4)})^2 \\
& (-G_{K_1+\tilde{k}_1}(\omega_{K_1+\tilde{k}_1})) \, (-G_{K_2+\tilde{k}_2}(\omega_{K_2+\tilde{k}_2})) \\
& (-G_{K_3+\tilde{k}_3}(\omega_{K_3+\tilde{k}_3})) \, (-G_{K_4+\tilde{k}_4}(\omega_{K_4+\tilde{k}_4})). \quad (2.7)
\end{aligned}
$$

Obviously, the summation over all intra-cluster momentum vectors $\tilde{k}_i$ can be pulled in front of the Green functions $G_{k_i}(\omega_{k_i})$:

$$
\begin{aligned}
2^{\text{nd}}\text{order} - \text{diagram} \quad \equiv \quad & \sum_{\sigma} \sum_{\substack{K_1,K_2,K_3,K_4 \\ \omega_{k_1},\omega_{k_2},\omega_{k_3},\omega_{k_4}}} \frac{1}{\beta^2} \frac{(-1)^s}{h(\Theta)} \frac{U^2}{N_c^2} \, \delta_{\text{energies}} \, \delta_{\text{spin}} \left(\delta_{K_1+K_2,K_3+K_4}\right)^2 \\
& \left(-\frac{N_c}{N} \sum_{\tilde{k}_1} G_{K_1+\tilde{k}_1}(\omega_{K_1+\tilde{k}_1})\right) \left(-\frac{N_c}{N} \sum_{\tilde{k}_2} G_{K_2+\tilde{k}_2}(\omega_{K_2+\tilde{k}_2})\right) \\
& \left(-\frac{N_c}{N} \sum_{\tilde{k}_3} G_{K_3+\tilde{k}_3}(\omega_{K_3+\tilde{k}_3})\right) \\
& \left(-\frac{N_c}{N} \sum_{\tilde{k}_4} G_{K_4+\tilde{k}_4}(\omega_{K_4+\tilde{k}_4})\right),
\end{aligned}
\tag{2.8}
$$

where we can identify the coarse-grained Green function $\bar{G}[M(\boldsymbol{k})]$ as:

$$
\bar{G}(\boldsymbol{K}) = \frac{N_c}{N} \sum_{\tilde{\boldsymbol{k}}} G(\boldsymbol{K} + \tilde{\boldsymbol{k}}),
\tag{2.9}
$$

with the number of lattice sites N, N_c is the number of clusters, and the $\tilde{\boldsymbol{k}}$ runs over the momenta of the cell with cluster momentum $\boldsymbol{K}$. We have seen, that the diagrammatic sequence of the generating functional remains unchanged under the DCA approximation, but under the assumption $N_c \ll N$, the complexity of the problem is drastically reduced.

2.3 Cluster sizes and topologies

In this section, we are going to examine different cluster sizes and topologies of our DCA approach. We have seen, that sufficiently small clusters enormously reduce the complexity of the original problem, but the remaining cluster problem represents an exhausting numerical task. In order to take a larger variety of cluster types into account, we also focus on cluster types which deviate from the usual square shaped cluster form. A general overview of different cluster sizes and topologies is given in Refs. [10, 11]. The authors of [11] investigate differ cluster types by referring to the finite size scaling behaviour of the Néel temperature of the 3-dimensional Hubbard model.

Lets assume, that the real space cluster is described by the principle lattice vectors $\boldsymbol{a}_1$ and $\boldsymbol{a}_2$. They are correlated to the reciprocal lattice vectors by the expression $\boldsymbol{b}_i = 2\pi\boldsymbol{a}_i/|\boldsymbol{a}_1 \times \boldsymbol{a}_2|$ with $\boldsymbol{k}_{nm} = n\boldsymbol{b}_1 + m\boldsymbol{b}_2$ for integer n and m. We can distinguish three different kinds of cluster families. The first is described by tilings with $a_{1x} = a_{1y}$ (corresponding to $N_c = 1, 8, 18, 32, \ldots$) where we have chosen the cluster types with $N_c = 1, 8$ for our calculations. The second family exhibits real-space principle cluster vectors with either $a_{1x} = 0$ or $a_{1y} = 0$, which leads to cluster types with $N_c = 1, 4, 16, 36, \ldots$. The single
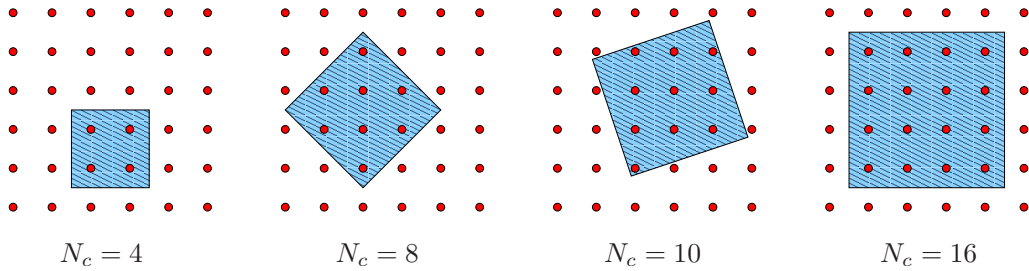
$$N_c = 4 \qquad N_c = 8 \qquad N_c = 10 \qquad N_c = 16$$

Figure 2.3 *Different cluster types and topologies which are utilised in our study.*

site cluster (see above) and the four and 16-sites cluster were used in our calculation. Both families are basically different in respect to the angle θ between the reciprocal lattice vectors compare to the principle reciprocal lattice vectors of the real system. In the first case the angle θ is $\pi/4$ whereas in the second case it is $\theta = 0$. In the third class of cluster types, we combine all other clusters with the property that they do not obey the point-group symmetry of the original lattice. Starting from the Hubbard model, we assert a C_{4v} symmetry, which is carried over to the coarse-grained cells in the first two families of cluster types. The reciprocal principle lattice vectors of the third class of cluster types with $N_c = 10, 20, 26, 34,$ ... do not point along a high symmetry direction of the real space. The consequence will be, that in principle equal points of the original lattice will map onto different cluster patches during the coarse-graining procedure. In order to obtain a comprehensive picture of the different cluster types, we take also the $N_c = 10$ into account in our calculations. A summary of the clusters utilised in our investigation is depicted in Fig. 2.3.

2.4 The DCA self-consistent loop

The DCA algorithm basically consists of two parts as shown in Fig. 2.4. The main part is captured by the self-consistent procedure, namely the coarse-graining of the lattice and the utilisation of the Dyson equation. This part will be explained in detail in the following. The second part includes the quantum Monte Carlo procedure to which purpose we employ the Hirsch-Fye algorithm, which is explained in section 2.7. The QMC procedure is the most time and resources consuming part in the self-consistent circle and is therefore carried out on a supercomputer.

The DCA self-consistent loop:

i) The DCA self-consistent loop starts with an initial guess of the self-energy $\Sigma_c(\boldsymbol{K}, i\omega_m)$. This value can be set to zero or to a perturbation theory result.

ii) The free lattice Green function $G^0(\boldsymbol{k}, i\omega_m)$ and the self-energy $\Sigma_c(\boldsymbol{K}, i\omega_m)$ are used to calculate the coarse-grained Green function $\bar{G}(\boldsymbol{K}, i\omega_m)$. N is the number of lattice

$$\boxed{\text{Cluster solver: Hirsch– Fye Algorithm}}$$

$$\mathcal{G}(\boldsymbol{X}_i - \boldsymbol{X}_j, \tau) \qquad\qquad\qquad G_c(\boldsymbol{X}_i - \boldsymbol{X}_j, \tau)$$

$$\mathcal{G}^{-1}(\boldsymbol{K}, i\omega_n) = \bar{G}^{-1}(\boldsymbol{K}, i\omega_n) + \Sigma_c(\boldsymbol{K}, i\omega_n) \qquad \Sigma_c(\boldsymbol{K}, i\omega_n) = \mathcal{G}^{-1}(\boldsymbol{K}, i\omega_n) - G_c^{-1}(\boldsymbol{K}, i\omega_n)$$

$$\bar{G}(\boldsymbol{K}, i\omega_n) = \frac{N_c}{N} \sum_{\tilde{\boldsymbol{k}}} \frac{1}{i\omega_n - \epsilon_{\boldsymbol{K}+\tilde{\boldsymbol{k}}} + \mu - \Sigma_c(\boldsymbol{K}, i\omega_n)}$$
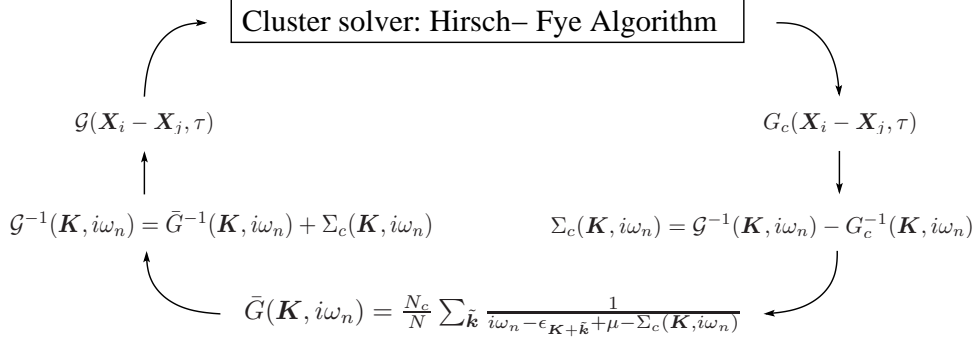
Figure 2.4 *Sketch of the DCA algorithm.*

sites and N_c declares the number of lattice sites within the real space cluster:

$$\bar{G}(\boldsymbol{K}, i\omega_m) = \frac{N_c}{N} \sum_{\tilde{\boldsymbol{k}}} \frac{1}{i\omega_m - \epsilon_{\boldsymbol{K}+\tilde{\boldsymbol{k}}} + \mu - \Sigma_c(\boldsymbol{K}, i\omega_m)} \tag{2.10}$$

At this point, the DCA assumes that $\Sigma_c(\boldsymbol{K}, i\omega_m)$ is only weakly dependent on momentum, so that we may write $\Sigma(\boldsymbol{K} + \tilde{\boldsymbol{k}}, i\omega_m) \approx \Sigma_c(\boldsymbol{K}, i\omega_m)$.

iii) The bare host Green function is given by the Dyson Equation:

$$\mathcal{G}^{-1}(\boldsymbol{K}, i\omega_m) = \bar{G}^{-1}(\boldsymbol{K}, i\omega_m) + \Sigma_c(\boldsymbol{K}, i\omega_m) \tag{2.11}$$

At this point, we have to subtract the self-energy in order to avoid over-counting diagrams and calculate the bare Green function of the cluster problem.

iv) In order to utilise the QMC procedure $\mathcal{G}(\boldsymbol{K}, i\omega_m)$ must be Fourier transformed from the momentum-frequency variables to space-imaginary-time variables:

$$\mathcal{G}(\boldsymbol{K}, i\omega_m) \longrightarrow \mathcal{G}(X_i - X_j, \tau_i - \tau_j) \tag{2.12}$$

v) The interacting cluster Green function $G_c(X_i - X_j, \tau_i - \tau_j)$ is obtained by using the QMC algorithm. This step is the most time consuming part.

vi) $G_c(X_i - X_j, \tau_i - \tau_j)$ is then Fourier transformed to momentum-frequency variables $G_c(\boldsymbol{K}, i\omega_m)$ and the Dyson Equation is used a second time in order to calculate a new cluster self-energy:

$$\Sigma_c(\boldsymbol{K}, i\omega_m) = \mathcal{G}^{-1}(\boldsymbol{K}, i\omega_m) - G_c^{-1}(\boldsymbol{K}, i\omega_m) \tag{2.13}$$

vii) These step are repeated until $\Sigma_c(\boldsymbol{K}, i\omega_m)$ converges.

viii) The lattice Green function depends on the momentum $\boldsymbol{k} = \boldsymbol{K} + \tilde{\boldsymbol{k}}$ and is calculated by:

$$G^{lat}(\boldsymbol{k}, i\omega_m) = \frac{1}{i\omega_m - \epsilon_{\boldsymbol{K}+\tilde{\boldsymbol{k}}} + \mu - \Sigma_c(\boldsymbol{K}, i\omega_m)} \tag{2.14}$$

2.5 Numerical implementation of the Fourier transformation

As described in the previous section, a Fourier transformation between Matsubara energy Green functions $G(\boldsymbol{K}, i\omega_m)$ and imaginary time Green functions $G(\boldsymbol{K}, \tau)$ has to be performed. In general, the Fourier transformation is nothing else but:

$$G(\boldsymbol{K}, i\omega_m) = \int_0^\beta d\tau \, e^{i\omega_m \tau} G(\boldsymbol{K}, \tau). \tag{2.15}$$

The numerical implementation of the Fourier transformation is a challenging task in order to capture the correct high-frequency behaviour of the Green function or self-energy. The Green function $G(\boldsymbol{K}, \tau)$ is only given on a discrete subset in the interval $[0, \beta]$. A simply interpolation strategy, i.e., an Akima spline, yields incorrect high-frequency results and the causality requirement:

$$\lim_{\omega_m \to \infty} G(\boldsymbol{K}, i\omega_m) \approx \frac{1}{i\omega_m} \tag{2.16}$$

would be violated. An enhancement of the discretisation in imaginary time would alleviate this problem but it would cause an intractable QMC simulation because of the CPU time and memory requirements which would increase to the power of three with respect to the number of imaginary time slices. Instead of this, we use the spectral representation of the Green function $G(\tau)$:

$$G(\tau) = -\int d\omega A(\omega) \frac{e^{-\tau\omega}}{1 + e^{-\beta\omega}} \text{ with } A(\omega) = -\frac{1}{\pi} \text{Im}[G(\omega + i0^+)] \tag{2.17}$$

The analytical continuation of the Green function $G(\tau)$ yields the corresponding spectral function $A(\omega)$ on a discrete set of real frequencies which obeys the following identity:

$$G(\tau) = -\sum_n \Delta\omega A(n\Delta\omega) \frac{e^{-\tau n\Delta\omega}}{1 + e^{-\beta n\Delta\omega}}. \tag{2.18}$$

Thus, the Fourier transformation of $G(\tau)$ to $G(i\omega_m)$ can be accomplished under consideration of the spectral theorem:

$$G(i\omega_m) = -\sum_n \Delta\omega \frac{A(n\Delta\omega)}{i\omega_m - n\Delta\omega} \tag{2.19}$$

It has been shown, that such a Fourier transformation provides the correct asymptotic behaviour of the Matsubara Green functions.

The inverse Fourier transformation provides $G(\tau)$ for a given Green function $G(i\omega_m)$:

$$G(\tau) = \frac{1}{\beta} \sum_{\omega_m} e^{-i\omega_m \tau} G(i\omega_m) \tag{2.20}$$

The discontinuity of $G(\tau)|_{\tau=0,\beta}$ can only be reproduced when an infinite number of Matsubara frequencies are taken into account in the sum of Eq. (2.20). In order to circumvent this problem, we consider the asymptotic behaviour of the Matsubara Green function:

$$
\begin{aligned}
G(i\omega_m) &= \int \mathrm{d}\omega \frac{A(\omega)}{i\omega_m - \omega} \\
&= \frac{1}{i\omega_m} \int \mathrm{d}\omega A(\omega) + \frac{1}{(i\omega_m)^2} \int \mathrm{d}\omega A(\omega)\omega + \mathcal{O}\left(\frac{1}{\omega_m^3}\right)
\end{aligned}
\tag{2.21}
$$

Obviously, Eq. (2.21) exhibits the correct high frequency behaviour: $\mathrm{Im}[G(i\omega_m)] = -1/i\omega_m + \mathcal{O}(1/\omega_m^3)$. The real part of the Green function $\mathrm{Re}[G(i\omega_m)]$ can be fitted by a least square fit to the form $b/(i\omega_m)^2$ with the abbreviation $b = \int \mathrm{d}\omega A(\omega)\omega$. After the rearrangement of the RHS of Eq. (2.20), one gets:

$$
\begin{aligned}
G(\tau) &= \frac{1}{\beta} \sum_{\omega_m} e^{-i\omega_m \tau} \left(G(i\omega_m) - \frac{1}{i\omega_m} + \frac{b}{\omega_m^2} \right) \\
&+ \frac{1}{\beta} \sum_{\omega_m} e^{-i\omega_m \tau} \left(\frac{1}{i\omega_m} - \frac{b}{\omega_m^2} \right).
\end{aligned}
\tag{2.22}
$$

For sufficiently large Matsubara frequencies $i\omega_m$, only the second sum of Eq. (2.22) gives a contribution to $G(\tau)$, therefore, the first summation has to be carried out only on a finite subset of Matsubara frequencies $i\omega_m$. The second sum may be computed analytically. For $0 < \tau < \beta$ we have:

$$\frac{1}{\beta} \sum_{\omega_m} \frac{e^{-\omega_m \tau}}{i\omega_m} = -\frac{1}{2} \tag{2.23}$$

$$\frac{b}{\beta} \sum_{\omega_m} \frac{e^{-\omega_m \tau}}{(i\omega_m)^2} = \frac{b}{2}\tau - \frac{b}{4}\beta. \tag{2.24}$$

2.6 Local quantities

In the following section, we express some comments about local cluster quantities. The consideration below shows that local lattice quantities can already be calculated on the DCA cluster. We focus initially on the lattice Green function, which is given by the Dyson equation:

$$G^{lat}(\boldsymbol{k}, i\omega_m) = \frac{1}{i\omega_m - (\epsilon(\boldsymbol{k}) - \mu) - \Sigma_c(\boldsymbol{K}, i\omega_m)} \tag{2.25}$$

The local lattice Green function reads:

$$G_{ii}^{lat}(i\omega_m) \quad = \quad \frac{1}{N} \sum_{\boldsymbol{k}} G^{lat}(\boldsymbol{k}, i\omega_m) \tag{2.26}$$

$$= \quad \frac{1}{N} \sum_{\boldsymbol{K}} \sum_{\boldsymbol{k} \,\in\, \mathrm{patch}\boldsymbol{K}} \frac{1}{i\omega_m - (\epsilon(\boldsymbol{k}) - \mu) - \Sigma_c(\boldsymbol{K}, i\omega_m)} \tag{2.27}$$

If we apply the definition of the coarse-grained Green function to the last expression in Eq. (2.27) and assume that self-consistence in the DCA loop has been achieved, then we can write:

$$G_{ii}^{lat}(i\omega_m) = \frac{1}{N_c} \sum_{\boldsymbol{K}} G_c(\boldsymbol{K}, i\omega_m). \tag{2.28}$$

Hence, the last equality exhibits an easy access to calculate local quantities in the DCA calculation, i.e. occupation numbers, magnetisation or local order parameters.

2.7 The QMC algorithm

As described in the previous section, the complexity of the original lattice problem can be reduced dramatically by coarse graining of the Green function. Hereby, the bath Green function $\mathcal{G}(i\omega_m)$, which is determined from the coarse-grained Green function $\bar{G}(i\omega_m)$ and the self-energy $\Sigma_c(i\omega_m)$, can be interpreted as the non-interacting Green function of the cluster problem. The cluster problem may be solved by a variety of methods. Typical candidates are the quantum Monte Carlo method (QMC) [12], the fluctuation exchange approximation (FLEX) [13], or the non-crossing approximation (NCA) [14]. The most appropriated method for our problem is the Quantum Monte Carlo technique, i.e., Hirsch-Fye algorithm (HF). It was first developed in order to solve few-impurity problems and it contributes very well to the Kondo problem as well as to the impurity problem of the DMFA. Compared to the conventional Blankenbecler-Sugar-Scalapino (BSS) [15] algorithm, the Hirsch-Fye algorithm does not show any stabilisation problems and it is characterised by a mild minus-sign problem away from half-filling. On the other hand, the HF algorithm is much more involved with respect to the CPU time and memory requirements. A comparison of the scaling behaviour of the CPU time and memory requirements as a function of system size and Trotter slices (which are directly related to the inverse temperature) respectively, are shown for both methods in Tab. 2.1. It explicitly shows, that calculations with the Hirsch-Fye algorithm are restricted to smaller clusters when compared to BSS calculations due to a poorer CPU time and memory scaling behaviour. Nevertheless, calculations within the DCA are carried out in thermodynamic limit because spatial correlations which exceed the cluster size are treated on a mean-field level, whereas the BSS calculations are performed on a finite lattice, where finite size problems are still present. Furthermore, one should keep in mind that the HF algorithm is in general an action based method, which

	CPU time	MEMORY
HF	$(N_l N_c)^3$	$(N_l N_c)^2$
BSS	$N_l N_c^3$	$N_l N_c^2$

Table 2.1 *Scaling behaviour of the CPU time and memory as a function of the number of clusters N_c and Trotter slices N_l of the Hirsch-Fye algorithm (HF) and Blankenbecler-Sugar-Scalapino quantum Monte Carlo (BSS) algorithm.*

means, that detailed knowledge of the Hamiltonian is not needed. In contrast, the BSS algorithm is a Hamiltonian based technique which gives the important constitutional difference between both methods and it becomes crucial when we consider that the detailed or effective form of the Hamiltonian of the cluster problem within the DCA self-consistent loop is unknown. Furthermore, the Monte Carlo upgrade procedure of the BSS algorithm additionally requires certain stabilisation techniques which increase the computational effort of the simulation [16]. Finally, as we will see in the next paragraph, the measurement off time-displaced quantities can be performed in the HF algorithm without essentially increasing of the computational effort.

In the first part of the next paragraph, basic concepts of auxiliary field Quantum Monte Carlo techniques are presented. With the introduction of auxiliary fields, i.e., Hubbard-Stratonovich fields, it is possible to manage a decomposition of the interacting term of the underlying Hamiltonian. In a further step, the partition function can be expressed by imaginary time propagators $U_{\boldsymbol{s}}(\beta, 0)$ and $B_{\boldsymbol{s}}(\beta, 0)$, where the index $\boldsymbol{s}$ corresponds to a given configuration of the introduced auxiliary field. Nevertheless, in order to calculate the partition function, one has to capture all field configurations which in principle represents an unsolvable task. To circumvent this problem, we adobe the Hirsch-Fye quantum Monte Carlo algorithm, which allows us to reduce the whole phasespace of configurations of the auxiliary field to a subset of configurations. The smaller configuration sample is chosen in such a way that the occurrence of the field configurations are distributed according to their occurrence probability. The Hirsch-Fye algorithm is presented in section 2.7.3.

2.7.1 Auxiliary Field Quantum Monte Carlo

In the forthcoming paragraph, we introduce the periodic Anderson impurity model (PAM) [17] which solves the cluster problem already described above within the DCA self-consistent loop.

The PAM is defined as:

$$H = H_0 + H_U \tag{2.29}$$

with

$$
\begin{aligned}
H_0 &= \sum_{k,\sigma} \epsilon(k) d_{k\sigma}^\dagger d_{k\sigma} + \sum_{i\sigma} (\epsilon_d d_{i\sigma}^\dagger d_{i\sigma} + \epsilon_f f_{i\sigma}^\dagger f_{i\sigma}) \\
&\quad + \sum_{k\sigma} V(k)(d_{k\sigma}^\dagger f_{k\sigma} + h.c.) \tag{2.30} \\
H_U &= U \sum_i (n_{fi\uparrow} - \frac{1}{2})(n_{fi\downarrow} - \frac{1}{2}), \tag{2.31}
\end{aligned}
$$

where $d_{i\sigma}(f_{i\sigma})^{(\dagger)}$ destroys (creates) a d(f) electron on site i with spin σ, ϵ_d and ϵ_f are the orbital energies of the d and f electrons respectively, $V(k)$ is the $d - f$ hybridisation, and U the on-site Coulomb repulsion of the f-electrons. The operator $d_{k\sigma}(f_{k\sigma})^{(\dagger)}$ destroys (creates) a d(f) electron with momentum k and spin σ. The dispersion of the d electrons is given by $\epsilon(k)$. The reader is referred to [17, 18] for a detailed overview of the Anderson model.

The goal of our investigation is the determination of the partition function $\mathcal{Z} = Tr[e^{-\beta(H-\mu N)}]$. The cluster problem of the DCA is described by the PAM with the host Green function $\mathcal{G}$ which corresponds to the non-interaction Green function of the cluster problem. If we introduce Grassmann variables γ's, we can rewrite the partition function as a path integral:

$$
\mathcal{Z} = \int \mathcal{D}\gamma^\star \mathcal{D}\gamma e^{-\int_0^\beta \mathrm{d}\tau \mathrm{d}\tau' \sum_{i,j,\sigma} \gamma_{i,j}^\star(\tau) \mathcal{G}^{-1}(i,\tau;j,\tau')\gamma_{j,\sigma}(\tau') - \int_0^\beta \mathrm{d}\tau H_U(\gamma_{i,\sigma}^\star(\tau),\gamma_{i,\sigma}(\tau))} \tag{2.32}
$$

The input (free) cluster Green function $\mathcal{G}(i,\tau;j,\tau')$ depends on the time and spatial coordinates. The decomposition of the purely local Hubbard-like interaction term H_U is performed in two steps. First, the exponent of the partition function is split off by introducing a discrete set of time slices with lengths $\Delta\tau = \frac{\beta}{N_l}$ and a positive integer N_l:

$$
\mathcal{Z} = Tr[e^{-\beta(H-\mu N)}] = Tr[(e^{-\Delta\tau(H_0+H_U)})^{N_l}]. \tag{2.33}
$$

In the second step, the exponential function can be decomposed, by considering that for a finite value of $\Delta\tau$ a systematic error $(\Delta\tau)^2$ occurs since $[H_0, H_U] \neq 0$:

$$
\mathcal{Z} = Tr[(e^{-\Delta\tau(H_0+H_U)})^{N_l}] = Tr[(e^{-\Delta\tau H_0} e^{-\Delta\tau H_U})^{N_l}] + \mathcal{O}(\Delta\tau^2). \tag{2.34}
$$

The error in $\Delta\tau$ can only be reduced by an enhancement of the number of time slices which automatically increases the computational effort of the calculation. By introducing a bosonic auxiliary field ϕ [19] the two-particle interaction in H_U can be expressed as a sum over all field configurations ϕ and one-particle operators which interact with the auxiliary field ϕ. In general, we can derive the following identity from the Gaussian integral:

$$
e^{A^2/2} = \frac{1}{\sqrt{2\pi}} \int_{-\infty}^{+\infty} \mathrm{d}\phi e^{-\frac{\phi^2}{2} - \phi A}. \tag{2.35}
$$

The important advantage of Eq. (2.35) lies in the fact, that for a given Hubbard-Stratonovich field ϕ the one body-problem is exact solvable. For a numerical approach, it is more convenient to discretise the auxiliary field where each configuration is described by a vector $\boldsymbol{s}$. Hence, we can rewrite the exponential function of the partition function:

$$e^{\Delta\tau U \sum_i (f_{i\uparrow}^\dagger f_{i\uparrow} - \frac{1}{2})(f_{i\downarrow}^\dagger f_{i\downarrow} - \frac{1}{2})} = C \sum_{\boldsymbol{s}=\pm 1} e^{\alpha \sum_i s_i (f_{i\uparrow}^\dagger f_{i\uparrow} - f_{i\downarrow}^\dagger f_{i\downarrow})}, \tag{2.36}$$

with

$$C = \frac{1}{2^{N_c}} e^{-\Delta\tau U N_c/4} \tag{2.37}$$

$$\cosh(\alpha) = e^{\Delta\tau U/2}. \tag{2.38}$$

With the decomposition of the exponential function in Eq. (2.34) and the introduction of the Hubbard-Stratonovich field, the partition function in Eq. (2.32) may be written as:

$$\mathcal{Z} \propto Tr_{s_{i,l}} \int \prod_{l,l'}^{N_l} \prod_{i,j}^{N_c} \mathrm{d}\gamma_{il,\sigma}^\star \mathrm{d}\gamma_{il,\sigma} e^{-\sum_{il,jl',\sigma} \gamma_{il,\sigma}^\star \mathcal{G}_{il;jl'}^{-1} \gamma_{jl',\sigma}} e^{-\sum_{i,l,\sigma} \alpha s_{i,l} \gamma_{il,\sigma}^\star \gamma_{i(l-1),\sigma}} \tag{2.39}$$

The integration over the electronic degrees of freedom (Grassmann variables) yields:

$$\mathcal{Z} \propto Tr_{s_{i,l}} \prod_\sigma \det(G_{s,\sigma})^{-1}, \tag{2.40}$$

where

$$(G_{s,\sigma})_{il,jl'}^{-1} = \mathcal{G}_{il;il'}^{-1} + \alpha\sigma s_{i,l}\delta_{i,j}\delta_{l',l-1}. \tag{2.41}$$

2.7.2 Numerical implementation

The numerical implementation of the Hirsch-Fye algorithm requires a reformulation of the partition function and the Green functions respectively. For this purpose, we introduce imaginary time propagators $U_{\boldsymbol{s}}$ and $B_{\boldsymbol{s}}$ in order to reformulate the partition function in Eq. (2.40):

$$\mathcal{Z} = C^{N_l} \sum_{\boldsymbol{s}} \prod_\sigma \det[1 + B_{N_l}^\sigma B_{N_l-1}^\sigma \ldots B_1^\sigma], \tag{2.42}$$

with

$$B_n^\sigma = e^{V^{(\sigma)}(s_n)} e^{-\Delta\tau h_0}. \tag{2.43}$$

A detailed derivation is given in the works of F. F. Assaad [20] and L. C. Martin [21]. The matrices $V^{(\sigma)}(s_n)$ have the components $\sigma\alpha s_n \delta_{i,j}\delta_{i,f-\text{sites}}$ with the auxiliary field s_n at imaginary time step n. We also introduce the second-quantisation time evolution operator $U_{\boldsymbol{s}}^\sigma(\tau_2, \tau_1)$:

$$U_{\boldsymbol{s}}(\tau_2, \tau_1) = \prod_\sigma \prod_{n=n_1+1}^{n_2} e^{\boldsymbol{a}_\sigma^\dagger V(s_n)\boldsymbol{a}_\sigma} e^{-\Delta\tau \boldsymbol{a}_\sigma^\dagger h_0 \boldsymbol{a}_\sigma} \tag{2.44}$$

The operator $\boldsymbol{a}^{(\dagger)}$ destroys (creates) an electron on a conduction or impurity site. We should keep in mind that the electron interaction takes only place on the f-sites. What follows is an overview of the measurement of observables and time-displaced single- and two-particle Green functions within the Hirsch-Fye algorithm.

Observables

The thermodynamic definition of the expectation value of the variable O is given by:

$$\langle O \rangle = \frac{Tr[e^{-\beta H}O]}{Tr[e^{-\beta H}]} \tag{2.45}$$

The evolution of the exponential function in imaginary time can be reformulated by the imaginary time propagators $U_{\boldsymbol{s}}(\tau_2, \tau_1)$ (Eq.(2.44)):

$$
\begin{aligned}
\langle O \rangle &= \frac{\sum_{\boldsymbol{s}} Tr[U_{\boldsymbol{s}}(\beta,\tau)OU_{\boldsymbol{s}}(\tau,0)]}{\sum_{\boldsymbol{s}} \prod_{\sigma} \det(1 + B_{\boldsymbol{s}}^{\sigma}(\beta,0))} \\
&= \left(\sum_{\boldsymbol{s}} \frac{\prod_{\sigma} \det(1 + B_{\boldsymbol{s}}^{\sigma}(\beta,0))}{\sum_{\boldsymbol{s}} \prod_{\sigma} \det(1 + B_{\boldsymbol{s}}^{\sigma}(\beta,0))} \right) \cdot \left(\frac{Tr[U_{\boldsymbol{s}}(\beta,\tau)OU_{\boldsymbol{s}}(\tau,0)]}{\prod_{\sigma} \det(1 + B_{\boldsymbol{s}}^{\sigma}(\beta,0))} \right) \\
&= \left(\sum_{\boldsymbol{s}} \frac{\prod_{\sigma} \det(1 + B_{\boldsymbol{s}}^{\sigma}(\beta,0))}{\sum_{\boldsymbol{s}} \prod_{\sigma} \det(1 + B_{\boldsymbol{s}}^{\sigma}(\beta,0))} \right) \cdot \left(\frac{Tr[U_{\boldsymbol{s}}(\beta,\tau)OU_{\boldsymbol{s}}(\tau,0)]}{Tr[U_{\boldsymbol{s}}(\beta,0)]} \right) \\
&= \sum_{\boldsymbol{s}} P_{\boldsymbol{s}} \langle O \rangle_{\boldsymbol{s}}
\end{aligned} \tag{2.46}
$$

The above equality is a result of the properties of the Slater determinants and will not be discussed here. Eq. (2.46) shows, that the expectation value of an observable O can be expressed as a weighted average of the measurement of O for a given Hubbard-Stratonovich field $\boldsymbol{s}$. The quantity $P_{\boldsymbol{s}}$ corresponds to the density matrix which, as opposed to in classical simulation, can be negative and leads to the notorious minus-sign problem. In order to see this problem, we keep track of the sign $\eta_{\boldsymbol{s}}$ of the quantity $p_{\boldsymbol{s}} = \prod_{\sigma} \det(1 + B_{\boldsymbol{s}}^{\sigma}(\beta,0))$. We formulate $p'_{\boldsymbol{s}} = |p_{\boldsymbol{s}}|$ and

$$
\begin{aligned}
\langle O \rangle_p &= \frac{\sum_{\boldsymbol{s}} p_{\boldsymbol{s}} \langle O \rangle_{\boldsymbol{s}}}{\sum_{\boldsymbol{s}} p_{\boldsymbol{s}}} = \frac{\sum_{\boldsymbol{s}} |p_{\boldsymbol{s}}| \eta_{\boldsymbol{s}} \langle O \rangle_{\boldsymbol{s}}}{\sum_{\boldsymbol{s}} |p_{\boldsymbol{s}}| \eta_{\boldsymbol{s}}} \\
&= \frac{\sum_{\boldsymbol{s}} p'_{\boldsymbol{s}} [\eta_{\boldsymbol{s}} O_{\boldsymbol{s}}]}{\sum_{\boldsymbol{s}} p'_{\boldsymbol{s}} \eta_{\boldsymbol{s}}} \cdot \frac{\sum_{\boldsymbol{s}} p'_{\boldsymbol{s}}}{\sum_{\boldsymbol{s}} p'_{\boldsymbol{s}}} \\
&= \frac{\langle \eta O \rangle_{p'}}{\langle \eta \rangle_{p'}}.
\end{aligned} \tag{2.47}
$$

The Boltzmann weight was written as $p_{\boldsymbol{s}} = p'_{\boldsymbol{s}} \eta_{\boldsymbol{s}}$ with $\eta_{\boldsymbol{s}} = \pm 1$. The last equality shows, that in the case of a very small average sign, the expectation value of the observable O underlies strong fluctuations. In order to compensate for the reduction of the quality of the data, one has to improve the statistics of the calculation by a factor of $\langle sign \rangle^{-2}$ compared to the situation where the minus-sign problem is absent.

The minus-sign problem occurs in the repulsive Hubbard model away from half-filling. In the case of particle-hole symmetry and for the attractive Hubbard model, it can be shown, that the density matrices for the two spin channels occur with the same sign for any field configurations $\boldsymbol{s}$:

$$\text{sign}\{\det[1 + B_{\boldsymbol{s}}^{\uparrow}]\} = \text{sign}\{\det[1 + B_{\boldsymbol{s}}^{\downarrow}]\}, \tag{2.48}$$

and hence, no minus-sign problem occurs.

Equal-time observable

We can estimate the expectation value of a single-body observable $O = \boldsymbol{c}^{\dagger} A \boldsymbol{c}$:

$$
\begin{aligned}
\langle O \rangle_{\boldsymbol{s}} &= \frac{\partial}{\partial \alpha} \ln Tr[U_{\boldsymbol{s}}(\beta, \tau) e^{\alpha O} U_{\boldsymbol{s}}(\tau, 0)]|_{\alpha=0} \\
&= \frac{\partial}{\partial \alpha} \ln \det[1 + B_{\boldsymbol{s}}(\beta, \tau) e^{\alpha A} B_{\boldsymbol{s}}(\tau, 0)]|_{\alpha=0} \\
&= \frac{\partial}{\partial \alpha} Tr \ln[1 + B_{\boldsymbol{s}}(\beta, \tau) e^{\alpha A} B_{\boldsymbol{s}}(\tau, 0)]|_{\alpha=0} \\
&= Tr\left[B_{\boldsymbol{s}}(\tau, 0)(1 + B_{\boldsymbol{s}}(\beta, 0))^{-1} B_{\boldsymbol{s}}(\beta, \tau) A \right] \\
&= Tr\left[(1 - (1 + B_{\boldsymbol{s}}(\tau, 0) B_{\boldsymbol{s}}(\beta, \tau))^{-1}) A \right]
\end{aligned}
\tag{2.49}
$$

The equal-time Green function may be written with the choice of A: $A_{x_1, x_2} = \delta_{x_1, y} \delta_{x_2, x}$ as:

$$G_{\boldsymbol{s}}(\tau, \tau)_{x,y} = \delta_{x,y} - \langle c^{\dagger} A c \rangle_{\boldsymbol{s}}, \tag{2.50}$$

and with Eq. (2.49) we derive the important result:

$$G_{\boldsymbol{s}}(\tau, \tau)_{x,y} = [1 + B_{\boldsymbol{s}}(\tau, 0) B_{\boldsymbol{s}}(\beta, \tau)]_{x,y}^{-1}, \tag{2.51}$$

which states, that any equal-time Green function can expressed in terms of matrices $B_{\boldsymbol{s}}$. Furthermore, it can be shown, that any equal-time multi-point correlation function can be formulated in sums of products of single-particle Green functions which corresponds to the validity of Wick's theorem. More technical considerations can be found in [20] and will not be repeated in this work again.

Imaginary time displaced Green Functions

Imaginary time displaced Green functions, such as single- and two-particle Green functions determine a variety of crucial properties of many particle systems. They contain information about spin as well as charge gaps [22, 23]. Furthermore, an inverse Laplace transformation, which can be performed via the Maximum Entropy technique [24, 25] (Sec. 3.2), provides the real-energy spectrum of the corresponding correlation function

and makes a direct comparison between theory and experimental measurements, such as photoemission, neutron scattering and optical measurements, possible.

In the following paragraph, we are going to show, that the time dependence of Green functions can be absorbed in the operators $B_{\boldsymbol{s}}^{\sigma}$. Furthermore, we present exemplarily for the two-particle Green function, that in general, any n-point time-displaced correlation function can be mapped onto n-point equal-time correlation functions, which consist of a sum of products of equal-time Green functions.

The single-particle Green function is defined by:

$$G(\tau_1, \tau_2)_{x,y} = -\langle \mathcal{T} a_x(\tau_1) a_y^\dagger(\tau_2) \rangle = \begin{cases} -\langle a_x(\tau_1) a_y^\dagger(\tau_2) \rangle, & \text{if } \tau_1 \geq \tau_2 \\ \langle a_y^\dagger(\tau_2) a_x(\tau_1) \rangle, & \text{if } \tau_1 < \tau_2 \end{cases} \tag{2.52}$$

We neglect in the forthcoming paragraph the minus-sign in the definition of the Green function due to convenience. By considering Eq. (2.46), the time-displaced Green function can be formulated as a weighted average over the field configurations $\boldsymbol{s}$:

$$G(\tau_1, \tau_2)_{x,y} = \sum_{\boldsymbol{s}} P_{\boldsymbol{s}} G_{\boldsymbol{s}}(\tau_1, \tau_2)_{x,y}. \tag{2.53}$$

Assume that $\beta > \tau_1 > \tau_2$ holds, then we can rewrite $G_{\boldsymbol{s}}(\tau_1, \tau_2)$:

$$\langle a_x(\tau_1) a_y^\dagger(\tau_2) \rangle_{\boldsymbol{s}} = \frac{Tr\left[U_{\boldsymbol{s}}(\beta, 0) e^{H\tau_1} a_x e^{-H\tau_1} e^{H\tau_2} a_y^\dagger e^{-H\tau_2} \right]}{Tr\left[U_{\boldsymbol{s}}(\beta, 0) \right]} \tag{2.54}$$

$$= \frac{Tr\left[U_{\boldsymbol{s}}(\beta, \tau_2) U_{\boldsymbol{s}}^{-1}(\tau_1, \tau_2) a_x U_{\boldsymbol{s}}(\tau_1, \tau_2) a_y^\dagger U_{\boldsymbol{s}}(\tau_2, 0) \right]}{Tr\left[U_{\boldsymbol{s}}(\beta, 0) \right]} \tag{2.55}$$

By using the definition of $U_{\boldsymbol{s}}(\tau_i, \tau_j)$ in Eq.(2.44), the term $U_{\boldsymbol{s}}^{-1}(\tau_1, \tau_2) a_x U_{\boldsymbol{s}}(\tau_1, \tau_2)$ can be expressed as a sequence of imaginary time dependent operators $e^{\pm \Delta \tau \boldsymbol{a}^\dagger A_i \boldsymbol{a}}$:

$$a_x(\tau) = e^{\Delta \tau \boldsymbol{a}^\dagger A_n \boldsymbol{a}} \dots e^{\Delta \tau \boldsymbol{a}^\dagger A_2 \boldsymbol{a}} e^{\Delta \tau \boldsymbol{a}^\dagger A_1 \boldsymbol{a}} a_x e^{-\Delta \tau \boldsymbol{a}^\dagger A_1 \boldsymbol{a}} e^{-\Delta \tau \boldsymbol{a}^\dagger A_2 \boldsymbol{a}} \dots e^{-\Delta \tau \boldsymbol{a}^\dagger A_n \boldsymbol{a}}, \tag{2.56}$$

with $\tau_1 = \tau_2 + n \cdot \Delta \tau$. The original Hamiltonian is encoded in the quantities A_i via Eq.(2.44). The propagation in imaginary time of $a_x(\tau)$ is described by $e^{\Delta \tau \boldsymbol{a}^\dagger A_1 \boldsymbol{a}} a_x e^{-\Delta \tau \boldsymbol{a}^\dagger A_1 \boldsymbol{a}}$ and from this we obtain the differential equation:

$$\frac{\partial a_x(\tau)}{\partial \tau} = -(A \boldsymbol{a}(\tau))_x, \tag{2.57}$$

with the solution

$$\boldsymbol{a}(\tau) = (e^{-A\tau} \boldsymbol{a}), \text{ and similarly } \boldsymbol{a}^\dagger(\tau) = (\boldsymbol{a}^\dagger e^{A\tau}). \tag{2.58}$$

If we successively apply the above equation then we obtain:

$$U_{\boldsymbol{s}}^{-1}(\tau_1, \tau_2) a_x U_{\boldsymbol{s}}(\tau_1, \tau_2) = (B_{\boldsymbol{s}}(\tau_1, \tau_2) \boldsymbol{a})_x \tag{2.59}$$

$$U_{\boldsymbol{s}}^{-1}(\tau_1, \tau_2) a_x^\dagger U_{\boldsymbol{s}}(\tau_1, \tau_2) = (\boldsymbol{a}^\dagger B_{\boldsymbol{s}}^{-1}(\tau_1, \tau_2))_x \tag{2.60}$$

With the last result, Eq. (2.55) may be rearranged as:

$$\langle a_x(\tau_1)a_y^\dagger(\tau_2)\rangle_{\boldsymbol{s}} = \frac{Tr\left[U_{\boldsymbol{s}}(\beta,\tau_2)[B_{\boldsymbol{s}}(\tau_1,\tau_2)\boldsymbol{a}]_x a_y^\dagger U_{\boldsymbol{s}}(\tau_2,0)\right]}{Tr\left[U_{\boldsymbol{s}}(\beta,0)\right]} \tag{2.61}$$

$$= \sum_z [B_{\boldsymbol{s}}(\tau_1,\tau_2)]_{x,z}\frac{Tr[U_{\boldsymbol{s}}(\beta,\tau_2)a_z a_y^\dagger [U_{\boldsymbol{s}}(\tau_2,\beta)]}{Tr[U_{\boldsymbol{s}}(\beta,0)]} \tag{2.62}$$

$$= \sum_z [B_{\boldsymbol{s}}(\tau_1,\tau_2)]_{x,z} G_{\boldsymbol{s}}(\tau_2,\tau_2)_{z,y} \tag{2.63}$$

$$= [B_{\boldsymbol{s}}(\tau_1,\tau_2)G_{\boldsymbol{s}}(\tau_2,\tau_2)]_{x,y}, \tag{2.64}$$

where the matrix $B_{\boldsymbol{s}}$ can be pulled in front of the trace. A straightforward calculation yields the following result for the case $\tau_2 > \tau_1$:

$$G_{\boldsymbol{s}}(\tau_1,\tau_2)_{x,y} = -[(1-G_{\boldsymbol{s}}(\tau_1,\tau_1))B_{\boldsymbol{s}}^{-1}(\tau_2,\tau_1)]_{x,y}. \tag{2.65}$$

The imaginary time dependencies of the Green function $G_{\boldsymbol{s}}$ are absorbed in the propagators $B_{\boldsymbol{s}}(\tau_i,\tau_j)$. Equivalent to the previous considerations, a time displaced two-particle correlation function can be decomposed into a sum of products of equal-time Green functions and operators $B_{\boldsymbol{s}}$:

$$\langle a_x^\dagger(\tau_1)a_x(\tau_1)a_y^\dagger(\tau_2)a_y(\tau_2)\rangle_{\boldsymbol{s}} = \tag{2.66}$$

$$= \sum_{z,z_1}[B_{\boldsymbol{s}}^{-1}(\tau_1,\tau_2)]_{z,x}[B_{\boldsymbol{s}}(\tau_1,\tau_2)]_{x,z_1}\langle a_z^\dagger(\tau_2)a_{z_1}(\tau_2)a_y^\dagger(\tau_2)c_y(\tau_2)\rangle_{\boldsymbol{s}} \tag{2.67}$$

$$= \sum_{z,z_1}[B_{\boldsymbol{s}}^{-1}(\tau_1,\tau_2)]_{z,x}[B_{\boldsymbol{s}}(\tau_1,\tau_2)]_{x,z_1}\Big[(1-G_{\boldsymbol{s}}(\tau_2,\tau_2))_{z_1,z}(1-G_{\boldsymbol{s}}(\tau_2,\tau_2))_{y,y}$$

$$+(1-G_{\boldsymbol{s}}(\tau_2,\tau_2))_{y,z}G_{\boldsymbol{s}}(\tau_2,\tau_2))_{z_1,y}\Big] \tag{2.68}$$

$$= [B_{\boldsymbol{s}}(\tau_1,\tau_2)(1-G_{\boldsymbol{s}}(\tau_2,\tau_2))B_{\boldsymbol{s}}^{-1}(\tau_1,\tau_2)]_{x,x}[1-G_{\boldsymbol{s}}(\tau_2,\tau_2)]_{y,y}$$

$$+[(1-G_{\boldsymbol{s}}(\tau_2,\tau_2))B_{\boldsymbol{s}}^{-1}(\tau_1,\tau_2)]_{y,x}[B_{\boldsymbol{s}}(\tau_1,\tau_2)G_{\boldsymbol{s}}(\tau_1,\tau_2)]_{x,y} \tag{2.69}$$

$$= [1-G_{\boldsymbol{s}}(\tau_1,\tau_1)]_{x,x}[1-G_{\boldsymbol{s}}(\tau_2,\tau_2)]_{y,y} - [G_{\boldsymbol{s}}(\tau_2,\tau_1)]_{y,x}[G_{\boldsymbol{s}}(\tau_1,\tau_2)]_{x,y}. \tag{2.70}$$

In the above derivative, we used the inverse property of the $B_{\boldsymbol{s}}(\tau_1,\tau_2)$ matrices:

$$B_{\boldsymbol{s}}(\tau_1,\tau_2)G_{\boldsymbol{s}}(\tau_2,\tau_2)B_{\boldsymbol{s}}^{-1}(\tau_1,\tau_2) = G_{\boldsymbol{s}}(\tau_1,\tau_1) \tag{2.71}$$

2.7.3 The Hirsch-Fye algorithm

The numerical implementation of the time-displaced Green function will be discussed in the following paragraph. For theses purposes, the partition function in Eq. (2.42) $\mathcal{Z}$ is rewritten in terms of matrices O^σ with the property $\det[O^\sigma] = \det[1 + B_{N_l}^\sigma B_{N_l-1}^\sigma \ldots B_1^\sigma]$

and the explicit form:

$$
O^\sigma = \begin{pmatrix}
1 & 0 & \cdot & \cdot & \cdot & B_1^\sigma \\
-B_2^\sigma & 1 & \cdot & \cdot & \cdot & 0 \\
0 & -B_3^\sigma & 1 & \cdot & \cdot & \cdot \\
\cdot & \cdot & \cdot & \cdot & \cdot & \cdot \\
\cdot & \cdot & \cdot & \cdot & \cdot & 0 \\
0 & \cdot & \cdot & 0 & -B_{N_l}^\sigma & 1
\end{pmatrix}
\tag{2.72}
$$

The time-displaced Green function $G_{\bm{s}}^\sigma(\tau_i, \tau_j)$, which is a function of discrete imaginary time slices $\tau_i = i\Delta\tau$ with $i = 1, \ldots, N_l$, can be formulated compactly in matrix form:

$$
g^\sigma = \begin{pmatrix}
G_{\bm{s}}^\sigma(\tau_1, \tau_1) & G_{\bm{s}}^\sigma(\tau_1, \tau_2) & \cdot & \cdot & G_{\bm{s}}^\sigma(\tau_1, \tau_{N_l}) \\
G_{\bm{s}}^\sigma(\tau_2, \tau_1) & G_{\bm{s}}^\sigma(\tau_2, \tau_2) & \cdot & \cdot & G_{\bm{s}}^\sigma(\tau_2, \tau_{N_l}) \\
\cdot & \cdot & \cdot & \cdot & \cdot \\
G_{\bm{s}}^\sigma(\tau_{N_l}, \tau_1) & G_{\bm{s}}^\sigma(\tau_{N_l}, \tau_2) & \cdot & \cdot & G_{\bm{s}}^\sigma(\tau_{N_l}, \tau_{N_l})
\end{pmatrix},
\tag{2.73}
$$

with the relation

$$
g^\sigma = O^{\sigma-1}.
\tag{2.74}
$$

In Eq. (2.73), we adopt the notation that each Green function $G^\sigma(\tau_i, \tau_j)$ represents a matrix, where the indices x and y indicate the spatial dependence of the Green functions:

$$
G^\sigma(\tau_i, \tau_j) = \begin{pmatrix}
[G^\sigma(\tau_i, \tau_j)]_{1,1} & [G^\sigma(\tau_i, \tau_j)]_{1,2} & \cdot & \cdot & [G^\sigma(\tau_i, \tau_j)]_{1,N_{tot}} \\
[G^\sigma(\tau_i, \tau_j)]_{2,1} & [G^\sigma(\tau_i, \tau_j)]_{2,2} & \cdot & \cdot & [G^\sigma(\tau_i, \tau_j)]_{2,N_{tot}} \\
\cdot & \cdot & \cdot & \cdot & \cdot \\
[G^\sigma(\tau_i, \tau_j)]_{N_{tot},1} & [G^\sigma(\tau_i, \tau_j)]_{N_{tot},2} & \cdot & \cdot & [G^\sigma(\tau_i, \tau_j)]_{N_{tot},N_{tot}}
\end{pmatrix}, \tag{2.75}
$$

where $[G^\sigma(\tau_i, \tau_j)]_{x,y}$ is the time displaced Green function and N_{tot} characterises the total number of sites.

The Green function matrix g is determined by a given Hubbard-Stratonovich field configuration $\bm{s}$. By changing the field configuration $\bm{s}$ to a new configuration $\bm{s}'$, the Green functions matrix changes as follows:

$$
g^\sigma = g'^\sigma + g'^\sigma \Delta^\sigma (1 - g^\sigma) \text{ with } \Delta^\sigma = (e^{V'^\sigma} e^{-V^\sigma} - 1),
\tag{2.76}
$$

where g' is the new Green function matrix corresponding to the new auxiliary field. The matrices V^σ are defined in the spirit of Eq. (2.44) as:

$$V^\sigma = \begin{pmatrix} V_1^\sigma & 0 & \cdot & \cdot & \cdot & 0 \\ 0 & V_2^\sigma & 0 & \cdot & \cdot & 0 \\ 0 & 0 & V_3^\sigma & 0 & \cdot & 0 \\ \cdot & \cdot & \cdot & \cdot & \cdot & \cdot \\ 0 & \cdot & \cdot & \cdot & 0 & V_{N_l}^\sigma \end{pmatrix}. \tag{2.77}$$

The validity of Eq. (2.76), which relates Green functions for different auxiliary fields to each other, can be shown by considering the matrix equation:

$$\tilde{O} = e^{-V^\sigma} O^\sigma \text{ with } \tilde{g} = \tilde{O}^{-1}, \tag{2.78}$$

so that (omitting the spin index σ):

$$\tilde{g} = [\tilde{O}' + \tilde{O} - \tilde{O}']^{-1} \tag{2.79}$$

$$= [\tilde{O}' + e^{-V} - e^{-V'}]^{-1} \tag{2.80}$$

$$= (\tilde{O}')^{-1} - (\tilde{O}')^{-1}(e^{-V} - e^{-V'})\tilde{g}, \tag{2.81}$$

where the last equality follows from the relation $\frac{1}{A+B} = \frac{1}{A} - \frac{1}{A}B\frac{1}{A+B}$. In the end, the Dyson equation (2.76) arises from Eq. (2.81) by inserting $\tilde{g} = ge^V$.

Finally, it should be summarised, that Eq. (2.76) describes the basis of the Hirsch-Fye algorithm and determines the upgrade scheme of the Green function during the Monte Carlo procedure.

Monte Carlo scheme

What follows is a short overview of the Monte Carlo procedure in the Hirsch-Fye algorithm and the upgrade scheme of the Green function g^σ which was introduced in Eq. (2.76). We have seen, that the quantum physical problem is reduced to a classical problem by introducing a Hubbard-Stratonovich field. The field configuration is described by $s_{i,l}$, where 'i' describes a spatial and 'l' a time coordinate. For further considerations, the indices 'i' and 'l' are combined to a superindex 'n'. A change in the Hubbard-Stratonovich field $\boldsymbol{s}_n \to \boldsymbol{s}_n'$ is accepted with the probability $R_{\boldsymbol{s} \to \boldsymbol{s}'}$. In Section 2.7.1, we have seen that the probability of the occurrence of a given field configuration $\boldsymbol{s}$ is given by $P_{\boldsymbol{s}}$. From this it follows, that the transition probability from one field configuration $\boldsymbol{s}$ to a new field

configuration s' can be written as:

$$
\begin{aligned}
R_{s \to s'} &= \prod_\sigma \frac{\det[1 + B'^\sigma_{N_l} B'^\sigma_{N_l-1} \ldots B'^\sigma_1]}{\det[1 + B^\sigma_{N_l} B^\sigma_{N_l-1} \ldots B^\sigma_1]} \\
&= \prod_\sigma \det[g^\sigma (g'^\sigma)^{-1}] \\
&= \prod_\sigma \det[1 + \Delta^\sigma(1 - g^\sigma)].
\end{aligned}
\tag{2.82}
$$

This transition probability obeys the requirement of detailed balance and ergodicity. In the beginning of the calculation the Hubbard Stratonovich field corresponds to the non-interacting Green function, e.g. all s_n are zero. In order to update the Green function one walk through the space-time and try to flip each spin. If $R_{s' \to s}$ is greater than a random number between zero and one, then the field configuration changes as follows:

$$
s'_n = \begin{cases} -s_n & \text{if } n = \tilde{f} \\ s_n & \text{if } n \neq \tilde{f} \end{cases}
\tag{2.83}
$$

Here, n' denotes the space-time coordinate where the change of the field configuration takes place. After the single-spin flip, the quantity Δ^σ exhibits only one non-zero element which is given by:

$$
\Delta^\sigma_{\tilde{f},\tilde{f}} = e^{-2\sigma\alpha s_{\tilde{f}}} - 1.
\tag{2.84}
$$

This expression can be introduced in the Dyson Eq. (2.76) which now reads:

$$
g^\sigma_{f,f'} = g'^\sigma_{f,f'} + \sum_{f''} g'^\sigma_{f,f''} \Delta^\sigma_{f'',f''} (1 - g^\sigma)_{f'',f'}.
\tag{2.85}
$$

If a single spin-flip in the Hubbard-Stratonovich field is accepted, then we can use Eq. (2.76) to derive the new Green function from the old one by calculating:

$$
g'^\sigma = g^\sigma [1 + \Delta^\sigma(1 - g^\sigma)]^{-1}.
\tag{2.86}
$$

We use the Sherman-Morrison formula in order to calculate $[1 + \Delta^\sigma(1 - g^\sigma)]^{-1}$ which gives us the final expression:

$$
g'^\sigma_{f,f'} = g^\sigma_{f,f'} + \frac{g^\sigma_{f,\tilde{f}} \Delta^\sigma_{\tilde{f},\tilde{f}} (g^\sigma - 1)_{\tilde{f},f'}}{1 + (1 - g^\sigma)_{\tilde{f},\tilde{f}} \Delta^\sigma_{\tilde{f},\tilde{f}}}
\tag{2.87}
$$

The stabilisation of the Hirsch-Fye algorithm was mentioned in one of the previous sections. The reader should note at this point, that due to the knowledge of the Hubbard Stratonovich field configuration s, the Green function g^σ can be recalculated from scratch at any time. The recalculation has the appealing advantage, that one can compare the recalculated Green function with those which are determined by successively applying Eq. (2.87).

In an actual calculation, one starts with a warmup phase, which consists of several hundred walks through the space-time lattice (sweeps), until the system comes into equilibrium and measurements can be started. The number of sweeps has to be large enough in order to take in account the autocorrelation time. The computational effort in the above described algorithm is basically given by the upgrading of the Green function. One upgrade of the Green function after a single site spin flip is an operation which scales with $(N_c N_l)^2$. In order to achieve a complete walk through the space time lattice, the numerical cost rises to $(N_c N_l)^3$. This fact explains, why the Hirsch-Fye algorithm is very expensive when it is applied to lattice problems, i.e., the Hubbard model. Nevertheless, the Hirsch-Fye algorithm is a successful tool for application to many impurity problems.

2.8 SU(2) Symmetry Breaking

Magnetic order can be incorporated within the DCA calculation by allowing the host to develop long range AF order. The technical implementation is illustrated in Fig. 2.5. The unit cell in real space is doubled allowing for AF order. This leads to a reduced (magnetic) Brillouin zone which is depicted in Fig. 2.6 (a).
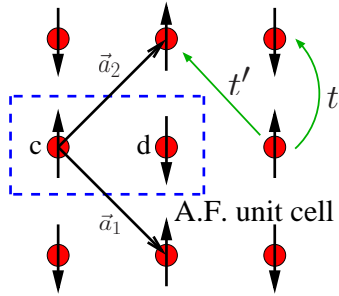
Figure 2.5   *SU(2) symmetry broken DCA calculation. AF unit cell with new basis vectors in real space. The unit cell consists of a c- and d-orbital. t and (t') indicate the nearest and next-nearest neighbour hopping.*

What follows, is a schematic derivation of the Hamiltonian with respect to the doubled unit cell, where we incorporate only the hopping term with amplitude t. Later on, we add to the corresponding Green function a next-nearest neighbour hopping term with amplitude t' (see Fig.2.5) and of course an interaction term, which is encoded in the self-energy Σ. Referring to Fig. 2.5, we consider one unit cell, which is characterised by the vector $\boldsymbol{R}$, then we can formulate the Hamiltonian with the hopping amplitude t as follows [26]:

$$
\begin{aligned}
H_0 &= -t \sum_{\boldsymbol{R}} \Bigg\{ (c_{\boldsymbol{R}}^\dagger d_{\boldsymbol{R}} + \text{ h.c. }) + (c_{\boldsymbol{R}}^\dagger d_{\boldsymbol{R}-\boldsymbol{a}_1} + \text{ h.c. }) \\
&\quad + (d_{\boldsymbol{R}}^\dagger c_{\boldsymbol{R}+\boldsymbol{a}_2} + \text{ h.c. }) + (d_{\boldsymbol{R}}^\dagger c_{\boldsymbol{R}+\boldsymbol{a}_1+\boldsymbol{a}_2} + \text{ h.c. }) \Bigg\},
\end{aligned}
\tag{2.88}
$$

with the vectors $\boldsymbol{a}_1 = \boldsymbol{a}_x - \boldsymbol{a}_y$ and $\boldsymbol{a}_2 = \boldsymbol{a}_x + \boldsymbol{a}_y$ whereas $\boldsymbol{a}_x$ and $\boldsymbol{a}_y$ are the principle vectors in real space. A Fourier transformation provides the representation of Eq. (2.88)
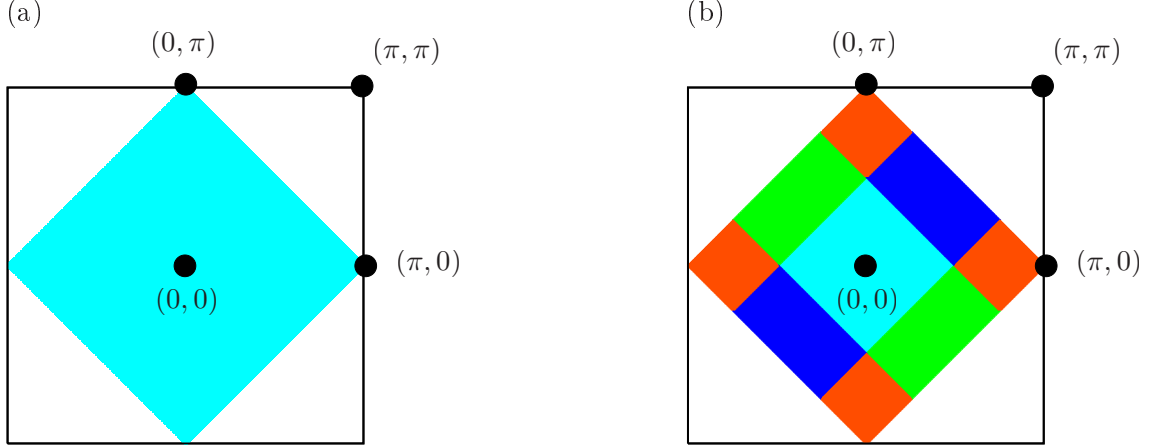
(a)

(b)

Figure 2.6 *Sketches of the magnetic Brillouin zone (BZ) for $N_c = 1$ (a) and $N_c = 4$ (b). The unit cell consists of two-orbitals (c- and d-orbital), which results in a reduction of the Brillouin zone. The colour code indicates regions in the BZ, where the self-energy is constant with respect to the momentum dependence.*

in the basis of operators $c_{\boldsymbol{K}}^{(\dagger)}$ and $d_{\boldsymbol{K}}^{(\dagger)}$ with momentum vector $\boldsymbol{K}$:

$$H_0 = -t \sum_{\boldsymbol{K}} \left(c_{\boldsymbol{K}}^{\dagger}, d_{\boldsymbol{K}}^{\dagger} \right) \begin{pmatrix} 0 & Z \\ \bar{Z} & 0 \end{pmatrix} \begin{pmatrix} c_{\boldsymbol{K}} \\ d_{\boldsymbol{K}} \end{pmatrix} \tag{2.89}$$

with $Z = Z_1 Z_2 = (1 + e^{-i\boldsymbol{K}\boldsymbol{a}_1})(1 + e^{-i\boldsymbol{K}\boldsymbol{a}_2})$. In the next step, the Hamiltonian is diagonalised by the following unitary transformation:

$$U = \frac{1}{\sqrt{2}} \begin{pmatrix} 1 & 1 \\ e^{-i\rho} & -e^{-i\rho} \end{pmatrix} \text{ with } e^{-i\rho} = e^{-i\boldsymbol{K}(\boldsymbol{a}_1 + \boldsymbol{a}_2)/2}, \tag{2.90}$$

which leads to the intermediate result:

$$H_0 = -t \sum_{\boldsymbol{K}} \quad \left(\frac{1}{\sqrt{2}}(c_{\boldsymbol{K}}^{\dagger} + e^{-i\rho}d_{\boldsymbol{K}}^{\dagger}), \frac{1}{\sqrt{2}}(c_{\boldsymbol{K}}^{\dagger} - e^{-i\rho}d_{\boldsymbol{K}}^{\dagger}) \right) \begin{pmatrix} |Z| & 0 \\ 0 & -|\bar{Z}| \end{pmatrix}$$

$$\begin{pmatrix} \frac{1}{\sqrt{2}}(c_{\boldsymbol{K}} + e^{i\rho}d_{\boldsymbol{K}}) \\ \frac{1}{\sqrt{2}}(c_{\boldsymbol{K}} - e^{i\rho}d_{\boldsymbol{K}}) \end{pmatrix} \tag{2.91}$$

$$= -t \sum_{\boldsymbol{K}} \quad Z(\boldsymbol{K})\gamma_{\boldsymbol{K}}^{\dagger}\gamma_{\boldsymbol{K}} - |Z(\boldsymbol{K})|\eta_{\boldsymbol{K}}^{\dagger}\eta_{\boldsymbol{K}}, \tag{2.92}$$

where we have introduced the operators $\gamma_{\boldsymbol{K}}^{\dagger} = c_{\boldsymbol{K}}^{\dagger} + e^{-i\rho}d_{\boldsymbol{K}}^{\dagger}$ and $\eta_{\boldsymbol{K}}^{\dagger} = c_{\boldsymbol{K}}^{\dagger} - e^{-i\rho}d_{\boldsymbol{K}}^{\dagger}$. Finally, we can identify these operators with the creation and annihilation operators of the original lattice:

$$\gamma_{\boldsymbol{K}}^{(\dagger)} = c_{\boldsymbol{k}}^{(\dagger)} \tag{2.93}$$

$$\eta_{\boldsymbol{K}}^{(\dagger)} = c_{\boldsymbol{k}+\boldsymbol{Q}}^{(\dagger)}, \tag{2.94}$$

with $\boldsymbol{Q} = (\frac{\pi}{a}, \frac{\pi}{a})$ and a is the lattice constant. This has the consequence, that the Hamiltonian can be rewritten in the basis of the reduced (magnetic) Brillouin zone:

$$H_0 = -t \sum_{\boldsymbol{k} \in \text{mBZ}} \epsilon(\boldsymbol{k}) c_{\boldsymbol{k}}^\dagger c_{\boldsymbol{k}} + \epsilon(\boldsymbol{k} + \boldsymbol{Q}) c_{\boldsymbol{k}+\boldsymbol{Q}}^\dagger c_{\boldsymbol{k}+\boldsymbol{Q}}. \tag{2.95}$$

In the spirit of the DCA approximation, the simplest realisation of the SU(2) symmetry breaking code can be performed by choosing $N_c = 1$. In this case, the coarse-grained Green function is the local Green function and the averaging is carried out over the entire magnetic Brillouin zone (see Fig. 2.6 (a)). In order to include the k-dependency of the self-energy on a basic level, we split the magnetic Brillouin zone into four cluster patches. On each cluster patch, the self-energy is constant with respect to the momentum dependence. This partition corresponds to a $N_c = 8$ DCA calculation for the paramagnetic case.

In the next step, we go beyond the non-interacting case and incorporate the self-energy. The starting point of our consideration is the Dyson equation for the interacting cluster Green function:

$$
\begin{aligned}
G_c^\sigma(\boldsymbol{K}, i\omega_m) &= \frac{1}{G_{0c}^{-1}(\boldsymbol{K}, i\omega_m) - \Sigma_c^\sigma(\boldsymbol{K}, i\omega_m)} \text{ with} \\
G_{0c}(\boldsymbol{K}, i\omega_m) &= (i\omega_m + \mu) \begin{pmatrix} 1 & 0 \\ 0 & 1 \end{pmatrix} \\
&\quad + \begin{pmatrix} 2t'(\cos(K_x) + \cos(K_y)) & Z \\ \bar{Z} & 2t'(\cos(K_x) + \cos(K_y)) \end{pmatrix} \text{ and} \\
\Sigma_c^\sigma(\boldsymbol{K}, i\omega_m) &= \begin{pmatrix} \Sigma_{11}^\sigma(\boldsymbol{K}, i\omega_m) & \Sigma_{12}^\sigma(\boldsymbol{K}, i\omega_m) \\ \Sigma_{21}^\sigma(\boldsymbol{K}, i\omega_m) & \Sigma_{22}^\sigma(\boldsymbol{K}, i\omega_m) \end{pmatrix},
\end{aligned}
\tag{2.96}
$$

where Z is defined by Eq. (2.89). We consider additionally to the Ansatz of H_0, a diagonal hopping term with amplitude t'. At this point it should be mentioned, that the momentum dependence of $G_c^\sigma(\boldsymbol{K}, i\omega_m)$ is formulated with respect to the Fourier transformed vectors $\boldsymbol{a}_1$ and $\boldsymbol{a}_2$ and therefore, the hopping dispersion for t' occurs in the diagonal elements of $G_{0c}^{-1}(\boldsymbol{K}, i\omega_m)$. The self-consistent cycle requires an initial guess of the self-energy. We set $\Sigma_c^\sigma = \Delta\sigma \begin{pmatrix} 1 & 0 \\ 0 & -1 \end{pmatrix}$ with the spin degrees of freedom $\sigma = \pm 1$ and a finite value for Δ.

The application of the unitary transformation in Eq. (2.90) leads to the Green functions with the momentum vectors $\boldsymbol{k}$ and $\boldsymbol{k} + \boldsymbol{Q}$. Equivalent to the procedure in Section 2.4, where the derivation of the lattice Green function from the cluster quantities is described, we can derive the interacting lattice Green function by replacing $G_{0c}(\boldsymbol{K}, i\omega_m)$ by the corresponding lattice Green function.

The Monte Carlo ratio and the upgrade equation of the Green function is in principle given by the previously presented results for the paramagnetic calculation but with a distinction

of both spin channels σ (see Eq. (2.87)).

On the basis of equal-time correlation functions, the calculation of the (double) occupation of site i or the magnetisation are determinable within the Hirsch-Fye algorithm. They can implemented in their canonical form. An improvement of the accuracy by reduction of the statistical error can be achieved by incorporating the time-translational invariance of the Green function $G(\tau = \tau_i - \tau_j)$ (see Section 2.7.2).

2.9 U(1) Symmetry Breaking

What follows is a brief discussion of how superconductivity can be taken into account within a DCA calculation. In the first step we assume that our U(1) symmetry breaking DCA code contains the static BCS mean-field solution. Hereby, a particle-hole transformation translates the anomalous Green function into spin-flip Green functions and the repulsive Coulomb interaction U changes its sign. The technical implementation requires a reformulation of the Monte Carlo ratio (Eq. (2.82)) as well as the upgrade formula (Eq. (2.87)) due to the occurrence of the spin-flip Green functions.

Starting point of our consideration is a general Hamiltonian with the following form [27]:

$$
\begin{aligned}
H &= \sum_\sigma \int \mathrm{d}^3 r \psi_\sigma^\dagger(\boldsymbol{r}) \left(-\frac{\nabla^2}{2m} - \mu \right) \psi_\sigma(\boldsymbol{r}) \\
&+ \sum_{\sigma,\sigma'} \int \mathrm{d}^3 r' \int \mathrm{d}^3 r \psi_\sigma^\dagger(\boldsymbol{r}) \psi_{\sigma'}^\dagger(\boldsymbol{r}') v(\boldsymbol{r} - \boldsymbol{r}') \psi_{\sigma'}(\boldsymbol{r}') \psi_\sigma(\boldsymbol{r}),
\end{aligned}
\tag{2.97}
$$

where the field operators $\psi_\sigma^{(\dagger)}$ destroy (create) an electron with spin σ at site $\boldsymbol{r}$. Bardeen, Cooper and Schrieffer proposed in their BCS theory a simplified interaction term, which incorporates only an attractive short-range interaction. This contact interaction is given by:

$$
v(\boldsymbol{r} - \boldsymbol{r}') = -\frac{g}{2}\delta(\boldsymbol{r} - \boldsymbol{r}'),
\tag{2.98}
$$

with a positive coupling constant g. The quartic term in Eq. (2.97) can be simplified by a common mean-field decomposition[2], which neglects fluctuation of the form $\psi_\uparrow^\dagger \psi_\downarrow^\dagger - \langle \psi_\uparrow^\dagger \psi_\downarrow^\dagger \rangle$. With the abbreviation $\Delta = \frac{g}{\Omega} \sum_{\boldsymbol{k}} \langle c_{-\boldsymbol{k}\downarrow} c_{\boldsymbol{k}\uparrow} \rangle$, where Ω is the volume, the Hamiltonian in Eq. (2.97) may be written in momentum space as:

$$
H_0 = \sum_{\boldsymbol{k}} \epsilon(\boldsymbol{k}) c_{\boldsymbol{k}\uparrow}^\dagger c_{\boldsymbol{k}\uparrow} + \epsilon(-\boldsymbol{k}) c_{-\boldsymbol{k}\downarrow}^\dagger c_{-\boldsymbol{k}\downarrow} - \sum_{\boldsymbol{k}} \Delta(\boldsymbol{k}) c_{\boldsymbol{k}\uparrow}^\dagger c_{-\boldsymbol{k}\downarrow}^\dagger + \text{h.c.}.
\tag{2.99}
$$

---

[2] $AB = (A - \langle A \rangle)(B - \langle B \rangle) + A\langle B \rangle + B\langle A \rangle - \langle A \rangle \langle B \rangle \overset{MF}{=} A\langle A \rangle + B\langle B \rangle$

The Hamiltonian H_0 suggests that we have to introduce additional Green functions, which destroy the $U(1)$ symmetry. An elegant notation is given by the Nambu formalism [28]:

$$G(\boldsymbol{k}, \tau) = \begin{pmatrix} -\langle \mathcal{T} c_{\boldsymbol{k}\uparrow}(\tau) c_{\boldsymbol{k}\uparrow}^\dagger(0) \rangle & -\langle \mathcal{T} c_{\boldsymbol{k}\uparrow}(\tau) c_{-\boldsymbol{k}\downarrow}(0) \rangle \\ -\langle \mathcal{T} c_{-\boldsymbol{k}\downarrow}^\dagger(\tau) c_{\boldsymbol{k}\uparrow}^\dagger(0) \rangle & -\langle \mathcal{T} c_{-\boldsymbol{k}\downarrow}(\tau) c_{-\boldsymbol{k}\downarrow}^\dagger(0) \rangle \end{pmatrix}, \tag{2.100}$$

which holds the Dyson equation:

$$G(\boldsymbol{k}, i\omega_m) = [i\omega_m \sigma_0 - (\epsilon_{\boldsymbol{k}} - \mu)\sigma_3 - \Sigma_c(\boldsymbol{K}, i\omega_m)]^{-1}, \tag{2.101}$$

whereat σ_i corresponds to the Pauli-spin matrices. The diagonal parts of the Nambu-matrix $\Sigma_c(\boldsymbol{K}, i\omega_m)$ describe quasiparticles renormalisations and the off-diagonal parts contains information about the $\boldsymbol{K}$- and frequency dependence of the pairing state. The interaction of the electrons on the f-sites are taken into account by adding the Hamiltonian operator $H_U = U \sum_i (c_{i\uparrow}^\dagger c_{i\uparrow} - \frac{1}{2})(c_{i\downarrow}^\dagger c_{i\downarrow} - \frac{1}{2})$ to the BCS Hamiltonian:

$$H = H_0 + H_U. \tag{2.102}$$

Consider now a canonical particle-hole transformation in one spin channel:

$$\gamma_{i\uparrow}^\dagger = c_{i\uparrow}^\dagger \tag{2.103}$$
$$\gamma_{i\downarrow}^\dagger = c_{i\downarrow}, \tag{2.104}$$

which leads to a reformulation of the Hamiltonian in Eq. (2.102):

$$\begin{aligned} H &= \sum_{\boldsymbol{k}} \epsilon(\boldsymbol{k}) \gamma_{\boldsymbol{k}\uparrow}^\dagger \gamma_{\boldsymbol{k}\uparrow} + \epsilon(-\boldsymbol{k})(1 - \gamma_{-\boldsymbol{k}\downarrow}^\dagger \gamma_{-\boldsymbol{k}\downarrow}) \\ &+ \sum_{\boldsymbol{k}} \Delta(\boldsymbol{k}) \gamma_{\boldsymbol{k}\uparrow}^\dagger \gamma_{-\boldsymbol{k}\downarrow} + \sum_{\boldsymbol{k}} \Delta(\boldsymbol{k}) \gamma_{-\boldsymbol{k}\downarrow}^\dagger \gamma_{\boldsymbol{k}\uparrow} \\ &- U \sum_i (\gamma_{i\uparrow}^\dagger \gamma_{i\uparrow} - \frac{1}{2})(\gamma_{i\downarrow}^\dagger \gamma_{i\downarrow} - \frac{1}{2}). \end{aligned} \tag{2.105}$$

Due to the particle-hole transformation the anomalous Green functions are replaced by spin-flip Green functions and the repulsive Coulomb interaction becomes an attractive potential. Naturally, these changes have an influence on the Monte-Carlo ratio (see Eq. (2.82)) as well as on the upgrade formula in Eq. (2.87).

In the attractive case, the Hubbard-Stratonovich (HS) field ϕ couples to the charge in order to avoid a complex HS field. The interaction term may be compactly rewritten as:

$$H_U = \gamma^{N_c} \sum_{\boldsymbol{s}} e^{\alpha \boldsymbol{s}(n_{i\uparrow} + n_{i\downarrow} - 1)}$$

with $\gamma = \frac{1}{2}$ and $e^{\Delta\tau U/2} = \cosh(\alpha)$. $\tag{2.106}$

By regarding Eq. (2.82), the probability of acceptance of a new Hubbard-Stratonovich configuration after a single-site spin flip is determined by:

$$R_{\boldsymbol{s} \to \boldsymbol{s}'} = \det[g(g')^{-1}] e^{\pm 2\alpha}. \tag{2.107}$$

The plus(minus) sign depends on the actual spin flip, i.e., a $+(-)$ sign occurs if one tries to flip a down (up) spin to an up (down) spin.

The evaluation of the determinant provides the final result for the update ratio in the Hirsch-Fye algorithm:

$$R_{\boldsymbol{s}\to\boldsymbol{s}'} = e^{\pm 2\alpha}\left\{\prod_\sigma (1+\Delta_{\tilde{f}\sigma})(1-g)_{\tilde{f}\sigma,\tilde{f}\sigma} - \prod_\sigma \Delta_{\tilde{f}\sigma}(1-g)_{\tilde{f}\sigma,\tilde{f}-\sigma},\right\} \tag{2.108}$$

where we have introduced the superindex $\tilde{f}$ which indicates the space coordinate i and the time index l where the spin flip has taken place. At this point, we would like to point out, that the above ratio boils down to the generic ratio in Eq. (2.82) if the spin-flip Green functions are zero.

Finally, the upgrade formula in Eq. (2.87) becomes, of course, more complicated due to the existence of the spin-flip Green functions. Assume that a single spin flip at superindex $\tilde{f}$ is performed, then the upgraded Green function g' at superindices f, f' is given as follows:

$$\begin{aligned}
g'_{f,f'} &= g_{f,f'} - \frac{g_{f,\tilde{f}\uparrow}\Delta^\uparrow_{\tilde{f},\tilde{f}}(1-g)_{\tilde{f}\uparrow,f'}}{1+(1-g)_{\tilde{f}\uparrow,f\uparrow}\Delta^\uparrow_{\tilde{f},\tilde{f}}}\\
&\quad - \frac{g_{f,\tilde{f}\downarrow}\Delta^\downarrow_{\tilde{f},\tilde{f}} - \frac{(-g)_{\tilde{f}\uparrow,\tilde{f}\downarrow}\Delta^\downarrow_{\tilde{f},\tilde{f}}}{1+(1-g)_{\tilde{f}\uparrow,\tilde{f}\uparrow}\Delta^\uparrow_{\tilde{f},\tilde{f}}}g_{f,\tilde{f}\uparrow}\Delta^\uparrow_{\tilde{f},\tilde{f}}}{1+(1-g)_{\tilde{f}\downarrow,\tilde{f}\downarrow}\Delta^\downarrow_{\tilde{f},\tilde{f}} - \frac{(-g)_{\tilde{f}\uparrow,\tilde{f}\downarrow}\Delta^\downarrow_{\tilde{f},\tilde{f}}(-g)_{\tilde{f}\downarrow,\tilde{f}\uparrow}\Delta^\uparrow_{\tilde{f},\tilde{f}}}{1+(1-g)_{\tilde{f}\uparrow,\tilde{f}\uparrow}\Delta^\uparrow_{\tilde{f},\tilde{f}}}}\\
&\quad \cdot \left[(1-g)_{\tilde{f}\downarrow,f'} - \frac{(-g)_{\tilde{f}\downarrow,\tilde{f}\uparrow}\Delta^\uparrow_{\tilde{f},\tilde{f}}}{1+(1-g)_{\tilde{f}\uparrow,\tilde{f}\uparrow}\Delta^\uparrow_{\tilde{f},\tilde{f}}}(1-g)_{\tilde{f}\uparrow,f'}\right],
\end{aligned} \tag{2.109}$$

where $\Delta^\sigma_{f,f}$ is defined by Eq. (2.84). One should keep in mind, that the definition of $\Delta^\sigma_{f,f}$ has to be adjusted when the simulation starts from the non-interacting system where all Ising spins have the value zero. Evidently, the above upgrade equation for the Green function reduces to Eq. (2.87) if the spin-flip Green functions are zero.

Observables

In this section, we briefly present some generic observables which could be determined within the Hirsch-Fye algorithm. As mentioned above, the Green functions in the Hirsch-Fye algorithm are described in the basis where the anomalous Green functions ($c^{(\dagger)}$-basis) are expressed by spin-flip Green functions ($\gamma^{(\dagger)}$-basis) which of course has a direct influence on the observables.

- The occupation number is given in the ($\gamma^{(\dagger)}$-basis) by:

$$\langle n \rangle = (1 - \langle \gamma_{i\uparrow}\gamma_{i\uparrow}^\dagger \rangle)\langle \gamma_{i\downarrow}\gamma_{i\downarrow}^\dagger \rangle. \tag{2.110}$$

- The double occupation in the ($\gamma^{(\dagger)}$-basis) can be derived from the expression $\langle n_{i\uparrow} n_{i\downarrow} \rangle = \langle c_{i\uparrow}^\dagger c_{i\uparrow} c_{i\downarrow}^\dagger c_{i\downarrow} \rangle$. As mentioned in Section 2.7.2, the fermions interact only with the auxiliary field, and therefore, we can apply Wicks theorem [29] for a fixed Hubbard-Stratonovich field configuration. The two-particle Green function reduces to a product of single-particle Green functions (see Eq. (2.70)):

$$\langle n_{i\uparrow} n_{i\downarrow} \rangle = (1 - \langle \gamma_{i\uparrow} \gamma_{i\uparrow}^\dagger \rangle) \langle \gamma_{i\downarrow} \gamma_{i\downarrow}^\dagger \rangle + \langle \gamma_{i\downarrow} \gamma_{i\uparrow}^\dagger \rangle \langle \gamma_{i\uparrow} \gamma_{i\downarrow}^\dagger \rangle. \tag{2.111}$$

- The s-wave order parameter is a result of the correlation functions of the anomalous Green function, which can be readily written in the ($\gamma^{(\dagger)}$-basis) as:

$$\Delta_{SC}^s = -\langle \gamma_{i+\#_x\downarrow} \gamma_{i\uparrow}^\dagger \rangle - \langle \gamma_{i\downarrow} \gamma_{i+\#_x\uparrow}^\dagger \rangle - \langle \gamma_{i+\#_y\downarrow} \gamma_{i\uparrow}^\dagger \rangle - \langle \gamma_{i\downarrow} \gamma_{i+\#_y\uparrow}^\dagger \rangle, \tag{2.112}$$

with the index $\#_{x,y}$ which represents the adjacent lattice sites in x- or y-direction from lattice site i.

- The superconducting d-wave order differs from the s-wave order parameter only in the underlying symmetry. It may be written as:

$$\Delta_{SC}^d = -\langle \gamma_{i+\#_x\downarrow} \gamma_{i\uparrow}^\dagger \rangle - \langle \gamma_{i\downarrow} \gamma_{i+\#_x\uparrow}^\dagger \rangle + \langle \gamma_{i+\#_y\downarrow} \gamma_{i\uparrow}^\dagger \rangle + \langle \gamma_{i\downarrow} \gamma_{i+\#_y\uparrow}^\dagger \rangle. \tag{2.113}$$

Analytical Continuation – Maximum Entropy Method

<div style="text-align: right">3</div>

3.1 Analytical Continuation

In the following chapter, we are going to describe the idea of analytical continuation of Matsubara functions to the real frequency axis. The quantum Monte Carlo technique provides correlation functions as functions of inverse temperature or imaginary time: $G(\tau) = -\langle \mathcal{T}\hat{\mathcal{O}}(\tau)\hat{\mathcal{O}}^\dagger(0)\rangle$. In order to compare the information of these correlations function with experimental data, one has to extract the real frequency dependencies of such quantities.

Analytical continuation is based on basic concepts of the theory of analytical functions. Let us review overcome these concepts by considering the one- and two-particle Green functions which exhibit the following periodicity:

$$G(\tau) = \mp G(\tau + \beta), \tag{3.1}$$

where the upper (lower) case holds for the fermionic (bosonic) case. The Green function is uniquely defined in the interval $\tau \in [0, \beta)$. The Fourier coefficients are the Matsubara functions $G(i\omega_m)$ which depend on imaginary frequency:

$$G(\tau) = \frac{1}{\beta} \sum_{\omega_n} e^{-i\omega_m \tau} G(i\omega_m) \tag{3.2}$$

$$G(i\omega_m) = \int_0^\beta d\tau e^{i\omega_m \tau} G(\tau). \tag{3.3}$$

The sum is carried out over Matsubara frequencies $\omega_m = (2m + 1)\pi/\beta$ for fermions and $\omega_m = 2m\pi/\beta$ for bosons, where $m \in \mathbb{Z}$. With the explicit form of the spectral function $A(\omega)$ in the Lehmann representation, Eq. (3.3) may be rewritten as:

$$G(i\omega_m) = \int_{-\infty}^{+\infty} \frac{A(\omega)}{i\omega_m - \omega} d\omega \tag{3.4}$$

In the following, we can define the Green function $G(z)$:

$$G(z) \equiv \int_{-\infty}^{+\infty} d\omega' \frac{A(\omega')}{z - \omega'}, \tag{3.5}$$

with complex energies z. This Green function is an analytic function in the upper and the lower complex plane and exhibits poles on the real frequency axis. Per construction, $G(i\omega_m)$ is concordant with $G(z)$ at all Matsubara frequencies $i\omega_m$ which allows us to apply a result from complex analysis: if two functions coincide on an infinite set of points then they are fully identical functions within the entire complex plane [30]. Hence, the Matsubara function $G(i\omega_m)$ or, equivalently, $G(\tau)$ can be uniquely extend to the whole complex plane. In order to obtain the spectral function $A(\omega)$, we define the retarded (advanced) Green function $G^{R(A)}(\omega) = G(\omega \pm i\eta)$ and the analytical continuation is performed by:

$$G^{R(A)}(\omega) = G(i\omega_m \to \omega \pm i\eta) \text{ and } \mp \frac{1}{\pi} Im[G^{R(A)}(\omega)] = A(\omega) \tag{3.6}$$

The single-particle spectral function $A(\omega)$ is positive definite

$$A(\omega) \geq 0, \tag{3.7}$$

and a sum rules ensures the normalisation

$$\int_{-\infty}^{+\infty} d\omega \, A(\omega) < \infty, \tag{3.8}$$

which gives $A(\omega)$ the appealing property that it can be interpreted as a probability distribution. If we apply a Fourier transformation to Eq. (3.5), then we can write:

$$G(\tau) = \mp \int d\omega \frac{1}{\beta} \sum_{\omega_n} \frac{e^{-i\omega_m\tau}}{i\omega_m - \omega} A(\omega) \tag{3.9}$$

$$= \int d\omega \frac{e^{-\omega\tau}}{e^{-\beta\omega} \pm 1} A(\omega) \tag{3.10}$$

$$= \int d\omega K(\tau, \omega) A(\omega) \tag{3.11}$$

In the last step, we adopt the kernel $K(\tau, \omega)$:

$$K(\tau, \omega) = \begin{cases} e^{-\omega\tau} / \left(e^{-\omega\beta} + 1 \right), & \text{fermions} \\ e^{-\omega\tau} / \left(e^{-\omega\beta} - 1 \right), & \text{bosons.} \end{cases} \tag{3.12}$$

In principle, Eq. (3.11) displays the relation between the imaginary time Green function $G(\tau)$ and the spectral function $A(\omega)$. Hereby, the analytical continuation can be understood as an inversion of the functional expression $\boldsymbol{K}[A(\omega)] = G(\tau)$. An analytical approach in order to perform the inverse Laplace transformation is not possible and from the numerical point of view, a straightforward inversion leads to unreliable results. The reason is given by numerical instabilities, which come from the extremely large condition number of

the kernel. This is shown by a singular value decomposition of the kernel $K = UDV$ into an orthogonal matrix U, a diagonal matrix D and an upper triangular matrix V. The diagonal matrix D exhibits very large and small eigenvalues, which would be mixed up during a simple matrix inversion of the kernel function. Additionally, the input data is incomplete and noisy, which makes the inversion of the Laplace transformation even worst. Finally, correlation effects of the input data between different bins and time slices could cause an over-fitting of the data. This mean, that one extracts structures out of the QMC spectrum, which are not actually present. All these arguments demonstrate why the inversion of the Laplace transformation is an ill-defined numerical task.

3.2 Maximum Entropy Method

The state of the art strategy in order to tackle the inverse Laplace transformation is the Maximum Entropy method [24, 31, 32]. This method was first introduced in order to improve noisy astronomical data [33]. In the meantime, it has become a standard tool for analysis of statistical data [34]. This method was also successfully applied to systems of many-body problems, i.e., to the one- and two dimensional Hubbard model [35, 36, 37, 38, 39, 40], to the single impurity Anderson model [41], and to spin systems like the spin-1/2-Heisenberg model [42, 43].

In the following section, we emphasise the basic idea of the classical Maximum Entropy method, before we summarise a stochastic implementation of the analytical continuation which was formulated by K. Beach. [25]

Generally, the Maximum Entropy method is based on the idea of maximising, a so-called aposteriori probability as a function of the given information content. This means in our case, that the Maximum Entropy method estimates the most probable spectral function A with respect to the given input data G and an additional prior knowledge of the spectral function which is encoded in a default model m, i.e., this corresponds to the maximisation of the conditional probability of $P(A|G, m)$. The conditional probability $P(A|G, m)$ can be computed in the framework of Bayesian statistic [44], which states that $P(A|G, m)$ is nothing else but,

$$P(A|G, m) = \frac{P(G|A, m)\ P(A|m)}{P(G|m)}. \tag{3.13}$$

The right hand side of Eq. (3.13) consists of the Likelihood function $P(G|A, m)$, the entropic prior $P(A|m)$ and the evidence $P(G|m)$ which can be written in terms of the Likelihood function and the entropic prior:

$$P(G|m) = \int \mathcal{D}A\ P(G|Am)\ P(A|m), \tag{3.14}$$

and represents only a normalisation factor. The maximisation of the aposteriori probability $P(A|G, m)$ is, thus, equal to the simultaneous maximisation of the Likelihood function and the entropic prior.

Let us discuss the Likelihood function and the entropic prior in detail:

P(G|A,m): Generally, the Likelihood function represents a procedure which allows to fit parameters to a given data set. In our case, this procedure poses the question: what is the most probable data set $\bar{G}$ which differs as little as possible from a data set G which is extracted from a given spectral function A by application of the Eq. (3.11)? The Likelihood function [45] gives us the correct answer:

$$P(\bar{G}|A, m, \alpha) = \frac{1}{(2\pi)^{N_l/2}\sqrt{\det C}}e^{-\frac{1}{2}\chi^2(A)} \ \ \text{with}$$

$$\chi^2(A) = \sum_{\tau,\tau'}\left(\bar{G}_\tau - \sum_i K_{\tau,i}A_i\right)C_{\tau,\tau'}^{-1}\left(\bar{G}_{\tau'} - \sum_i K_{\tau',i}A_i\right). \tag{3.15}$$

The matrix C is the covariance matrix and N_l represents the number of time slices (see Sec. 2.7.1) and α serves as a statistical parameter. Obviously, χ^2 in Eq. (3.15) is independent from the default model m and α and the conditional probability is normalised to one. In the spirit of the maximum Likelihood approach, the best solution of the inverse Laplace transformation is given by the $\bar{G}$ which minimises Eq. (3.15). Hereby, the apriori knowledge is totally neglected and the input data will be over-fitted.

P(A|m): The apriori knowledge about the input data set is encoded in a default model m. The default model should not underlay any constraints except some elementary conditions which ensure that the default model (or the spectral function A) can be understood as a probability distribution. In the case of non-existence of prior information the prior entropy is given by $P(A|m) = const.$

On the basis of general considerations of the Maximum Entropy axioms [33], it is possible to derive a close expression for the information content of the spectral function with respect to a default model. Hereby, the Maximum Entropy axioms can be summarised by the key words: subset independence, coordinate invariance, system independence and scaling properties. The apriori probability for a positive additive distribution function is determined by:

$$P(A|m) = \frac{1}{Z_s}e^{\alpha S}, \tag{3.16}$$

with Z_s serves as a normalisation factor: $\int \mathcal{D}A \ P(A|m) = 1$ and α is a free statistical parameter. The entropy can be written as [33]:

$$S = \int_{-\infty}^{\infty} d\omega \ \left[A(\omega) - m(\omega) - A(\omega)\ln\left(\frac{A(\omega)}{m(\omega)}\right)\right]. \tag{3.17}$$

The entropy describes the difference between the spectral function A and the given default model m. If the default model is equal to $A(\omega)$ the entropy yields zero and becomes

negative otherwise. The combination of the Likelihood function and the apriori entropy leads to an expression for the aposteriori probability [46, 47]:

$$P(A|G) \sim e^{\alpha S - \chi^2/2}, \tag{3.18}$$

which exhibits a competition between $P(G|A, m)$ and $P(A|m)$. The first term in the exponent take account of the information entropy, i.e., the Maximum Entropy method would just prioritise the spectrum which is the most indefinite against prior knowledge and the second term prioritise the classical minimisation of χ^2, which corresponds to a classical fit of a data set to a given model.

3.2.1 Stochastic Analytical Continuation

Another way to perform the continuation of correlation functions from imaginary time to real frequencies was shown by K. Beach [25]. In particular, Beach could identify the maximum entropy method as a special limit of stochastic analytical continuation. Hereby, the continuation problem is mapped onto a system of interacting classical fields $n(x)$. The thermally averaged value of this field is given by:

$$\langle n(x) \rangle = \frac{1}{Z} \int \mathcal{D}n \, n(x) \, e^{-\alpha H[n]}, \tag{3.19}$$

where Z severs as a normalisation factor and the integral has to be taken over all field configurations $n(x)$. The underlying Hamiltonian is chosen in such a way, that the ground state solution corresponds to the unregularised inversion of the input data with the regularisation parameter α, which can be interpreted as a fictive inverse temperature. In the high temperature limit ($\alpha \to 0$), the integral in Eq. (3.19) averages all field configurations and the average is independent from the input data $G(\tau)$. These two extrema obviously correspond to the over-fitting ($Q \sim \chi^2[A]$) and over-smoothing limits ($Q \sim -S[A]$) which were described in Sec. 3.2. The evaluation of the integral expression in Eq.(3.19) requires a discretisation of $\mathcal{D}n$ and a Monte Carlo technique is utilised in order to tackle the huge phase space. During the Monte Carlo procedure each field configuration $C = \{r_\gamma, a_\gamma\}$ is parametrised by a set of so-called walkers which exhibit a given residue $r_\gamma > 0$ and coordinate $0 \leq a_\gamma \leq 1$:

$$n_C(x) = \sum_\gamma r_\gamma \, \delta(x - a_\gamma) \tag{3.20}$$

The Monte Carlo procedure starts with an arbitrary start configuration and new configurations are suggested by varying the residues and coordinates of the walkers. A new configuration causes an energy shift which is determined by H and the acceptance of a new configuration is controlled with the usual Metropolis algorithm [48]. The updating process incorporates the detailed balance criterion and a normalisation constraint on the classical field ($\sum_\gamma r_\gamma = const$) which secures the normalisation of the spectral function.

As mentioned before, the parameter α can be connected to an artificial temperature. Simulations for different temperatures are carried out simultaneously with a parallel tempering technique [49]. Adjacent temperature layers can interchange their configurations which leads to an effective updating scheme. If the systems enter into equilibrium one can starts the measurements of the internal energy with respect to the temperature ($\{U(\alpha_p) = \langle H[n] \rangle_{\alpha_p} : \ p = 0, \ldots, N\}$), where N characterises the number of temperature layers. Furthermore, the specific heat can be obtained from the derivative of the internal energy with respect to the temperature and a phase transition would cause a jump in the specific heat at a particular energy $E^\star$. Beach argues, that the correct spectral function $A(\omega)$ is given by a sum over all field configurations $\langle n(x) \rangle_E$ which have the energy $E < E^\star$.

3.2.2 Analytical Continuation of two-particle correlation functions

The following section presents some comments on the usage of the Maximum Entropy method in the case of two-particle correlation functions. As we have seen in Eq. (3.11), the Kernel exhibits in the bosonic case a divergence for $\omega = 0$. A simple symmetrisation of the Kernel function can circumvent this problem:

$$
\begin{aligned}
\chi(\boldsymbol{q}, \omega) &= -\chi(\boldsymbol{q}, -\omega) \\
&= \frac{1}{\pi} \int_{-\infty}^{\infty} d\omega \, \frac{e^{-\tau\omega}}{1 - e^{-\beta\omega}} \, \chi(\boldsymbol{q}, \omega) \\
&= \frac{1}{\pi} \int_{-\infty}^{\infty} d\omega \, \frac{e^{-\tau\omega}}{1 - e^{-\beta\omega}} \, \chi(\boldsymbol{q}, \omega) \, \tanh(\frac{\beta\omega}{2}) \, \coth(\frac{\beta\omega}{2}) \\
&= \frac{1}{\pi} \int_{-\infty}^{\infty} d\omega \, \frac{e^{-\tau\omega}}{1 + e^{-\beta\omega}} \, \underbrace{\chi(\boldsymbol{q}, \omega) \, \coth(\frac{\beta\omega}{2})}_{\tilde{\chi}(\boldsymbol{q}, \omega)} \\
&= \frac{1}{\pi} \left[\int_0^\infty d\omega \, \frac{e^{-\tau\omega}}{1 + e^{-\beta\omega}} \, \tilde{\chi}(\boldsymbol{q}, \omega) + \int_0^\infty d\omega \, \frac{e^{(\tau-\beta)\omega}}{1 + e^{-\beta\omega}} \, \tilde{\chi}(\boldsymbol{q}, \omega) \right] \\
&= \int_0^\infty d\omega \, \underbrace{\frac{e^{-\tau\omega} + e^{(\tau-\beta)\omega}}{\pi(1 + e^{-\beta\omega})}}_{K(\omega, \tau)} \, \tilde{\chi}(\boldsymbol{q}, \omega).
\end{aligned}
$$

(3.21)

(3.22)

The symmetrisation yields a redefinition of the susceptibility $\chi(\boldsymbol{q}, \omega)$ (Eq. (3.21)) which has to be taken into account in the definition of the dynamical structure factor $S(\boldsymbol{q}, \omega)$:

$$
S(\boldsymbol{q}, \omega) = \frac{\chi(\boldsymbol{q}, \omega)}{1 - e^{-\beta\omega}} = \frac{\tilde{\chi}(\boldsymbol{q}, \omega)}{1 + e^{-\beta\omega}} \tag{3.23}
$$

Finally, some general important notes about the Maximum Entropy method should be mentioned. As described in Sec. 3.2, the resulting spectral function should be interpreted as a probability distribution. That means in detail, that different sharp structures in the spectrum indicate regions with high or low probability for finding a real peak. Although

the total weight of the spectral function is conserved, statements about the absolute value and the shape of a peak have to be taken carefully. Especially, the nature of broadened and smeared out features in the spectra are hard to figure out. They can be a consequence of a bad resolution due to the error of the QMC data or they indeed originate from a uniform distribution. In order to avoid such misinterpretations it is important to keep the simulations running until no visible changes in the spectra occur.

The single-band Hubbard model

<div style="text-align: right; font-size: large;">4</div>

The single-band Hubbard model is defined in the language of second quantisation by [50, 51, 52]

$$H = -\sum_{ij\sigma} t_{ij} c_{i\sigma}^{\dagger} c_{j\sigma} + U \sum_{i} n_{i\uparrow} n_{i\downarrow}, \tag{4.1}$$

with the hopping amplitude t_{ij} and the Hubbard interaction U. In this thesis the energy scale of the Hubbard Hamiltonian is set by the nearest-neighbour hopping amplitude t and throughout we consider $U = 8t$. A visualisation of the different energy contributions is depicted in Fig. 4.1. The Hubbard model is nowadays one of the standard models used in order to describe the physics of strongly-correlated electron systems. In the beginning, it was assigned to described the magnetism of strongly correlated, itinerant electrons in narrow band materials. In the special case of a half-filled system with one hole and an infinite value of the Coulomb interaction, the Hubbard model shows for $d \leq 2$ a completely spin-polarised, i.e., ferromagnetic ground state [53]. But is was shown that the ferromagnetic solution on a primitive cubic or cubic body-centered system does not remain completely stable. In the last several years it has become more apparent, that antiferromagnetic correlation plays an even more important role. Apart from a pure theoretical description, the Hubbard model is considered to describe the physics of 3d-transition metals, such as high-temperature superconductors (HTSC) [54]. These ceramics consist in general of copper oxide compositions. Inelastic neutron scattering experiments showed that the electrical properties of these materials are dominated by the physics within the two dimensional copper oxide plans. The electrical resistivity perpendicular to the copper oxide planes is $10^2 - 10^5$ order of magnitudes higher than within the planes. [55] This high anisotropy can be justified by the crystal structure of these materials. The HTSCs consists of layers of copper oxide which are separated by inter-layer atoms, i.e., lanthanum or yttrium. Due to the crystal structure, these materials can be effectively regarded as two dimensional systems. Furthermore, a detailed close-up of the electronical structure yields an even more bizarre property of the conductivity of the HTSCs. In the case of La_2CuO_4, one finds the
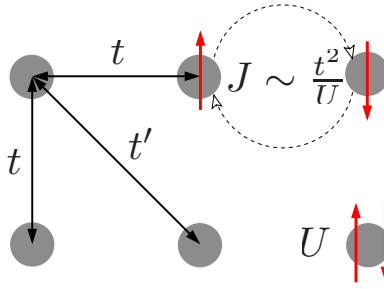
Figure 4.1   *Schematic presentation of the one-band Hubbard model with nearest neigh-
bour hopping t, next-nearest neighbour hopping t', on-site Coulomb interaction U for
double occupied lattice sites and exchange interaction $J \sim \frac{t^2}{U}$.*

copper atoms in the configuration $3d^9$. Due to the crystal splitting of the $3d$-states, one
obtains a d-configuration with one hole in the $d_{x^2-y^2}$-state. This state hybridises with the
p_x- and p_y-state of the oxygen atoms and forms a band close to the Fermi-energy. This
configuration would normally lead to a metallic state because one can add/remove addi-
tional electrons/holes to the half-filled band. But at low temperatures, the phase-diagram
of such HTSCs exhibits an antiferromagnetic insulating phase. Later on, we can justify this
behaviour by the strong Coulomb interaction which enforces a metal-insulator transition.
At higher doping (see Fig. 4.2), the HTSCs are characterised by a metallic behaviour with
a few of exotic properties, e.g., the existence of a pseudo-gap regime. The superconducting
phase is located at roughly optimal doping and captures a dome-like shape. By further
doping one reaches a normal metallic regime which can be described by the Fermi-liquid
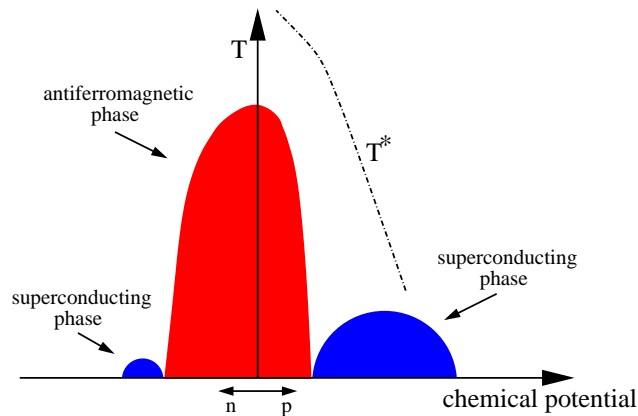
Figure 4.2   *Sketch of the generic temperature versus doping phase-diagram of the high-
temperature superconductors. The abbreviations 'n' and 'p' indicate the electron and hole
doping regimes, respectively. The pseudo-gap regime is located under the dashed-dotted
line and is connected to a typical temperature $T^\star$.*
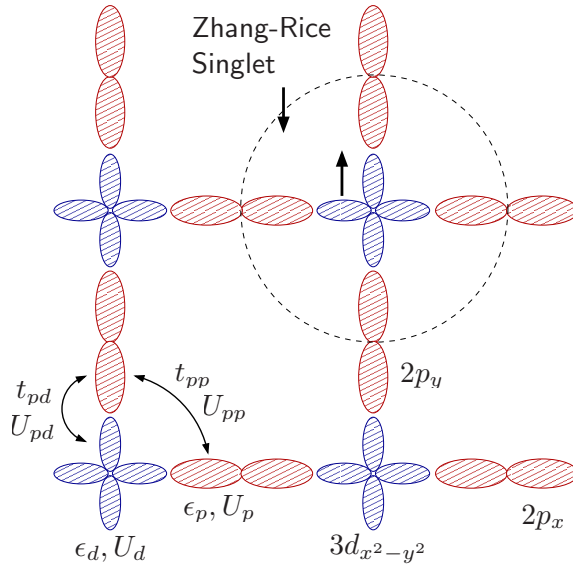
Figure 4.3 *Sketch of the interaction und hopping terms of the three-band Hubbard model. The copper $d_{x^2-y^2}$ (oxygen $2p_x$ and $2p_y$) orbitals are indicated by the red (blue) ellipses. The hopping amplitudes between the orbitals are given by t_{pp} and t_{pd} and U_{pp}, U_{pd}, U_p and U_d characterise the Coulomb interaction between electrons of the p-, pd-, and d-orbitals. The energy cost of adding or removing an electron on the d- or p-orbitals are defined by ϵ_d and ϵ_p. Holes on the oxygen and copper orbitals could form a singlet (Zhang-Rice singlet) which can move through the lattice in a similar way as a single hole in an effective one-band Hubbard model with strong interaction U [56].*

theory.

A more realistic description of the electronic structure of the HTSCs can be achieved by the three-band Hubbard model or Emery model [57] which incorporates the electronic degrees of freedom of the d- and p-orbitals. The $d_{x^2-y^2}$ copper orbitals are separated from the $2p_x$ and $2p_y$ oxygen orbitals by the crystal field. Hereby, the oxygen orbitals gather the additional charge carriers (holes) when the system is doped away from half-filling. The holes on the oxygen orbitals couple parallel (singlet) or anti-parallel (triplet) to the holes on the copper orbitals. In the strong coupling limit, one can show in the framework of second order perturbation theory, that the holes of the d- and p-orbitals build a Zhang-Rice singlet [56]. This configuration is energetically more favoured than a triplet state. In order to reduce the complexity of the system, one integrates out the electronical degrees of freedom of the oxygen orbitals and considers an effective model which only incorporates the low energy physics of the singlet state and neglects the high energy excitations due to the triplet configurations. Therefore, the single-band Hubbard model is expected to describe the physics of the high-temperature superconductors. Nevertheless, the properties of the

HTSCs impose several requirements on the model. First, the model has to describe the interaction of strongly correlated electrons. Furthermore, the model should exhibit an insulating antiferromagnetic phase at half-filling which persists to higher dopings. Last but not least, it has to show a transition from the Mott-insulator to a paramagnetic metal and superconducting state when additional charge carriers are introduced. The transition from the metallic state to the superconducting state is still not clearly understood and is still under investigation [11, 58].

The single-band Hubbard model, which is introduced in Eq. (4.1), reveals several basic symmetries. The Hubbard Hamiltonian is invariant under a global SU(2) and U(1) symmetry which enforces spin and particle conservation. In particular, the z-component of the spin is conserved and without lost of generality the magnetisation m can be set to a positive value. On the bipartite lattice, the single-band Hubbard Hamiltonian, with only a nearest-neighbour hopping amplitude, exhibits particle-hole symmetry which can be broken by adding a next-nearest neighbour hopping term to the Hamiltonian.

The first term of single-band Hubbard model describes the hopping of the electrons whereas the second term of Eq. (4.1) represents the interaction of the electrons which occupy the same lattice site. The model can be solved only in very limiting cases. In one dimension, the Bethe Ansatz provides an analytical solution which was already proposed in the year 1968 by Lie und Wu [59]. In the limit of infinite dimension the Hubbard model can be exactly mapped onto the impurity Anderson model which can be solved with the quantum Monte Carlo technique (see section 2.1). This means that even in two dimension, with the exceptions of the scenarios described above, an exact solution has not been found. The reason is given by the combination of the two parts in the Hubbard Hamiltonian. To elaborate, we consider for the moment only the free motion of the electrons and set $U = 0$ and neglect the Coulomb interaction. In this limit, we can Fourier transform the annihilation (creation) operators

$$c_{i\sigma} = \frac{1}{\sqrt{N}} \sum_{\boldsymbol{k}} e^{i\boldsymbol{k}\boldsymbol{R}_i} c_{\boldsymbol{k}\sigma}, \tag{4.2}$$

which reformulates the Hubbard Hamiltonian

$$H(U = 0) = \sum_{\boldsymbol{k},\sigma} \epsilon(\boldsymbol{k}) n_{\boldsymbol{k}\sigma} \text{ with } \epsilon(\boldsymbol{k}) = -t \sum_{\langle i0 \rangle} e^{i\boldsymbol{k}\boldsymbol{R}_i}, \tag{4.3}$$

where $n_{\boldsymbol{k}\sigma}$ is the occupation operator and $\langle i0 \rangle$ represents all neighbours of lattice site 0. For the two dimensional lattice we obtain the free dispersion $\epsilon(\boldsymbol{k}) = -2t(\cos(k_x) + \cos(k_y))$ and find a metallic solution for the Hubbard model. In the second case we consider the pure Coulomb interaction and set $t = 0$. The interaction part is already diagonal in real space and we derive two dispersionless Hubbard bands in the spectrum which are separated by the interaction strength U. At half-filling, the lower Hubbard band is completely filled whereas the upper Hubbard band is completely empty. This situation describes an insulator.

The interplay of the kinetic and the Coulomb term is responsible for the interesting many-body correlation physics which occurs in the two-dimensional Hubbard model.

4.1 Temperature and doping dependence of the Hubbard model

The Hubbard model exhibits a variety of correlation effects whose outcome enormously depends on doping and temperature. In the strong coupling regime which means, that the Coulomb interaction of the electrons is comparable or larger than their kinetic energy, and half-filling and sufficiently low temperature, the Hubbard model undergoes a metal-insulator transition. This transition is forced by the strong interaction of the electrons and constitutionally differs, therefore, from the metal-insulator transition known from band-insulators. By introducing additional charge carriers into the system, the insulating behaviour vanishes due to the possibility of the electrons to move through the system without generating additional double occupied lattice sites. This first example clarifies the drastic consequences of the strong interaction of the electrons. The classification of the different phases of the Hubbard model can be accomplished by the investigation of the one- and two-particle Green functions or their corresponding spectral functions. The following paragraph provides a short overview of the different regimes of the Hubbard model and gives a basis for the classification of the results of this thesis.

The single-band Hubbard model is assumed to describe the important properties of the high-temperature superconductors. Equivalent to the phase-diagram of the HTSCs (Fig. 4.2), the Hubbard model describes an effective antiferromagnetic (AF) ordered state close by half-filling which is driven by the interplay of the Coulomb interaction and the hybridisation. In particular, virtual hopping processes can reduce the free energy of the system but this assumes adjacent spins with opposite alignment due to the Pauli principle. The reader should note, that in the case of two dimensions and at finite temperature continuous symmetry breaking is prohibited by the Mermin-Wagner theorem [60]. Nevertheless, the magnetic correlation length can approach the system size at sufficiently low temperatures and the system appears to be in an effective AF ordered state. Hence, simulations close by half-filling seem to be performed in an AF ordered state although the continuous $SO(3)$ symmetry is not really broken. This advantage brings the simulation very close to an adequate description of the high-T_c materials. Another possibility which can cause an antiferromagnetic instability at half-filling is given by perfect nesting. Perfect nesting connects regions of the Brillouin zone which are parallel to each other by a commensurable wave vector $\boldsymbol{q} = (\pi/a, \pi/a)$. On the other hand, an AF ordered system can be described by two sub-lattices A and B which double the unit cell in real space and lead to a reduced magnetic Brillouin zone which realises the perfect nesting criteria.

Possible scattering processes with a momentum transfer of $\boldsymbol{q} = (\pi/a, \pi/a)$ obey the Bragg conditions and stabilise the state with reduced translational symmetry. The consequence is an insulating state which is justified by the nesting property and is distinguishable from the above described Mott-Hubbard transition.

Properties of the half-filled Hubbard model

In addition to the presence of two incoherent high energy bands, which result from the strong Coulomb interaction, one can observe low-energy excitations of the order of the exchange interaction J in the single-particle spectrum. The low energy excitations only occur at sufficiently low temperatures when the relevant spin degrees of freedom must be taken into account and the quantum nature of the spins become important. The narrow quasi-particle band can be nicely fitted by a tight-binding harmonics with dispersion of the form

$$E(\boldsymbol{k}) = 2cJ(\cos(k_x) + \cos(k_y))^2, \tag{4.4}$$

with the constant factor $c = 1/8$. A wide variety of several methods have reproduced the above dispersion relation for different models. The t-J model, which can be derived from the Hubbard model in the strong coupling limit, was investigated by the exact diagonalisation technique [61, 62, 63] and by the Green function quantum Monte Carlo method [64]. The Hubbard model also approved the above dispersion relation in exact diagonalisation studies [65] as well as in quantum Monte Carlo simulation [66]. The numerical results are also supported by analytical investigation such as the self-consistent Born approximation [67, 68, 69] or other variational calculations based on the 'string' picture or series expansion. All calculations confirm the picture of a single hole which is propagating in a Heisenberg antiferromagnet or half-filled Hubbard model. A visualisation of this scenario is possible within a string picture introduced by Bulaevskii, Nagaev, and Khomskii [70] and it is illustrated in Fig.4.4. The figure is taken from reference [71]. In the string picture, a hole is moving in an AF ordered background and creates a path of misaligned spins (grey shaded arrows in Fig. 4.4). The increase of the magnetic energy initiates an attractive potential which traps the hole around its starting point. A coherent motion of the hole becomes impossible and instead, the hole performs an incoherent oscillatory motion around the point where it was originally created. A coherent motion of the hole becomes only possible if the spin defects are healed up by spin-flip processes which restore the original AF ordered state. Thus, each spin-flip reduces the length of the string by two lattice spacings and shift the origin of the oscillatory motion to a second-nearest or third-nearest neighbour. Fig. 4.5 illustrates the different paths which are possible in order to reach a second-nearest (1,1) neighbour exist and a third-nearest-neighbour (2,0). Apparently, there exist two different paths to the (1,1) neighbour but only one path to the
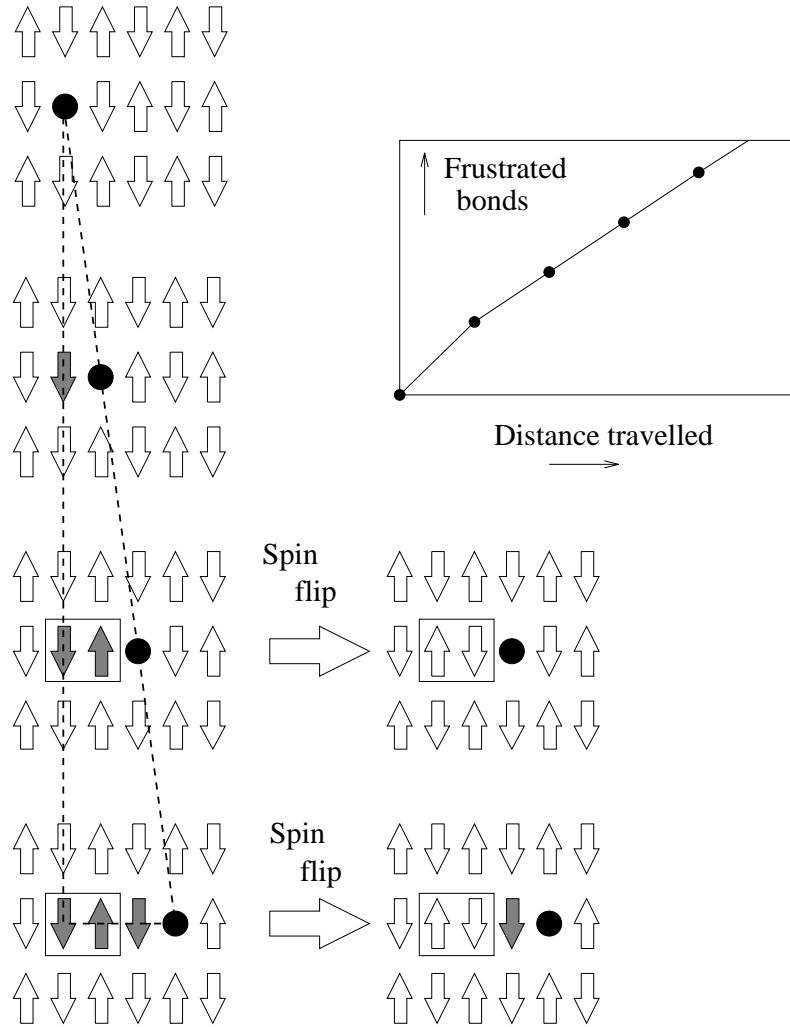
Figure 4.4 *Sketch of the motion of a single hole within an AF ordered background. The hopping of the hole leads to a trace of misaligned spins which results in an increase of the magnetic energy (top right) and, therefore, the motion of the hole is confined by an attractive potential. The only way to escape from this attractive potential is given by spin-flips which heal up the generated spin-defects. The figure is taken from [71].*
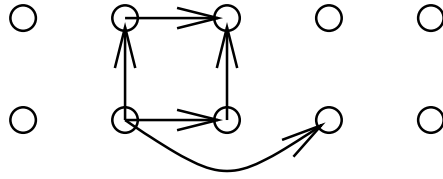
Figure 4.5 *Illustration of the different paths in order to reach a second-nearest neighbour (two possibilities) or to reach a third-nearest neighbour (one possibility).*

(2,0) neighbour. After these considerations, one immediately finds the dispersion of the above described hopping processes [71]:

$$
\begin{aligned}
cJ[2(\cos(2k_x) \quad &+ \quad \cos(2k_y)) + 2 \cdot 4\cos(k_x)\cos(k_y)] \\
&= \quad 4cJ[(\cos(2k_x) + \cos(2k_y))^2 - 1].
\end{aligned} \tag{4.5}
$$

With the exception of the prefactor c (which is numerically derived as $1/8$) the dispersion is entirely determined by the topology of the string. Obviously, the dispersion is degenerate for all momentum vectors which are lying on the surface of the magnetic Brillouin zone. However, numerical studies on the $t - J$ model show that the degeneracy is actually lifted. The observed energy difference is only small for $J/t \approx 0.4$ but becomes quite remarkable for larger ratios of J/t. A study of the parameter dependence shows that the dispersion along the line $(\pi/2, \pi/2)$ to $(\pi, 0)$ scales with the hopping integral t. This observation suggests an additional hopping process which involves the hopping amplitude t. In a simple picture, one can imagine the motion of a hole in the AF ordered background as a superposition of a rapidly oscillating particle (i.e. on a time scale $\propto t^{-1}$) and a slowly moving box (i.e. time scale $\propto J^{-1}$), which represents the string in Fig. 4.4. Therefore, the box represents the misaligned spins which form an attractive potential for the hole and might be viewed as a region of suppressed Néel order, such that the picture corresponds to the strong coupling limit of Schrieffer's spin-bag theory [72, 73]. Additionally, the superimposed motion of the hole and the box is sometimes referred to as a spin-polaron, where in an equivalent way an electron is moving in the presence of very strong electron-phonon coupling through a system which exhibits strong lattice distortions. Nevertheless, the string, spin-bag, and spin-polaron pictures describe the same situation: an oscillating hole is trapped in a region of reduced Néel order, with the consequence that the entire region has to move through the AF ordered background thereby enhancing the effective mass of the quasiparticle.

The correlation effects on energy scales J leave fingerprints in the one- and two-particle excitation spectra. At half-filling we find the following situation: additional to the incoherent Hubbard bands which result from the high energy Coulomb repulsion of the electrons, one can recognise the low energy excitations of the magnitude J close to the chemical potential. The low energy quasiparticle only occurs at sufficiently low temperatures if the spin degrees of freedom become important. Obviously, one can explain the origin of the

low-energy band by the above mentioned superposition of the motion of a hole in a reduced Néel ordered background. Further evidence for the spin-nature of the quasi-particle band is given by the dynamical spin-structure factor. The occurrence of the quasiparticle band in the one-particle spectrum is accompanied by the formation of a coherent spin-excitation around the wave-vector (π, π). The authors of Ref. [74] have fitted the collective spin mode in the spin-response function by a spin-wave dispersion:

$$E^{SW}(\boldsymbol{k}) = 2J\sqrt{1 - \frac{1}{4}(\cos(k_x) + \cos(k_y))^2}. \tag{4.6}$$

Even earlier studies have shown that two-particle correlation functions such as the spin-response function can be described in the framework of the SDW approximation for large values of the interaction U [73]. The spin response function shows a spin-wave dispersion $E^{SW}(\boldsymbol{k})$ with an energy scale of $2J$. The weight of the spin-response at $\boldsymbol{k} = (\pi, \pi)$ increases with decreasing temperature and becomes more and more sharp as it is predicted in the AF spin-wave theory.

Let us discuss the paramagnetic regime of the Hubbard model. This regime is mainly characterised by the interaction of itinerant electrons due to the strong Coulomb interaction. Spin-correlation effects, such as those described in the previous section, can be totally neglected because all relevant spin-degrees of freedom are thermally excited. Therefore, no sign of the energy scale J exists. The Green functions in the paramagnetic regime can be given in the Hubbard-I approximation:

$$G^{Hub-I}(\boldsymbol{k}, \omega) = \frac{1 - n/2}{\omega - \epsilon(\boldsymbol{k})(1 - n/2) + i\eta} + \frac{n/2}{\omega - U - \epsilon(\boldsymbol{k})n/2 + i\eta}, \tag{4.7}$$

which leads to the upper and lower band in the one-particle spectral function:

$$E_{\pm}^{Hub-I}(\boldsymbol{k}) = \frac{1}{2}\left(\epsilon(\boldsymbol{k}) + U \pm \sqrt{\epsilon(\boldsymbol{k})^2 + U^2}\right), \tag{4.8}$$

whereby n determines the filling of the system and $\epsilon(\boldsymbol{k}) = -2t(\cos(k_x) + \cos(k_y))$ denotes the tight-binding dispersion. The expression for the Green function in Eq. (4.7) becomes exact in the limits of $U = 0$ and $\epsilon(\boldsymbol{k}) = 0$.

The transition from the paramagnetic high-temperature regime to the AF ordered phase at half-filling is accompanied by an increase of the spin-correlation length. The reduction of the Brillouin zone initiates a fundamental change of the spectral function around the antiferromagnetic wave-vector $\boldsymbol{k} = (\pi, \pi)$ by backfolding of the spectral function $A(\boldsymbol{q}, \omega)$. In this intermediate regime, a drastic change in the dynamical correlation functions occurs. The transition from the SDW-like regime at half-filling to the Hubbard-I regime is accompanied by losing the low energy quasiparticle excitations. A similar change is visible in the two-particle spin-response spectrum. The coherent spin-wave washes out and gives way to a broad incoherent structure. This means, in other words, that the system loses all characteristics linked to a hole which is dressed by spin excitations and is moving in an AF ordered background.

Properties of the doped Hubbard model

As mentioned at the beginning of the section, the density of states of the strongly interacting Hubbard model splits into two distinguishable bands, i.e., a lower (valence) and upper (conductive) band at half-filling. The two-bands are separated by the Coulomb interaction U because the adding of further electrons inevitably leads to a double occupation causing an energy penalty U. If one inserts hole into the system, then the probability of double occupation decreases which leads to a reduction of spectral weight of the upper Hubbard band. These states are transferred close to the Fermi energy and contribute to the lower Hubbard band. Hence, the Hubbard model does not show a rigid band shift under doping but rather a shift of spectral weight from the upper to the lower Hubbard band [23]. The doping dependence of the single-particle function is depicted in Fig. 4.6 at an inverse temperature of $\beta t = 3$ and (a) at $\delta = 5$ % doping and (b) at $\delta = 20$ % doping. Regions with black or white colours correspond to spectral functions with high or low spectral weights respectively. These calculations are carried out at a relatively high temperature in order to reduce the notorious minus-sign problem. Nevertheless, this temperature should be low enough to observe possible magnetic correlation effects, since the magnetic exchange interaction is determined by the energy scale $J = 4t^2/U$ which has the value $0.5t$ for an interaction strength of $U = 8t$. In the under-doped regime, the single-particle spectral function clearly exhibits two incoherent Hubbard-bands and a coherent quasi-particle excitation with origins in the motion of a hole dressed by a cloud of spin-excitations. By increasing the doping, the chemical potential drops deeper into the lower Hubbard band in the region around (π, π). In this so-called 'optimal-doped' regime, the quasiparticle bands with energy scale J are still present. The quasi-particle band starts to vanish above optimal doping ($\langle n \rangle = 0.86$) and it becomes more visible when one reaches the over-doped regime with $\langle n \rangle = 0.80$. The fingerprints of the magnetic correlations are also visible in the

(a)

(b)
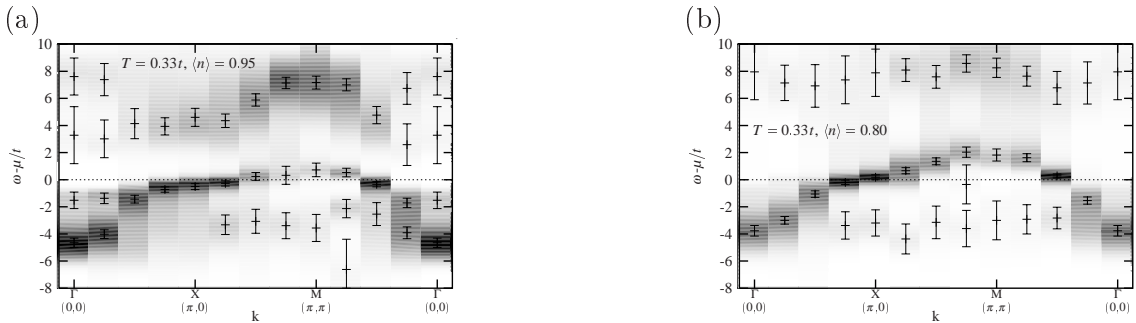
Figure 4.6 *Dynamical angle-resolved spectral function $A(\boldsymbol{k}, \omega)$ of the 8×8 Hubbard model at $\beta t = 3$ und $U = 8t$ for different fillings: (a) $\langle n \rangle = 0.95$ (under-doped), $\langle n \rangle = 0.80$ (over-doped). The results are extracted from [74].*
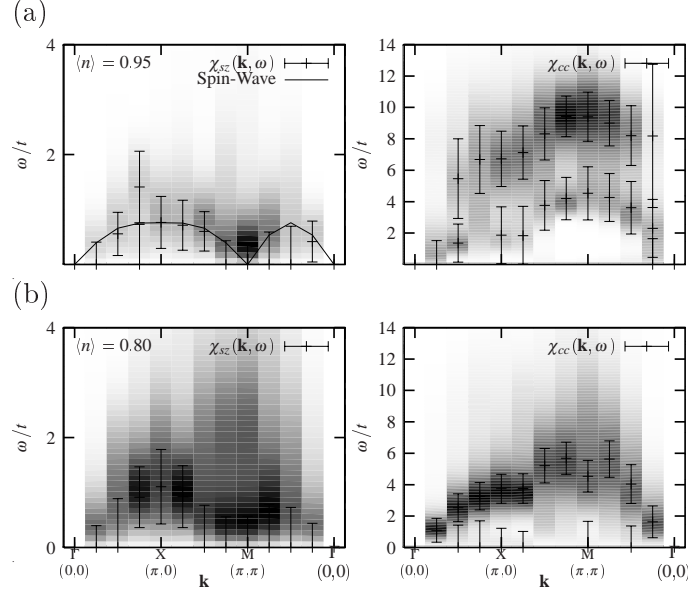
Figure 4.7 *Dynamical spin-, $\chi_{sz}(\boldsymbol{k},\omega)$, and charge-correlation functions, $\chi_{cc}(\boldsymbol{k},\omega)$, of the 8×8 Hubbard model at $\beta t = 3$ und $U = 8t$ for different fillings: (a) $\langle n \rangle = 0.95$ (under-doped), $\langle n \rangle = 0.80$ (over-doped). The results are extracted from [74].*

dynamical spin-correlation functions $\chi_{sz}(\boldsymbol{k},\omega)$ which are depicted in Fig. 4.7 (a) and (b) on the left hand site. In the underdoped and roughly optimal doped regime $\chi_{sz}(\boldsymbol{k},\omega)$ exhibits a well defined spin-wave around the antiferromagnetic wave vector $\boldsymbol{k} = (\pi,\pi)$ with the above mentioned spin-wave dispersion $E^{SW}(\boldsymbol{k},\omega) = 2J\sqrt{1 - \frac{1}{4}(\cos(k_x) + \cos(k_y))^2}$. The energy scale J can be read off at momentum vector $\boldsymbol{k} = (\pi,0)$ and has the value $2J$. The characteristics of the spin-response function drastically change if one dopes the system further. Above optimal doping, the spin-wave loses its sharp structure and the energy scale changes from $J = 4t^2/U$ to $E_{kin} \propto 8.0t$. Apparently, these changes come along with the loss of the quasiparticle features in the single-particle spectral function at the same doping. The charge response exhibits an overall broad structure with an energy scale of $E^{charge} \propto 12t$ which slightly reduces with increasing doping. These high energy structures mainly result from the strong Coulomb interaction and, in particular, no energy excitations of the scale $\propto J$ are visible. A more detailed investigation of the charge-response function is presented in [74].

At optimal doping and sufficiently low temperatures the Hubbard model exhibits a superconductive instability. It is assumed, that this instability is already pronounced by preformed cooper pairs above the actual critical temperature T_c in the pseudo-gap regime [75, 76]. The superconductors of the cuprates enormously differ from the conventional superconductors which can be described by the Bardeen-Cooper-Schrieffer (BCS) theory. In the BSC theory, the forming of cooper pairs can be traced back to a Fermi sur-

face instability. The exchange particles are phonons, the quanta of ionic vibrations of the crystal, which lead to an attractive potential between the electrons. The interaction of the cooper pairs exhibits an s-wave symmetry due to the local nature of the pairing interaction. Scattering processes between the electrons leads to a reduction of the potential energy and, hence, the electrons may occupy states above the Fermi sea which leads to an enhancement of the kinetic energy. This observation stands in contrast to the pairing mechanism in the high-temperature superconductors. The parent compounds of the high-temperature superconductors are antiferromagnetic ordered insulators which differ from a conventional Fermi-liquid description. On the other hand, the cuprates exhibit enormous high critical temperatures which suggests a totally different pairing mechanism in comparison to the conventional superconductors. This statement is also supported by the d-wave symmetry of the pairing interaction in the high-T_c materials.

In the forthcoming section, we investigate two-particle correlation functions in the framework of the Dynamical Cluster Approximation (DCA) with respect to the temperature and doping dependence. We try to figure out, if correlation effects of the energy scale J, which are presented in the previous section, are visible in the DCA two-particle correlation functions. Hereby, we can consider much lower temperatures because the DCA does not enormously suffer from the minus sign problem. Additionally, we are going to check if fingerprints of the two-particle correlations are also visible in the single-particle spectral function. The main part of the next section is extracted from [77].

In section 6, we incorporate the superconductive instability in the framework of the Dynamical Cluster approximation (DCA) and study the single-particle spectral function in detail. Our goals are the estimation of the superconducting transition temperature and the investigation of the evolution of the pseudo- and superconducting-gap.

Two-particle correlation functions within the DCA

5

Two-particle correlation functions, such as the dynamical spin- and charge correlation functions, determine a variety of crucial properties of many-body systems. Their poles as a function of frequency and momentum describe the elementary excitations, i.e., electron-hole excitations and collective modes, such as spin- and charge-density waves. Furthermore, an effective way to identify continuous phase transitions is to search for divergences of susceptibilities, i.e., two-particle correlation functions. Yet, compared to studies of single-particle Green functions and their spectral properties, where a good overall accord between theoretical models (Hubbard type-models) and experiment (ARPES) has been established (see [78, 66, 23, 79]), the situation is usually not so satisfying for two-particle Green functions. This is especially so for the case of correlated electron systems such as high-T_c superconductors (HTSC). The primary reason for this is that calculations of these Green functions are, from a numerical point of view, much more involved.

To expose the problem let us consider the spin-susceptibility which is given by:

$$\chi(\underline{q}) = \frac{1}{\beta L} \sum_{\underline{k},\underline{p}} \chi_{\underline{k},\underline{p}}(\underline{q}) \quad , \text{with} \tag{5.1}$$

$$\chi_{\underline{k},\underline{p}}(\underline{q}) = \langle c^\dagger_{\underline{k},\uparrow} c_{\underline{k}+\underline{q},\downarrow} c^\dagger_{\underline{p},\downarrow} c_{\underline{p}-\underline{q},\uparrow} \rangle$$

Here, L corresponds to the lattice size, β is the inverse temperature and $\underline{q} \equiv (\boldsymbol{q}, \Omega_m)$, $\boldsymbol{q}$ being the momentum and Ω_m a (bosonic) Matsubara frequency. To simplify the notation, we have adopted a path integral coherent state notation with Grassman variables:

$$c_{\underline{k},\sigma} \equiv c_{\boldsymbol{k},\omega_m,\sigma} = \frac{1}{\sqrt{\beta L}} \sum_{\boldsymbol{r}} \int_0^\beta \mathrm{d}\tau e^{i(\omega_m \tau - \boldsymbol{kr})} c_{\boldsymbol{r},\sigma}(\tau) \tag{5.2}$$

The two-particle irreducible vertex, $\Gamma_{\underline{k}',\underline{k}''}(\underline{q})$, is defined through the Bethe-Salpeter equation,

$$\chi_{\underline{k},\underline{p}}(\underline{q}) = \chi^0_{\underline{k},\underline{p}}(\underline{q}) + \sum_{\underline{k}',\underline{k}''} \chi^0_{\underline{k},\underline{k}'}(\underline{q}) \Gamma_{\underline{k}',\underline{k}''}(\underline{q}) \chi_{\underline{k}'',\underline{p}}(\underline{q}), \tag{5.3}$$
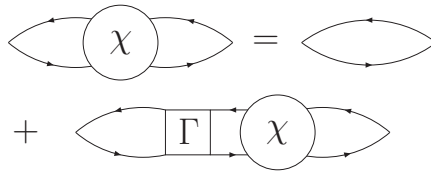
Figure 5.1 *Bethe-Salpeter equation for the two-particle propagator.*

which is diagrammatically depicted in Fig. (5.1).

Within the Dynamical Cluster Approximation (DCA) [7, 8], and see section 2.1, one can consistently define the two-particle Green functions, by extracting the irreducible vertex function from the cluster.

To define uniquely the DCA approximation, in particular in view of two-particle quantities, it is useful to start with the Luttinger-Ward functional Φ, which is computed using the DCA Laue function. Hence, Φ_{DCA} is a functional of a coarse-grained Green function, $\bar{G}(\boldsymbol{K}, i\omega_m) \equiv \bar{G}(\underline{K})$. Irreducible quantities such as the self-energy, and the two-particle irreducible vertex are calculated on the cluster and correspond, respectively, to the first- and second-order functional derivatives of Φ_{DCA} with respect to $\bar{G}$. Using the cluster irreducible self-energy, $\Sigma(\underline{K})$, and two-particle vertex, $\Gamma_{\underline{K}',\underline{K}''}(\underline{Q})$, one can then compute the lattice single-particle and lattice two-particle correlation functions using the Dyson and Bethe-Salpeter equations. This construction of two-particle quantities has the appealing property that they are thermodynamically consistent [6, 80]. Hence, the spin susceptibility, as calculated by using the particle-hole correlation functions, corresponds precisely to the derivative of the magnetisation with respect to an applied uniform static magnetic field. The technical aspects of the above program are readily carried out for single-particle properties. However a full calculation of the irreducible two-particle vertex -even within the DCA- is prohibitively expensive [81] and, thus, has never been carried out. In contrast to the calculation of single-particle quantities, the coarse-grained two-particle correlation function $\bar{\chi}_{\underline{K},\underline{K}'}(\underline{Q})$ is after completion of the self-consistence procedure not equal to the cluster two-particle correlation function $\chi_{c\underline{K},\underline{K}'}(\underline{Q})$ because the self-consistency is only made on the single-particle level. The following considerations will show, that the susceptibility can be calculated within the DCA approximation, where the irreducible two-particle vertex Γ is substituted by the corresponding cluster vertex Γ_c, which leads to an inversion of the cluster two-particle Bethe-Salpeter equation.

For the moment, we consider the bare and interacting cluster susceptibilities as well as the irreducible cluster vertex function: $\chi^0_{c\underline{K},\underline{K}'}(\underline{Q})$, $\chi_{c\underline{K},\underline{K}'}(\underline{Q})$ and $\Gamma_{c\underline{K},\underline{K}'}(\underline{Q})$. These quantities are evaluated at cluster momentum vectors and they are correlated by the cluster Bethe-

Salpeter equation,

$$\chi_{c\underline{K},\underline{P}}(\underline{Q}) = \chi^0_{c\underline{K},\underline{P}}(\underline{Q}) + \sum_{\underline{K'},\underline{K''}} \chi^0_{c\underline{K},\underline{K'}}(\underline{Q})\Gamma_{c\underline{K'},\underline{K''}}(\underline{Q})\chi_{c\underline{K''},\underline{P}}(\underline{Q}), \tag{5.4}$$

where the inversion may be written in a short notation:

$$\Gamma_c(\underline{Q}) = [\chi^0_c(\underline{Q})]^{-1} - [\chi_c(\underline{Q})]^{-1}. \tag{5.5}$$

Each quantity in Eq. (5.5) represent a matrix with row and column indices $\underline{K}$ and $\underline{K'}$. The non-interacting two-particle Green function $\chi^0_c(\underline{Q})$ is constructed from a pair of fully dressed single-particle Green functions and it is diagonal in the spin, momentum and frequency labels:

$$\begin{aligned}\chi^0_c(\underline{Q}) &= \chi^0_{c\underline{K},\underline{K'}}(\underline{Q}) \\ &= N_c\delta_{\sigma\sigma'}\delta_{mm'}\delta_{\boldsymbol{KK'}}G^\sigma_c(\boldsymbol{K},i\omega_m)G^{\sigma'}_c(\boldsymbol{K}+\boldsymbol{Q},i\omega_m+i\nu).\end{aligned} \tag{5.6}$$

The convolution of the cluster Green function G^c will be calculated after the actual quantum Monte Carlo run, whereas the decomposition of the interacting cluster two-particle Green function has to be performed for each Hubbard-Stratonovich configuration within the Monte Carlo run separately.

In comparison with the single-particle quantities, the coarse-grained two-particle Green function $\bar{\chi}$ can be defined in a similar way. The lattice vectors $\boldsymbol{k}$, $\boldsymbol{k'}$ and $\boldsymbol{q}$ are decomposed into inter- and intra-cluster momentum vectors: $\boldsymbol{k} = \boldsymbol{K} + \tilde{\boldsymbol{k}}$, $\boldsymbol{k'} = \boldsymbol{K'} + \tilde{\boldsymbol{k}}'$ and $\boldsymbol{q} = \boldsymbol{Q} + \tilde{\boldsymbol{q}}$ (compare with section 2.1). $\bar{\chi}$ may be written as follows:

$$\bar{\chi}(\boldsymbol{Q}+\tilde{\boldsymbol{q}},i\nu) = \frac{N_c^2}{N^2}\sum_{\tilde{\boldsymbol{k}},\tilde{\boldsymbol{k}}'}\chi_{\boldsymbol{K}+\tilde{\boldsymbol{k}},i\omega_m;\boldsymbol{K'}+\tilde{\boldsymbol{k}}',i\omega_{m'}}(\boldsymbol{Q}+\tilde{\boldsymbol{q}},i\nu). \tag{5.7}$$

The definition of the non-interacting coarse-grained two-particle Green function is similar to the corresponding cluster quantity. $\bar{\chi}^0(\boldsymbol{Q}+\tilde{\boldsymbol{q}},i\nu)$ is diagonal in the spin, momentum and frequency labels:

$$\begin{aligned}\bar{\chi}^0(\boldsymbol{Q}+\tilde{\boldsymbol{q}},i\nu) &= N_c\delta_{\sigma\sigma'}\delta_{\boldsymbol{KK'}}\delta_{mm'}\left[\frac{N_c}{N}\sum_{\tilde{\boldsymbol{k}}}G^\sigma(\boldsymbol{K}+\tilde{\boldsymbol{k}},i\omega_m)\right. \\ &\quad \left.\times G^{\sigma'}(\boldsymbol{K}+\tilde{\boldsymbol{k}}+\boldsymbol{Q}+\tilde{\boldsymbol{q}},i\omega_m+i\nu)\right].\end{aligned} \tag{5.8}$$

The DCA approximation is applied to Eq.(5.3) by replacing the irreducible vertex function Γ by the irreducible cluster vertex function Γ_c. The reader should take into account, that χ and χ_0 on the RHS of Eq. (5.3) share no common momentum labels and, hence, one can freely sum over the momenta $\tilde{\boldsymbol{k}}$, which gives the following identity:

$$\bar{\chi}_{\underline{K},\underline{P}}(\underline{q}) \cong \bar{\chi}^0_{\underline{K},\underline{P}}(\underline{q}) + \sum_{\underline{K'},\underline{K''}} \bar{\chi}^0_{\underline{K},\underline{K'}}(\underline{q})\Gamma_{c\underline{K'},\underline{K''}}(\underline{Q})\bar{\chi}_{\underline{K''},\underline{P}}(\underline{q}), \tag{5.9}$$

which can be written in a short notation:

$$\Gamma_c(\underline{Q}) = [\bar{\chi}^0(\underline{q})]^{-1} - [\bar{\chi}(\underline{q})]^{-1}. \tag{5.10}$$

At this point, we can combine Eq. (5.5) and Eq. (5.10) and get the result:

$$\bar{\chi}^{-1}(\underline{q}) = \chi_c^{-1}(\underline{Q}) - \chi_c^{0-1}(\underline{Q}) + \bar{\chi}^0(\underline{q}). \tag{5.11}$$

The charge (ch) and spin (sp) susceptibilities $\chi_{ch,sp}$ are deduced from $\bar{\chi}$ [81]:

$$\chi_{ch,sp}(q,T) = \frac{(k_B T)^2}{N_c^2} \sum_{\underline{K}\underline{K}'\sigma\sigma'} \lambda_{\sigma\sigma'} \bar{\chi}_{\sigma,\sigma',\underline{K},\underline{K}'}(q), \tag{5.12}$$

where $\lambda_{\sigma\sigma'} = 1$ for the charge channel and $\lambda_{\sigma\sigma'} = \sigma\sigma'$ for the spin channel. The complexity of this approach lies in the inversion of the Bethe-Salpeter equation (5.5), since the irreducible vertex consists of three momentum and three frequency indices.

In the present work, we would like to overcome this situation by suggesting a scheme where the $\underline{K}'$ and $\underline{K}''$ dependencies of the irreducible vertex are neglected. At low temperatures, this amounts to the assumption that in an energy and momentum window around the Fermi surface, the irreducible vertex depends weakly on $\underline{K}'$ and $\underline{K}''$. Following this assumption, an effective two-particle vertex in terms of an average over the $\underline{K}'$ and $\underline{K}''$ dependencies of $\Gamma_{c\underline{K}',\underline{K}''}(\underline{Q})$ is introduced:

$$\frac{1}{\beta L} U_{eff}(\underline{Q}) = \langle \Gamma_{c\underline{K}',\underline{K}''}(\underline{Q}) \rangle. \tag{5.13}$$

As shown in an earlier Quantum Monte Carlo (QMC) study by Bulut et al. [82] for a single QMC cluster, this is reasonable for the 2D Hubbard model (on this QMC cluster of size 8×8 with $U = 8t$). The authors of [82] investigate the question of whether the correlations between electrons can be described by an effective interaction which only takes single longitudinal and transverse spin fluctuations into account or whether the effect of higher-order multi-spin fluctuations may not be neglected. Bulut et al. calculated with $U_{eff}(\underline{Q})$ the effective irreducible electron-hole vertex and compared the results with calculations where the irreducible electron-hole vertex was estimated via the Monte Carlo technique on a 8×8 single QMC cluster and via a third-order perturbation theory approach. Both the momentum and frequency dependence were in rather good agreement with the QMC and perturbation theory results for the effective electron-hole interaction.

By replacing the irreducible vertex by $\frac{1}{\beta L} U_{eff}(\underline{Q})$ in the cluster version of the Bethe-Salpeter Eq. (5.3) and carrying out the summations to obtain the cluster susceptibility gives:

$$U_{eff}(\underline{Q}) = \frac{1}{\bar{\chi}_0(\underline{Q})} - \frac{1}{\chi(\underline{Q})}, \tag{5.14}$$

where χ corresponds to the fully interacting spin/charge susceptibility on the DCA cluster in the particle-hole channel and $\bar{\chi}_0$ can be derived from the free cluster spin/charge correlation function. Hereby, we consider the free expectation value to which purpose we can apply Wick's theorem. The free cluster spin susceptibility $\bar{\chi}_0(\boldsymbol{Q}, i\omega_m)$ [1] reads with $S(\boldsymbol{Q}) = \frac{1}{\sqrt{N_c}} \sum_{\boldsymbol{j}} e^{i\boldsymbol{Q}\boldsymbol{j}} (n_{\boldsymbol{j},\uparrow} - n_{\boldsymbol{j},\downarrow})$ in the paramagnetic case [2]:

$$
\begin{aligned}
\bar{\chi}_0(\boldsymbol{Q}, i\Omega_m) &= \int d\tau \, e^{i\Omega_m \tau} \langle S^z(\boldsymbol{Q}, \tau) \, S^z(-\boldsymbol{Q}, 0) \rangle_0 &&(5.15) \\
&= \frac{1}{N_c} \sum_{\boldsymbol{j},\boldsymbol{j}'} \int d\tau \, e^{i\Omega_m \tau} \, e^{i(\boldsymbol{j}-\boldsymbol{j}')Q} \\
&\quad \sum_{\sigma,\sigma'} \sigma\sigma' \langle c^\dagger_{\boldsymbol{j},\sigma}(\tau) \, c_{\boldsymbol{j}',\sigma'}(0) \rangle \langle c_{\boldsymbol{j},\sigma}(\tau) \, c^\dagger_{\boldsymbol{j}',\sigma'}(0) \rangle \\
&= -\frac{1}{N_c} \sum_{\substack{\sigma \\ \boldsymbol{K},\boldsymbol{K}'}} \int d\tau \, e^{i\Omega_m \tau} \, \delta(\boldsymbol{Q} - \boldsymbol{K} + \boldsymbol{K}') \, G^\sigma_{c\boldsymbol{K}}(\tau, 0) \, G^\sigma_{c\boldsymbol{K}'}(0, \tau) \\
&= -\frac{1}{N_c} \sum_{\boldsymbol{K},\sigma} \int d\tau \, e^{i\Omega_m \tau} \, G^\sigma_{c\boldsymbol{K}}(\tau, 0) \, G^\sigma_{c\boldsymbol{K}-\boldsymbol{Q}}(0, \tau) \\
&= -\frac{1}{N_c} \frac{1}{\beta^2} \sum_{\substack{\boldsymbol{K},\sigma \\ i\omega_m, i\omega_{m'}}} \int d\tau \, e^{i(\Omega_m - \omega_m + \omega_{m'})\tau} \, G^\sigma_c(\boldsymbol{K}, i\omega_m) \, G^\sigma_c(\boldsymbol{K}-\boldsymbol{Q}, i\omega_{m'}) \\
&= -\frac{1}{N_c} \frac{1}{\beta} \sum_{\substack{\boldsymbol{K},\sigma \\ i\omega_m, i\omega_{m'}}} \delta(i\omega_{m'} - (i\omega_m - i\Omega_m)) \, G^\sigma_c(\boldsymbol{K}, i\omega_m) \, G^\sigma_c(\boldsymbol{K}-\boldsymbol{Q}, i\omega_{m'}) \\
&= -\frac{1}{N_c} \frac{1}{\beta} \sum_{\substack{\boldsymbol{K},\sigma \\ i\omega_m}} G^\sigma_c(\boldsymbol{K}, i\omega_m) \, G^\sigma_c(\boldsymbol{K}-\boldsymbol{Q}, i\omega_m - i\Omega_m) \\
&= -\frac{1}{N_c} \frac{1}{\beta} \sum_{\substack{\boldsymbol{K},\sigma \\ i\omega_m}} G^\sigma_c(\boldsymbol{K}+\boldsymbol{Q}, i\omega_m + i\Omega_m) \, G^\sigma_c(\boldsymbol{K}, i\omega_m) &&(5.16)
\end{aligned}
$$

The calculation of the bubble is accompanied by the following transformations:

$$
-\left\langle c_{\boldsymbol{j},\sigma}(\tau) \, c^\dagger_{\boldsymbol{j}',\sigma}(0) \right\rangle = G^\sigma(\boldsymbol{j}, \tau, \boldsymbol{j}', 0) = \frac{1}{N_c} \sum_{\boldsymbol{k}} e^{-i(\boldsymbol{j}-\boldsymbol{j}')\boldsymbol{k}} \, G^\sigma_{\boldsymbol{k}}(\tau, 0) \tag{5.17}
$$

with

$$
G_{\boldsymbol{k}}(\tau, 0) = \frac{1}{\beta} \sum_{i\omega_m} e^{-i\omega_m \tau} \, G(\boldsymbol{k}, i\omega_m) \tag{5.18}
$$

and

$$
G_{\boldsymbol{k}}(0, \tau) = \frac{1}{\beta} \sum_{i\omega_m} e^{i\omega_m \tau} \, G(\boldsymbol{k}, i\omega_m). \tag{5.19}
$$

----

[1] By taking $N(\boldsymbol{Q}) = \frac{1}{\sqrt{N_c}} \sum_{\boldsymbol{j}} e^{i\boldsymbol{Q}\boldsymbol{j}} (n_{\boldsymbol{j},\uparrow} + n_{\boldsymbol{j},\downarrow})$, a similar calculation yields the same result for the free cluster charge susceptibility. The static term $\sum_{\sigma,\sigma'} \langle c^\dagger_{\boldsymbol{j},\sigma}(\tau) \, c_{\boldsymbol{j},\sigma}(\tau) \rangle \langle c^\dagger_{\boldsymbol{j}',\sigma'}(0) \, c_{\boldsymbol{j}',\sigma'}(0) \rangle$ has to be subtracted from the RHS of Eq. (5.15) due to the *Kubo formula*.

[2] In the paramagnetic case is $\sum_{\sigma,\sigma'} \sigma\sigma' \langle c^\dagger_{\boldsymbol{j},\sigma}(\tau) \, c_{\boldsymbol{j},\sigma}(\tau) \rangle \langle c^\dagger_{\boldsymbol{j}',\sigma'}(0) \, c_{\boldsymbol{j}',\sigma'}(0) \rangle = 0$.
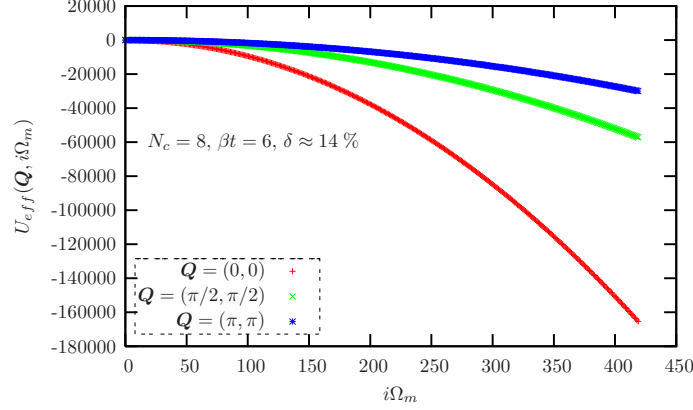
Figure 5.2   *Effective two-particle vertex $U_{eff}(\mathbf{Q}, i\Omega_m)$ as a function of the bosonic Matsubara frequency $i\Omega_m$ for a typical parameter set: $\beta t = 6$ at $\delta \approx 14$ % on the $N_c = 8$ cluster at different cluster momentum vectors*

In Eq. (5.16) we recognise that $\bar{\chi}_0$ is constructed from a pair of fully dressed single-particle Green functions. In order to incorporate the correct high frequency behaviour of the Green functions in Eq. (5.16), one has to perform the summation over Matsubara frequencies from minus infinity to plus infinity. This summation is performed in two steps. In a frequency window of 500 Matsubara frequencies around $i\omega_m = 0$, the Green functions in Eq. (5.16) were taken from the Monte Carlo calculation. The remaining summation is performed in an analytical way. Therefore, we consider the high energy behaviour of the Green functions: $\lim_{i\omega_m \to \infty} G(i\omega_m) \propto \frac{1}{i\omega_m}$ and transform the summation in Eq. (5.16) into an integral expression. The analytical treatment of the convolution is carried out from a given fermionic Matsubara frequency $z = i\omega_m$. Hence, we obtain with the bosonic Matsubara frequency $a = i\Omega_m$ the following relations:

$$\int_z^{+\infty} \mathrm{d}z' \frac{1}{z' + a} \frac{1}{z'} = \frac{1}{a} \log \frac{z + a}{z} \tag{5.20}$$

$$\int_{-\infty}^{-z} \mathrm{d}z' \frac{1}{z' + a} \frac{1}{z'} = \frac{1}{a} \log \frac{z}{z - a}, \tag{5.21}$$

and for the case $a = 0$:

$$\int_z^{+\infty} \mathrm{d}z' \frac{1}{z'^2} = \int_{-\infty}^{-z} \mathrm{d}z' \frac{1}{z'^2} = \frac{1}{z}. \tag{5.22}$$

We have explicitly checked, that the high frequency behaviour of the bubble is given by $\propto \frac{1}{(i\omega_m)^2}$. The interacting susceptibility χ obeys the same high frequency behaviour as the non-interacting susceptibility but with a different proportionality factor. From this it follows that the effective interaction U_{eff} is also given by $\propto \frac{1}{(i\omega_m)^2}$ in the large frequency limit. The situation is depicted in Fig. 5.2, where we use a typical parameter set. The effective particle-hole vertex is shown for different cluster momentum vectors and,

obviously, the contributions of U_{eff} become more important with the increasing value of Matsubara frequency. The reader should note, that a simple Fourier transformation of U_{eff} from Matsubara frequencies to the imaginary time axis would cause incorrect results. We have seen, that the bubble can be constructed from the coarse-grained Green function, where we implicitly incorporate the equivalence of the spin up and spin down Green functions in the paramagnetic case. In the case of the interacting susceptibility, the decomposition of the two-particle correlation function has to be performed for each Hubbard-Stratonovich configuration within the Monte Carlo procedure. Hereby, the equivalence of the spin up and spin down Green functions is not longer guaranteed, which yields additional terms in the calculation of the susceptibility:

$$\chi(\boldsymbol{Q}, i\Omega_m) \;\; = \;\; \int d\tau \, e^{i\Omega_m \tau} \begin{cases} \langle S^z(\boldsymbol{Q}, \tau) \, S^z(-\boldsymbol{Q}, 0) \rangle, & \text{spin} \\ \langle N(\boldsymbol{Q}, \tau) \, N(-\boldsymbol{Q}, 0) \rangle, & \text{charge,} \end{cases} \tag{5.23}$$

with

$$\begin{aligned} \langle S^z(\boldsymbol{Q}, \tau) \, S^z(-\boldsymbol{Q}, 0) \rangle_{\boldsymbol{s}} \;\; = \;\; & \sum_{\boldsymbol{j}, \boldsymbol{j}'} \sum_{\sigma, \sigma'} e^{i(\boldsymbol{j}-\boldsymbol{j}')Q} \, \sigma\sigma' \Big\{ \langle c^\dagger_{\boldsymbol{j},\sigma}(\tau) \, c_{\boldsymbol{j},\sigma}(\tau) \rangle_{\boldsymbol{s}} \langle c^\dagger_{\boldsymbol{j}',\sigma'}(0) \, c_{\boldsymbol{j}',\sigma'}(0) \rangle_{\boldsymbol{s}} \\ & + \langle c^\dagger_{\boldsymbol{j},\sigma}(\tau) \, c_{\boldsymbol{j}',\sigma'}(0) \rangle_{\boldsymbol{s}} \langle c_{\boldsymbol{j},\sigma}(\tau) \, c^\dagger_{\boldsymbol{j}',\sigma'}(0) \rangle_{\boldsymbol{s}} \Big\}, \end{aligned}$$

and

$$\begin{aligned} \langle N^z(\boldsymbol{Q}, \tau) \, N^z(-\boldsymbol{Q}, 0) \rangle_{\boldsymbol{s}} \;\; = \;\; & \sum_{\boldsymbol{j}, \boldsymbol{j}'} \sum_{\sigma, \sigma'} e^{i(\boldsymbol{j}-\boldsymbol{j}')Q} \Big\{ \langle c^\dagger_{\boldsymbol{j},\sigma}(\tau) \, c_{\boldsymbol{j},\sigma}(\tau) \rangle_{\boldsymbol{s}} \langle c^\dagger_{\boldsymbol{j}',\sigma'}(0) \, c_{\boldsymbol{j}',\sigma'}(0) \rangle_{\boldsymbol{s}} \\ & + \langle c^\dagger_{\boldsymbol{j},\sigma}(\tau) \, c_{\boldsymbol{j}',\sigma'}(0) \rangle_{\boldsymbol{s}} \langle c_{\boldsymbol{j},\sigma}(\tau) \, c^\dagger_{\boldsymbol{j}',\sigma'}(0) \rangle_{\boldsymbol{s}} \Big\}, \end{aligned}$$

where $\langle \cdots \rangle_{\boldsymbol{s}}$ denotes the expectation value for a given Hubbard Stratonovich configuration $\boldsymbol{s}$. Finally, the combination of the effective two-particle vertex U_{eff} and the bubble $\chi_0(\underline{q})$ of the dressed lattice Green functions $G(\underline{k})$ results in our estimate of the lattice susceptibility:

$$\chi(\underline{q}) = \frac{\chi_0(\underline{q})}{1 - U_{eff}(\underline{Q}) \cdot \chi_0(\underline{q})}. \tag{5.24}$$

The bubble of the lattice $\chi_0(\underline{q})$ is given by Eq. (5.16), whereas the cluster Green functions have to be replaced by the lattice Green functions which are determined by the Dyson equation: $G(\underline{k}) = \frac{1}{G_0^{-1}(\underline{k}) - \Sigma(\underline{K})}$. The self-energy is self-consistently calculated for all cluster momentum vectors $\boldsymbol{K}$ in the DCA loop (see section. 2.4). Hereby, we exploit the weak momentum dependence of the self-energy. The real- and imaginary parts are depicted in Fig. 5.3 at the first Matsubara frequency and for different fillings. The momentum dependence rapidly becomes weaker if the system is doped away from half-filling.

(a)

(b)
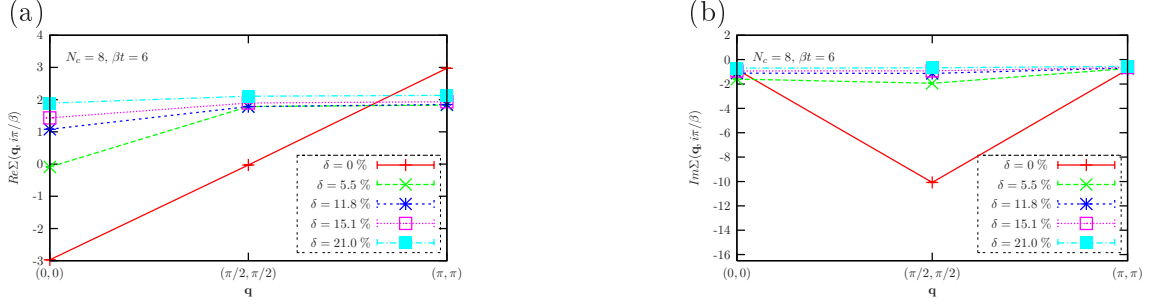
Figure 5.3 *Real- and imaginary part of the self-energy for different fillings at inverse temperature $\beta t = 6$ and $U = 8t$ on the $N_c = 8$ cluster.*

In order to cross check our results, we slightly modify Eq. 5.24 to:

$$\chi(\underline{q}) = \frac{\chi_0(\underline{q})}{1 - \alpha \cdot U_{eff}(\underline{q}) \cdot \chi_0(\underline{q})}. \tag{5.25}$$

Here, we have introduced an additional "controlling" parameter α in the susceptibility denominator, which is calculated in a self-consistent manner. It assures, for example in the case of the longitudinal spin response, that $\chi(\underline{q})$ obeys the following sum rule (a similar idea, to use sum rules for constructing a controlled local approximation for the irreducible two-particle vertex has been implemented by Vilk and Tremblay [83]):

$$\frac{1}{\beta L} \sum_{\underline{q}} \chi(\underline{q}) = \langle (S_i^z)^2 \rangle. \tag{5.26}$$

Of course, α should be as close as possible to $\alpha = 1$, which is indeed what we will find after implementing the sum rule (see below). At this point, it should be mentioned, that our sum rule in Eq. (5.26) or our approach to two-particle correlation functions is much more sophisticated than the approximation for the two-particle vertex, which was formulated by Vilk and Tremblay [84]. In their two-particle self-consistent approximation (TPSC), the spin χ_{spin} and charge susceptibilities χ_{charge} are approximated by an RPA-like form with two different interactions U_{spin} and U_{charge}. The estimation of the interactions is performed in a self-consistent manner and, therefore, the TPSC notably differs from the standard RPA-approach. The necessity to distinguish between two different effective interactions for spin and charge is dictated by the Pauli exclusion principle. It implies that both χ_{spin} and χ_{charge} are related to only one local pair correlation function $\langle n_\uparrow n_\downarrow \rangle$ [85]. The huge difference between our approach to two-particle correlation functions (see Eq. 5.25) and the TPSC is, that we regard the total frequency dependence of the effective interactions and, hence, take retardation effects into account.

Our implementation of the DCA for the Hubbard model is standard. The reader should consult section 2.1 or Ref. [8] for a summary. At this point, we will only discuss our
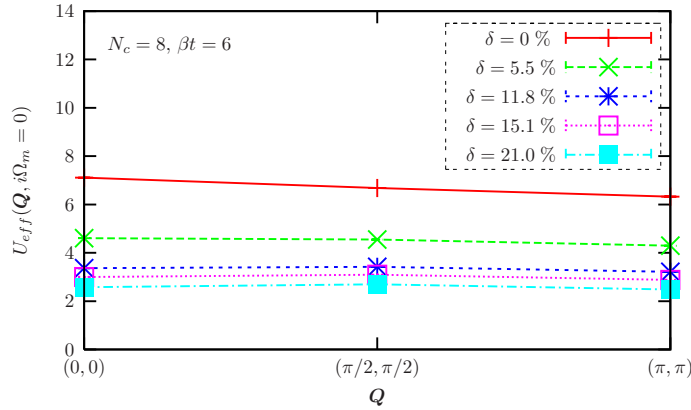
Figure 5.4 *Static ($i\Omega_m = 0$) irreducible particle-hole interaction U_{eff} in the spin channel for different cluster momentum vectors and dopings at inverse temperature $\beta t = 6$ and $U = 8t$.*

interpolation scheme as well as the implementation of a SU(2)-spin symmetry broken algorithm. Since the DCA evaluates the irreducible quantities, $\Sigma(\underline{K})$ as well as $U_{eff}(\underline{Q})$ for the cluster wave vectors, an interpolation scheme has to be used. To achieve this, we adopt the following strategy: for a fixed Matsubara frequency $i\Omega_m$ and for each cluster vector $\boldsymbol{Q}$, the effective interaction U_{eff} is rewritten as a series expansion:

$$U_{eff}(\boldsymbol{Q}, i\Omega_m) = \sum_i \sum_{\Delta_i} e^{i\Delta_i \boldsymbol{Q}} A_i(i\Omega_m), \tag{5.27}$$

with $i = 0, ..., N_c - 1$, where N_c is the number of the cluster momentum vectors $\boldsymbol{Q}$. The quantity Δ_i represents vectors, where each vector from the corresponding Δ_i belongs to the same "shell" around the origin $(0,0)$ in real space, i.e.

$$\Delta_0 = \begin{pmatrix} 0 \\ 0 \end{pmatrix}; \ \Delta_1 = \pm \begin{pmatrix} 1 \\ 0 \end{pmatrix}, \pm \begin{pmatrix} 0 \\ 1 \end{pmatrix}$$

$$\Delta_2 = \begin{pmatrix} \pm 1 \\ \pm 1 \end{pmatrix}, \begin{pmatrix} \mp 1 \\ \pm 1 \end{pmatrix}; \ \Delta_3 = \pm \begin{pmatrix} 2 \\ 0 \end{pmatrix}, \pm \begin{pmatrix} 0 \\ 2 \end{pmatrix} ... . \tag{5.28}$$

With a given U_{eff}, Eq. (5.27) can be inverted to uniquely determine A_i. With these coefficients, one can compute the effective particle-hole interaction for every lattice momentum vector $\boldsymbol{q}$. This interpolation method works well when U_{eff} is localised in real space and the sum in Eq. (5.27) can be cut-off at a given shell.

The effective particle-hole interaction U_{eff} in the spin channel is shown in Fig. 5.4 for a variety of dopings at inverse temperature $\beta t = 6$, $U/t = 8$ and on an $N_c = 8$ cluster, which corresponds to the so-called "8A" Betts cluster (see [10, 11]). The U_{eff}-function displays
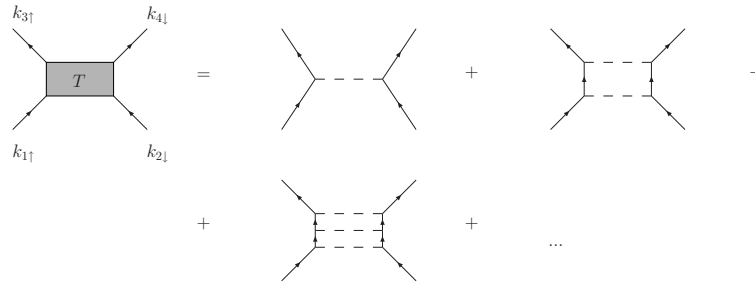
Figure 5.5 *Multi-scattering processes of two electrons. Kanamori screening leads to a renormalisation of the interaction strength brought by T-matrix effects.*

a smooth momentum dependence. These observations further support the interpolation scheme in (Eq. (5.27)). Thus, indeed, U_{eff} is rather localised in real space with sizable reduction from its bare $U = 8t$ value for larger doping and a further slight reduction at $q = (\pi, \pi)$. The reduction is partly due to the self-energy effects in the single-particle propagator, which reduce $\bar{\chi}_0$ from its non-interacting ($U = 0$) value $\chi^{(0)}$. Partly, it also reflects both the Kanamori (see [52]) repeated particle-particle scattering and vertex corrections. The repeating scattering processes of two electrons with spin k_1 and k_2 are depicted in Fig. 5.5. Hereby, Kanamori completely neglects the generation of electron-hole excitations out of the Fermi sea and assumes, that the scattering processes in Fig. 5.5 are the dominant ones whereby all other electron-electron interactions are negligible. By omitting vertex corrections, the T-matrix takes the form of a geometric series. The approximation works well in the dilute limit, i.e., in the case of an almost filled or empty band. In systems with a large value of the Coulomb interaction, the screened interaction is reduced to $\tilde{U} \simeq \frac{U}{1+U/W} \simeq W$.

The static irreducible particle-hole interaction U_{eff} in the spin channel is depicted in Fig. 5.6 for different cluster momentum vectors and cluster sizes at $\delta \approx 14\,\%$ doping. Only marginal differences are visible between the different cluster types. The reader should note, that the cluster momentum vector $\boldsymbol{k} = (\pi/2, \pi, 2)$ is not present on the $N_c = 4$ cluster.

Summarising, the new approach to two-particle properties relies on two approximations which render the calculation of the corresponding Green function possible. Firstly, the effective particle-hole interaction $U_{eff}(\underline{Q})$ depends only on the center-of-mass momentum and frequency, i.e. $\boldsymbol{Q}$ and $i\Omega_m$. Secondly, $\chi(\underline{Q})$, is directly extracted from the cluster and $\bar{\chi}_0(\underline{Q})$ is obtained from the bubble of the coarse-grained Green functions.

To generate DCA results for the Néel temperature, we have used an SU(2) symmetry broken code. The setup is illustrated in Fig. 2.5. We introduce a doubling of the unit cell — to accommodate AF ordering — which in turn defines the magnetic Brillouin zone. The unit cell is characterised by a c- and d-orbital. The DCA k-space patching is carried out in the magnetic Brillouin zone and the Dyson equation for the single-particle propagator

is given as a matrix equation:

$$G^\sigma(\underline{k}) = \frac{1}{G_0^{-1}(\underline{k}) - \Sigma^\sigma(\underline{K})}, \tag{5.29}$$

with

$$G^\sigma(\underline{k}) = \begin{pmatrix} G_{cc}^\sigma(\underline{k}) & G_{cd}^\sigma(\underline{k}) \\ G_{dc}^\sigma(\underline{k}) & G_{dd}^\sigma(\underline{k}) \end{pmatrix}. \tag{5.30}$$

The Green functions with spin σ are defined by

$$G_{\alpha\alpha'}^\sigma(\underline{k}) = -\int_0^\beta \mathrm{d}\tau e^{i\omega_m\tau} \langle T_\tau \{c_{\alpha,\sigma}(k,\tau)c_{\alpha',\sigma}^\dagger(k,0)\}\rangle \tag{5.31}$$

and α, α' indicate the c- and d-orbitals. With the SU(2) symmetry broken algorithm, one can compute directly the staggered magnetisation, i.e., $m = \frac{1}{L}\sum_{\boldsymbol{j}} e^{i\boldsymbol{Qj}}(n_{\boldsymbol{j},\uparrow} - n_{\boldsymbol{j},\downarrow})$, and thereby determine the transition temperature. Since the DCA is a conserving approximation, the so determined transition temperature corresponds precisely to the temperature scale at which the corresponding susceptibility, calculated without any approximations on the irreducible vertex $\Gamma_{\underline{K'},\underline{K''}}(\boldsymbol{Q})$, diverges.

5.1 AF phase transition

A first test of the validity of our new approach is a comparison with the SU(2) symmetry broken DCA calculation on an $N_c = 8$ cluster at $U = 8t$. The idea is to extract the Néel temperature T_N from a divergence in the spin susceptibility as calculated in the above described (paramagnetic) scheme — see Eq. 5.25 — and to compare it to the DCA
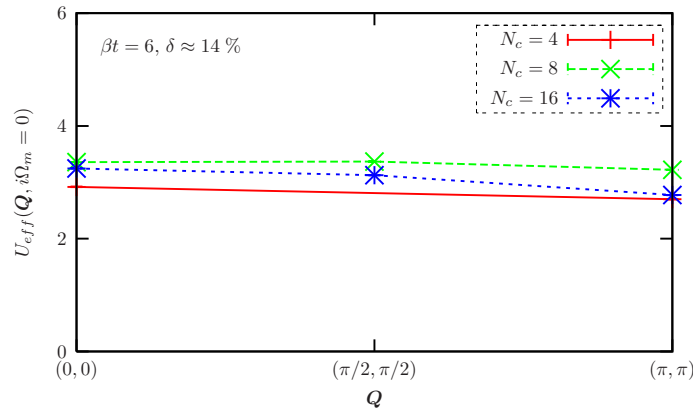
Figure 5.6 *Static $(i\Omega_m = 0)$ irreducible particle-hole interaction U_{eff} in the spin channel for different cluster momentum vectors and cluster sizes at $\delta \approx 14$ % dopings and at inverse temperature $\beta t = 6$ and $U = 8t$.*

(a)

(b)
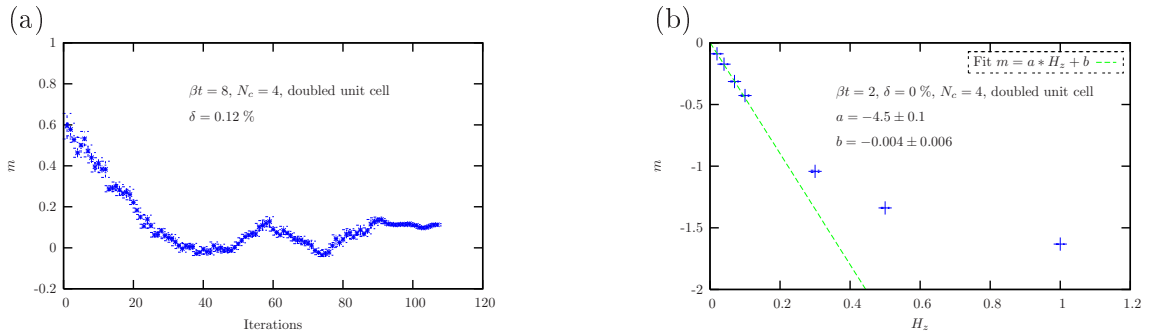
Figure 5.7 *Left: Evolution of the magnetisation as function of the iterations for a typical simulation which was performed close to the para- antiferromagnetic phase transition at $\beta t = 6$ and $\delta = 12$ % for an $N_c = 4$ cluster (doubled unit cell) Right: Exemplary presentation of the magnetisation in the presence of an external magnetic field H_z which couples to the spins of the systems.*

result as obtained from the SU(2) symmetry broken algorithm. This comparison provides information on the accuracy of our approximation to the two-particle irreducible vertex (see Eq. (5.13)).

By using the SU(2) symmetry breaking algorithm, the magnetic phase diagram for the one-band Hubbard model as a function of doping is shown in Fig. 5.8. The para-(antiferro)magnetic phase transition is indicated here by gray (blank) circles. At half-filling $T_N \simeq 0.4t$ and magnetism survives up to approximately 15 % hole doping. It is know that the convergence of the magnetisation during the self-consistent steps in the DCA approach is extremely poor near the phase transition and, therefore, we cannot estimate the transition temperature more precisely than shown in Fig. 5.8. A typical example is depicted in Fig. 5.7 (a) for a simulation which was performed close to the para - antiferromagnetic phase transition $\beta t = 6$ and $\delta = 12$ % for an $N_c = 4$ cluster (doubled unit cell). It shows the evolution of the magnetisation with respect to the number of iterations. The evolution of the magnetisation after approximately forty iterations steps indicates that the magnetisation has reached a self-consistent solution. The result would suggest a paramagnetic solution. If one keeps the simulation running and reduces the statistical error of the Monte Carlo calculation by the enhancement of the number of bins, one obtains a clear antiferromagnetic solution. For simulations which are much closer to the phase transition, the damping of the oscillation of the magnetisation is weaker and, therefore, no insight into the phase transition is possible. In our investigation, we tried to avoid this problem by introducing an external magnetic field H_z. For small values of H_z, we know from *linear response theory*, that the answer of the system is proportional to the external excitation. In Fig. 5.7 (b), the linear response of the magnetisation is apparent for an external magnetic field, which is smaller than 0.1. We chose for the simulation in Fig. 5.7 (b) a very high tem-
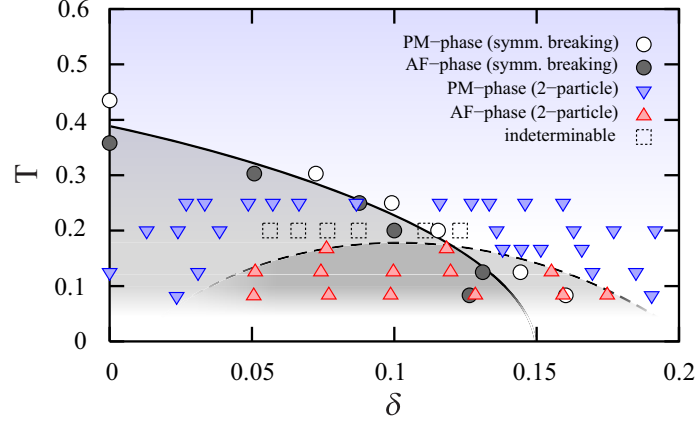
Figure 5.8 *Phase diagram for the one-band Hubbard model with $U = 8t$ with respect to different temperatures and fillings. The calculations are carried out on an $N_c = 8$ cluster. The red and gray (blue and blank) objects indicate the antiferromagnetic (paramagnetic) phase. Lines and shading of AF and PM regions are a guide to the eye. Details are in the text.*

perature in order to outline the principle idea. In the case of larger values of H_z, we can see a saturation effect. Obviously, one has to keep the external field weak enough in order to exploit the linear behaviour of the magnetisation. This means, that the above mentioned oscillations of the magnetisation can not be reduced in an efficient way. Furthermore, one has to perform at least three simulations with different external fields H_z in order to consult a least square fit, which enlarges the numerical effort. Hence, we discovered in our examination, that it is more effective, when one starts with a bad Monte Carlo statistic in
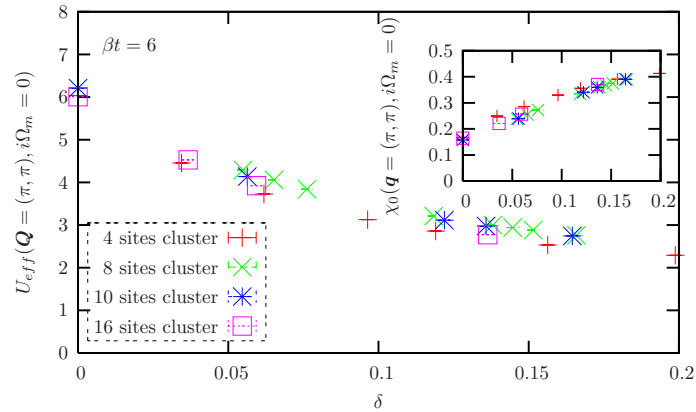
Figure 5.9 *Static irreducible particle-hole interaction U_{eff} for the cluster momentum vector $\boldsymbol{Q} = (\pi, \pi)$. The inset shows the static free lattice susceptibility χ_0 for the momentum vector $\boldsymbol{q} = (\pi, \pi)$. The bare Hubbard interaction strength is $U = 8t$.*

order to bring the system closer to the final solution without loss of computational time. After this start procedure, the precision of Monte Carlo calculations can be continuously increased. However, we want to point out, that the precision of the determination of the magnetisation is sufficient for comparison with our new approach. We again stress that the so determined magnetic phase diagram corresponds to the *exact* DCA result where no approximation — apart from coarse graining — is made on the particle-hole irreducible vertex.

In Fig. 5.8, the blue (red) triangles indicate the transition line for the para- to the anti-ferromagnetic solutions extracted from the divergent spin susceptibility (Eq. 5.25) within the paramagnetic calculation. A precise estimation of the Néel temperature requires very accurate results and boils down to finding the zeros of the denominator of Eq. 5.25. In Fig. (5.9), we consider the effective irreducible particle-hole interaction U_{eff} for the static case and for the cluster momentum $\boldsymbol{Q} = (\pi, \pi)$ relevant for the AF instability. As apparent, the irreducible particle-hole interaction becomes weaker with increasing doping. On the other hand, the susceptibility $\chi_0(\boldsymbol{q}, i\Omega_m = 0)$ grows with increasing doping. At a first glance both quantities U_{eff} and χ_0 (see Fig. (5.9)) smoothly vary as a function of doping. However, in the vicinity of the phase transition, signalised by the vanishing of the denominator in Eq. 5.25, the precise interplay between U_{eff} and χ_0 becomes delicately important and renders an accurate estimate of the Néel temperature difficult. Given the difficulty in determining precisely the Néel temperature, we obtain good agreement between both methods at $\delta \gtrsim 10$ %. Note that in those calculations the values of $\alpha \approx 0.86 - 0.97$ are required to satisfy the sum rule in Eq. (5.26). At smaller dopings, and in particular at half-band filling, the Néel temperature, as determined by the vanishing of the denominator in Eq. 5.25, underestimates the DCA result. Hence, in this limit, the $\underline{K}'$ and $\underline{K}''$ dependence of the irreducible vertex plays an important role in the determination of T_N and cannot be neglected.

Let us emphasise, that a good agreement between the Néel temperatures at $\delta \simeq 10$ % and above is a non-trivial achievement lending substantial support to the above new scheme for extracting two-particle Green functions.

5.2 Dynamical spin and charge structure factors

To further assess the validity of our approach, we compare it to *exact* auxiliary-field Blankenbecler, Scalapino, Sugar (BSS) QMC results (Ref. [23]). This method has a severe sign-problem especially in the vicinity of $\delta \simeq 10$ % and, hence, is restricted to high temperatures. The spin, $S(\boldsymbol{q}, \omega)$ and charge $C(\boldsymbol{q}, \omega)$ dynamical structure factors are given,

(a)

(b)

(c)

(d)
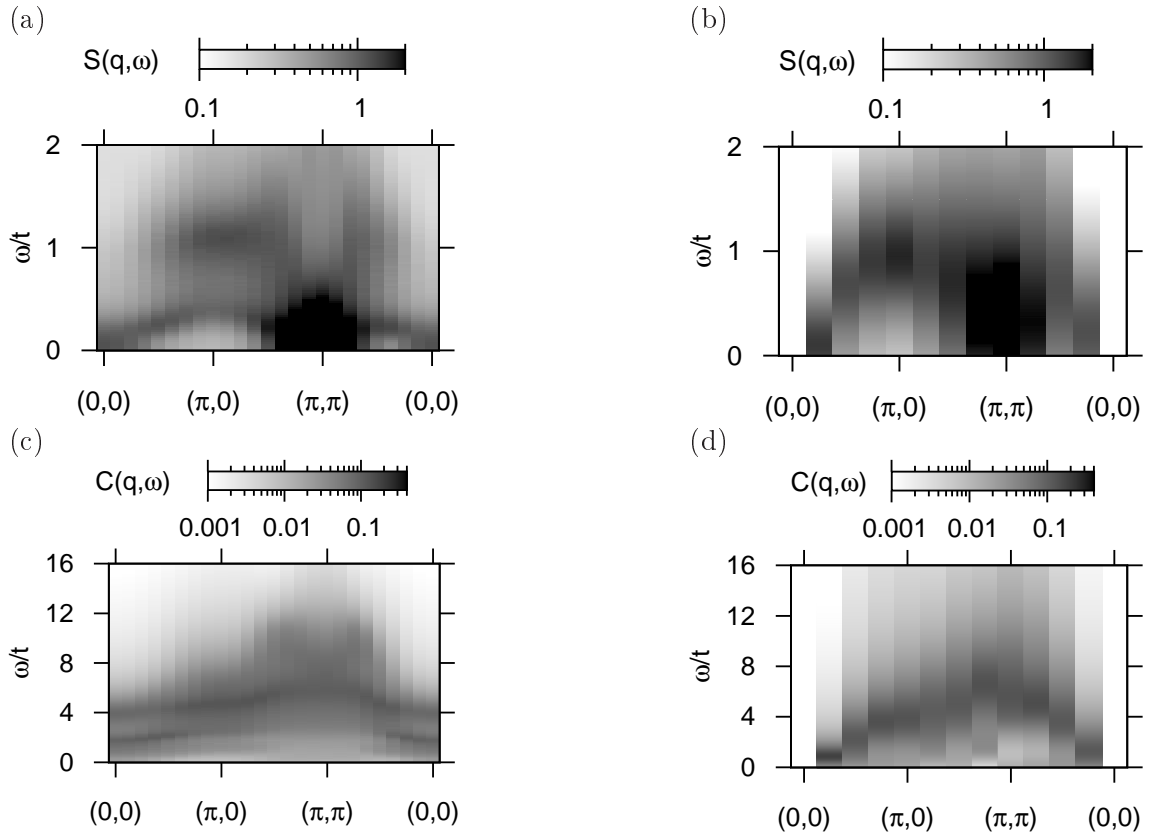
Figure 5.10 *DCA (left) versus auxiliary field QMC (BSS) (right) for the dynamical spin and charge structure factors of the Hubbard model at $U/t = 8$, $\delta \approx 14\,\%$ and $\beta t = 3$. The BSS data on the 8×8 lattice is essentially exact and acts as a benchmark for the DCA approach. The DCA calculations were carried out on an $N_c = 8$ cluster. Here we have used $\alpha = 0.98$ and $\alpha = 1.01$ to satisfy the sum rule in the spin and charge sectors, respectively.*
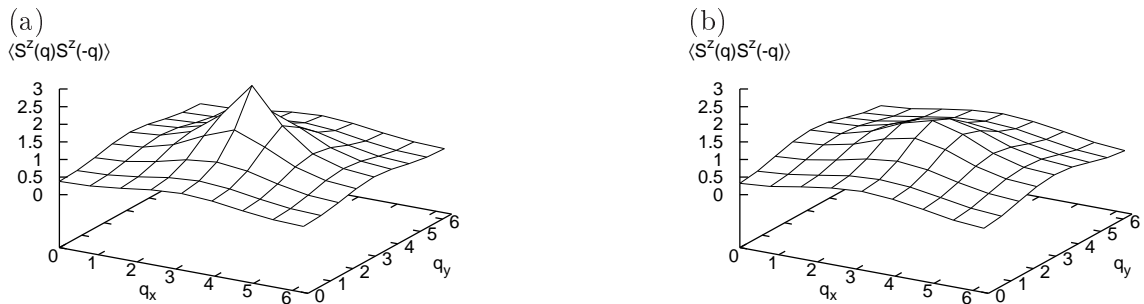
(a)

$\langle S^z(q)S^z(-q)\rangle$

(b)

$\langle S^z(q)S^z(-q)\rangle$

Figure 5.11 *DCA (a) versus BSS (b) static spin correlation function at $U/t = 8$, $\delta \approx 14\,\%$ and $\beta t = 3$ on an $N_c = 8$ cluster.*

respectively, by:

$$\langle S^z(\boldsymbol{q},\tau)S^z(-\boldsymbol{q},0)\rangle \;\; = \;\; \frac{1}{\pi}\int \mathrm{d}w\; e^{-\tau\omega}\, S(\boldsymbol{q},\omega) \tag{5.32}$$

$$\langle N(\boldsymbol{q},\tau)N(-\boldsymbol{q},0)\rangle \;\; = \;\; \frac{1}{\pi}\int \mathrm{d}w\; e^{-\tau\omega}\, C(\boldsymbol{q},\omega) \tag{5.33}$$

Here, $S^z(\boldsymbol{q}) = \frac{1}{\sqrt{L}}\sum_{\boldsymbol{j}} e^{i\boldsymbol{qj}}\,(n_{\boldsymbol{j},\uparrow} - n_{\boldsymbol{j},\downarrow})$ and $N(\boldsymbol{q}) = \frac{1}{\sqrt{L}}\sum_{\boldsymbol{j}} e^{i\boldsymbol{qj}}\,(n_{\boldsymbol{j},\uparrow} + n_{\boldsymbol{j},\downarrow})$. The left hand side of the above equations are obtained from the corresponding susceptibility as calculated from Eq. (5.24). Finally, a stochastic version of the Maximum Entropy method [25, 34] is used to extract the dynamical quantities.
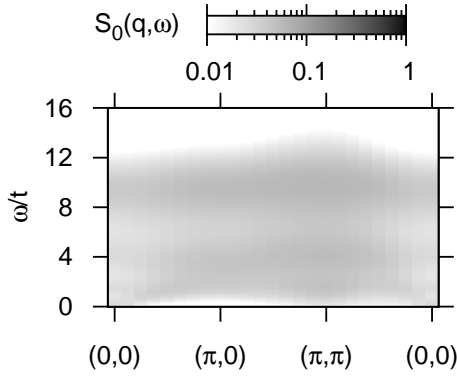
Figure 5.12 *Non-interacting dynamical two-particle lattice structure factor of the Hubbard model at $\beta t = 6$, $\delta \approx 14\,\%$ and $U/t = 8$.*

The comparison for the dynamical spin, $S(\boldsymbol{q},\omega)$, and charge, $C(\boldsymbol{q},\omega)$ dynamical structure factors is shown in Fig. 5.10 at $\beta t = 3$, $\delta \approx 14\,\%$ and $U/t = 8$. The BSS results correspond to simulations on an 8×8 lattice. Fig. 5.10 (b) depicts the BSS-QMC data in the spin sector. Due to short-range spin-spin correlations, remnants of the spin-density-wave are observable, displaying a characteristic energy-scale of $2J$, where J is the usual exchange coupling, i.e., $J = 4\frac{t^2}{U}$. The two-particle DCA calculations show spin excitations with the dominant weight concentrated, as expected and seen in the QMC data, around the AF wavevector (π,π). As apparent from the sum-rule,

$$\langle S^z(\boldsymbol{q})S^z(-\boldsymbol{q})\rangle = \frac{1}{\pi}\int \mathrm{d}\omega\; S(\boldsymbol{q},\omega) \tag{5.34}$$

(see Fig. 5.11 (a)), the DCA overestimates the weight at this wave vector but does very well away from $\boldsymbol{q} = (\pi,\pi)$. The dispersion in the two-particle data has again a higher energy

Fig. 5.13	a,b	c,d	e,f	g,h
α (spin)	0.99	0.92	0.93	0.97
α (charge)	0.98	1.00	1.00	1.00

Table 5.1 *Values of α for the spectra in Fig. 5.13.*

branch around $2J$, but it also shows features at J. Since the total spin is a conserved quantity, one expects a zero-energy excitation at $\boldsymbol{q} = (0,0)$. This is exactly reproduced in the 8×8 QMC-BSS data, and qualitatively in the DCA results.

The non-interacting dynamical two-particle lattice structure factor at $\beta t = 6$, $\delta \approx 14$ % and $U/t = 8$ is depicted in Fig. 5.12. The bubble shows a continuum of two-particle excitations and, i.e., no coherent excitation is visible. This means in other words, that a possible coherent spin excitation must be generated by the denominator of the expression in Eq. 5.25.

As a function of decreasing temperature, the DCA dynamical spin structure factor shows a more pronounced spin-wave spectrum. This is confirmed in Fig. 5.13 on the left hand side. Here, we fix the temperature to $\beta t = 6$ and keep the doping at $\delta \approx 14$ % but vary the cluster size. As apparent, for all considered cluster sizes ($N_c = 4, 8, 10, 16$) a spin wave feature is indeed observable: a peak maximum at $\boldsymbol{q} = (\pi, \pi)$ is present and the correct energy scale at $\boldsymbol{q} = (\pi, 0)$ of $2J$ is recovered. Additionally, we plot the spin dynamical structure factor calculated on the finite $N_c = 8$ cluster at $\beta t = 6$ and $\delta \approx 14$ % in Fig. 5.14 (a) where the discussed spin wave features are also existent. Unfortunately, a direct comparison of these results with auxiliary field quantum Monte Carlo calculations at lower temperature is not possible due to the severe minus-sign problem in the BSS calculation.

The investigation of the dynamical charge correlation function for the above parameters shows that the DCA calculations, which are depicted in Fig. 5.10 c), can also reproduce basic characteristics of the BSS charge excitation spectrum 5.10 d). Both calculations show excitations at $\omega \approx U$ which are set by the remnants of the Mott-Hubbard gap. Similar results are obtained at lower temperatures ($\beta t = 6$) on the right hand side of Fig. 5.13 for different cluster sizes ($N_c = 4, 8, 10, 16$). The corresponding values of α are listed in Tab. 5.1. These values confirm the overall correctness of our approach in that the corresponding sum rule for the charge response is accurately (exactly for $\alpha = 1$) fulfilled. For comparison, the dynamical cluster structure factor is presented for the $N_c = 8$ cluster at $\beta t = 6$ and $\delta \approx 14$ % in Fig. 5.14 (b). It exhibits also excitations at $\omega \approx U$. The bad momentum resolution is because of the small finite cluster geometry.

The doping dependence of the spin- and charge-response is examined in Fig. 5.15. Here, we restrict our calculations to the $N_c = 8$ cluster at $\beta t = 6$ and dopings between $\delta = 14$ % and $\delta = 32$ %. At $\delta = 14$ % (see Fig. 5.13) the dynamical spin structure factor displays a spin wave dispersion with energy scale J. That is $E^{SDW}(\pi, 0) = 2J$ with $J = 4\frac{t^2}{U}$. As the system is further doped ($\delta = 27$ %) the dispersion is no longer sharply peaked around $\boldsymbol{q} = (\pi, \pi)$. The excitations broaden up and change their energy scale from $J = 4\frac{t^2}{U}$ to an energy scale set by the non-interacting bandwidth. This effect becomes even more visible with higher dopings at $\delta = 32$ % (Fig. 5.15 (c)). Furthermore, the spectrum of the charge response shows a reduction of the weight of states at high energies ($\omega/t \approx 8$). This
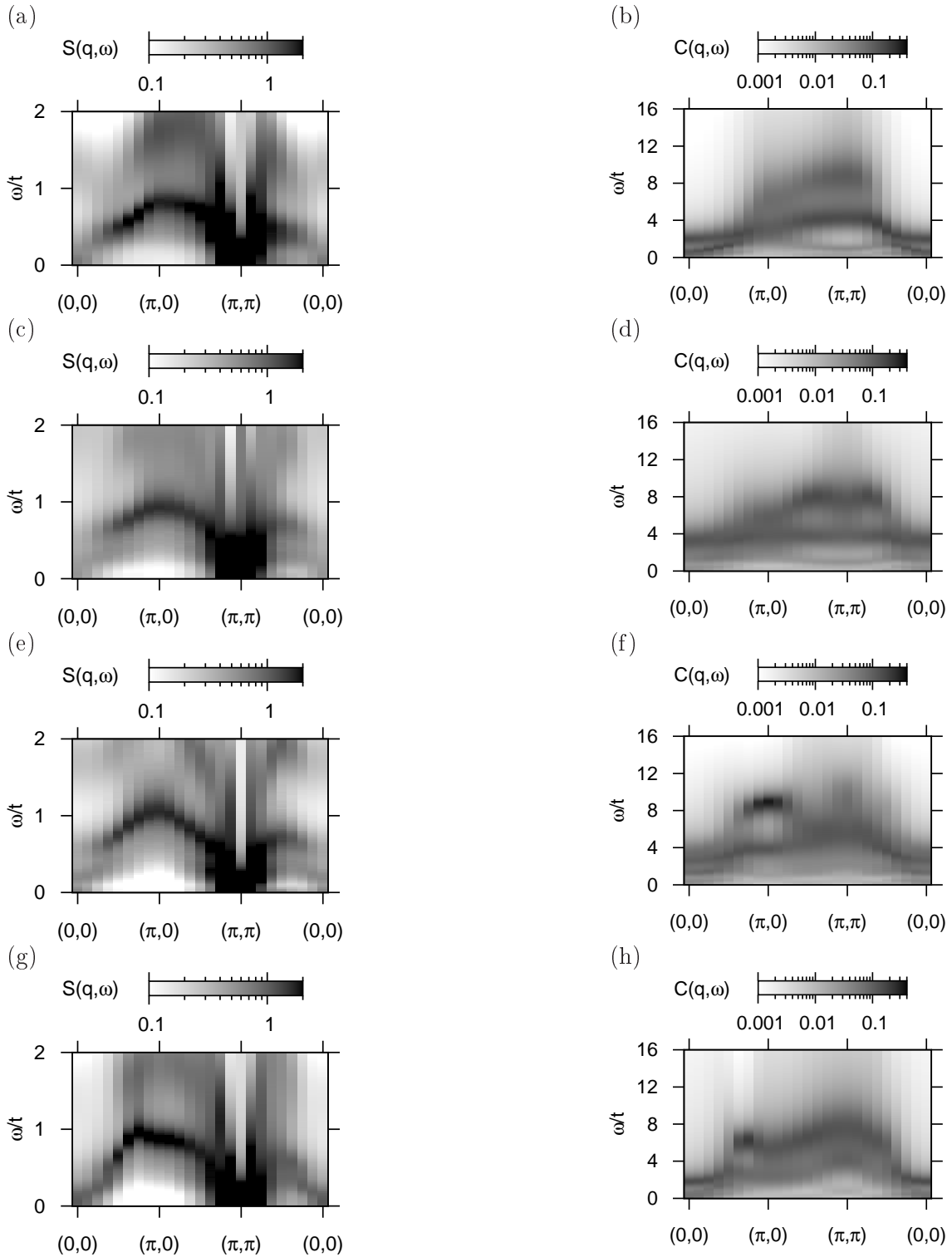
75

(a)

(b)

(c)

(d)

(e)

(f)

(g)

(h)

Figure 5.13 *Dynamical spin and charge structure factors of the Hubbard model at $\beta t = 6$, $\delta \approx 14 \%$ and $U/t = 8$. for different cluster sizes: (a-b): $N_c = 4$, (c-d): $N_c = 8$, (e-f): $N_c = 10$ and (g-h): $N_c = 16$.*
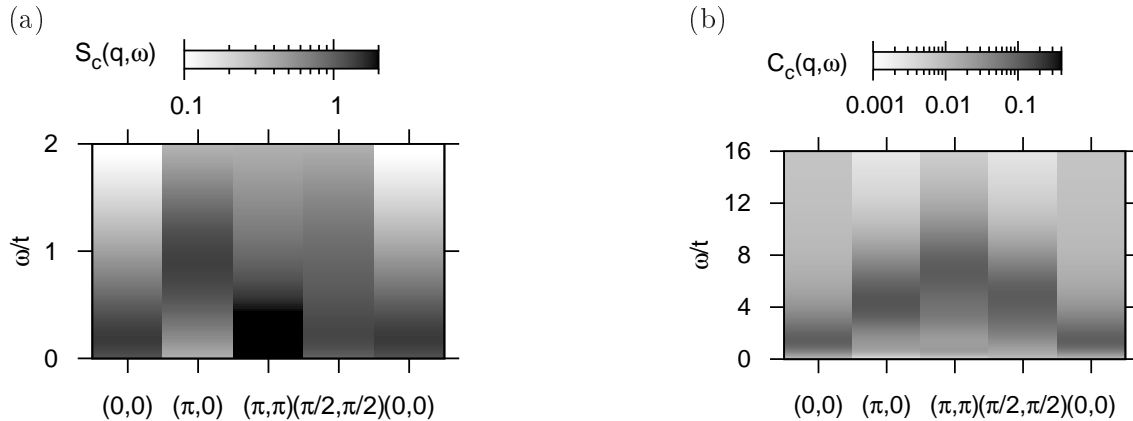
(a)

$S_c(q,\omega)$

(b)

$C_c(q,\omega)$

Figure 5.14 *Dynamical cluster spin and charge structure factors of the Hubbard model at $\beta t = 6$, $\delta \approx 14$ % and $U/t = 8$ on the $N_c = 8$ cluster.*

behaviour corresponds to the loss of weight of the upper Hubbard band with increasing doping. The corresponding equal time spin and charge correlation functions of Fig. 5.15 (c-d) are depicted in Fig. 5.16 (a-b). As in auxiliary-field QMC simulations [79], the equal time spin correlation function shows a set of peaks at $\boldsymbol{q} = (\pi \pm \epsilon, \pi)$ and $\boldsymbol{q} = (\pi, \pi \pm \epsilon)$. Here ϵ is proportional to the doping. By reducing the filling of the system, the set of peaks are almost vanished at $\delta = 27$ % (see Fig. 5.16). Below $\delta = 21$ % doping one can only observe a clear peak at the antiferromagnetic wave vector in the static spin-response spectrum which leads to the antiferromagnetic instability which is shown in Fig. 5.8. The static charge-response spectrum is depicted on the right hand site of Fig. 5.16. It shows an overall inconspicuous behaviour. At this point, the reader should keep in mind, that information at momentum vectors $\boldsymbol{k} = (0,0)$ is complicated to recover because this momentum vector corresponds to large length scales in real space which can exceed the size of the utilised cluster.

The overall trend of the doping dependence of the spin- and charge-responses is in good agreement with the previous findings of QMC simulations (see section 4.1 and [66, 23]): there it was shown that the spin-response has a characteristic energy scale $\omega \approx 2J$ and an SDW-like dispersion up to about $\delta \approx 10 - 15$ % doping, despite the fact that at these dopings the spin-spin correlations are very short-ranged (of order of the lattice parameter). A lot of the features of the two-particle spectra have direct influence on the single-particle spectral function and vice-versa. At optimal doping, $\delta = 14$ % the spectral function $A(\boldsymbol{q}, \omega)$ in Fig. 5.17 (a) shows three distinguishing features. An upper Hubbard band ($\omega/t \approx 8$) and a lower Hubbard band which splits in an incoherent background and a quasiparticle band of width set by the magnetic scale J (compare with Fig. 4.6). In agreement with earlier QMC data [66, 23], we view this narrow quasiparticle band as a fingerprint of a spin-polaron where the bare particle is dressed by spin fluctuations. The fact that the
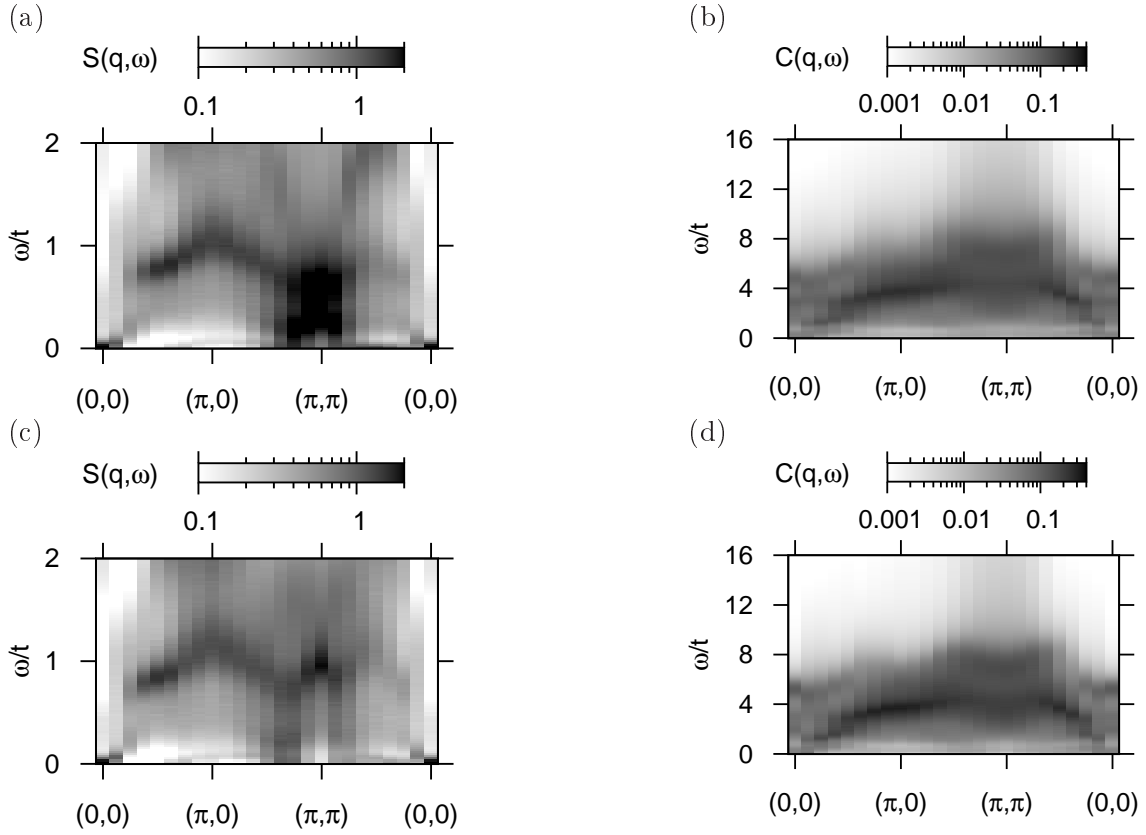
Figure 5.15 *Spin- and charge structure functions for different dopings: (a,b): 27 % and (c,d): 32 % The calculations are carried out on an $N_c = 8$ cluster at $\beta t = 6$. Here we have used $\alpha = 0.96$ (a), $\alpha = 1.00$ (b), $\alpha = 0.96$ (c) and $\alpha = 1.00$ (d).*

dynamical spin structure factor in Fig. 5.13 (c) shows a well defined magnon dispersion at this temperature and doping, $\delta = 14$ %, allows us to interpret the features centered around $\boldsymbol{q} = (0,0)$ and below the Fermi energy as backfolding or shadows of the quasiparticle band at $\boldsymbol{q} = (\pi,\pi)$. A comparison of the charge response spectrum in Fig. 5.13 (d) with the corresponding single-particle spectra in Fig. 5.17 (a) reveals that the response in the particle-hole channel at almost zero energy is caused by particle-hole excitations around the quasi-particle spin-polaron band close to the Fermi energy. The high energy excitations, mentioned above, are due to transitions from the quasi-particle band to the upper Hubbard band. As a function of doping, notable changes in the spectral function which are reflected in the two-particle properties are apparent. On one hand, the spectral weight in the upper Hubbard band is reduced. As mentioned previously, this reduction in high energy spectral weight is apparent in the dynamical charge structure factor. On the other hand, at higher dopings the magnetic fluctuations are suppressed. Consequently, the narrow band changes its bandwidth from the magnetic exchange energy J to the free
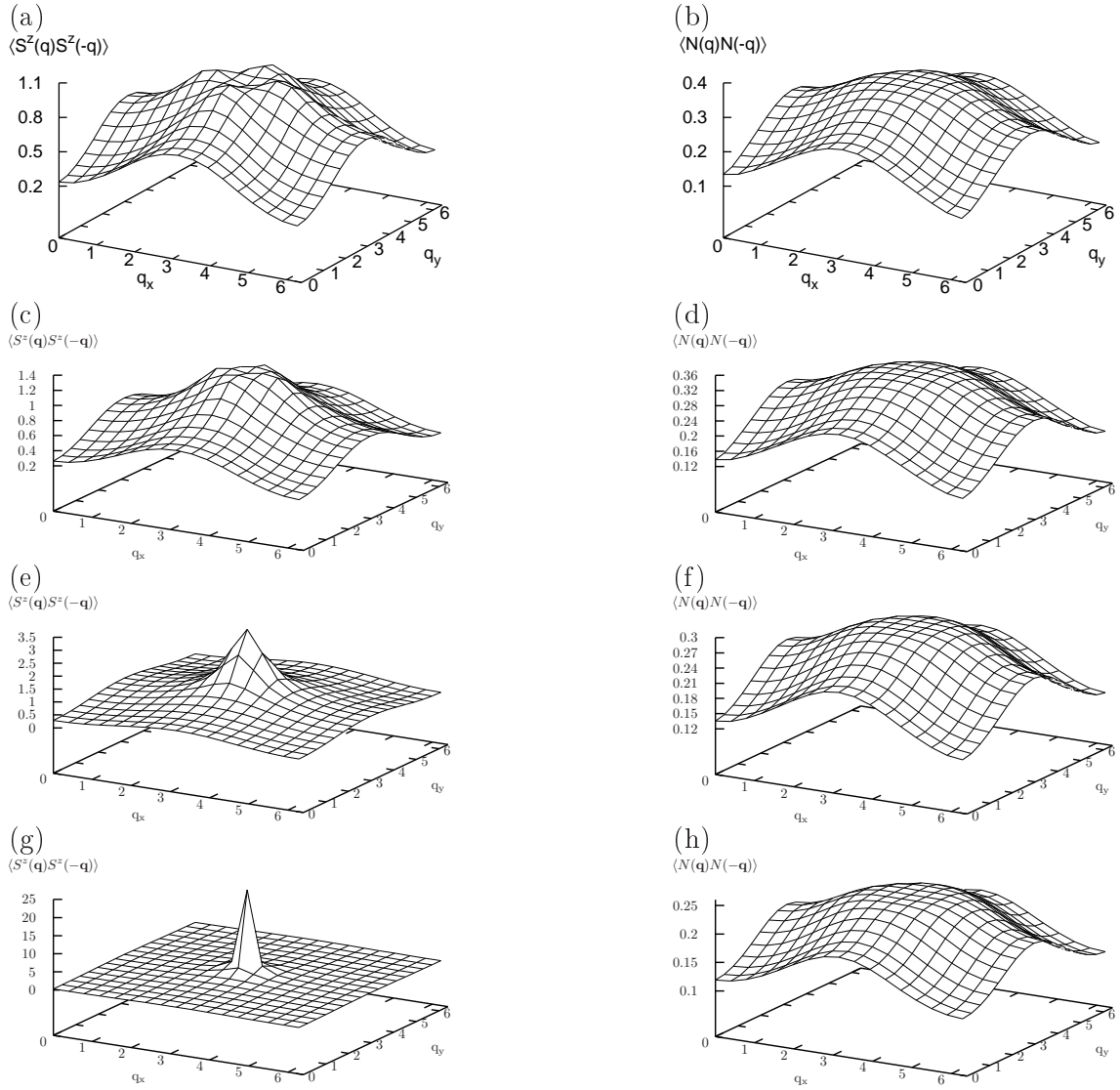
Figure 5.16 *Static spin (left) and charge (right) correlation functions at $U/t = 8$ and $\beta t = 6$ on an $N_c = 8$ cluster. The different dopings are $\delta \approx 32$ % (a-b), $\delta \approx 27$ % (c-d), $\delta \approx 21$ % (e-f), $\delta \approx 14$ % (g-h).*

bandwidth. This evolution is clearly apparent in Figs. 5.17 (b) and (c) and is in good agreement with previous BSS-QMC results (see section 4.1 and Ref. [23]).
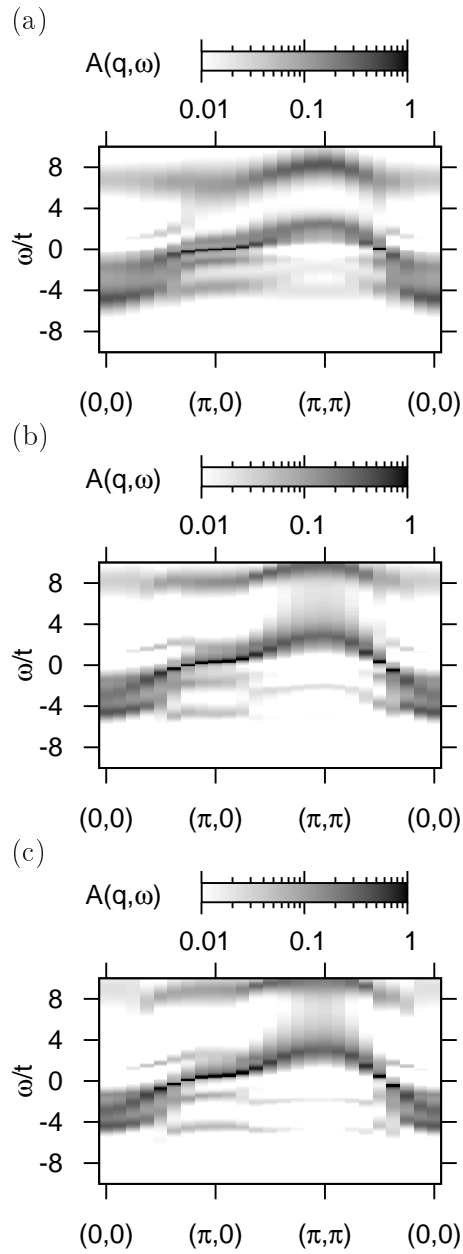
Figure 5.17 *Angle-resolved spectral functions $A(\boldsymbol{q}, \omega)$ for various hole dopings: a): 14 %, b): 27 % and c): 32 %. Calculations are carried out on an $N_c = 8$ cluster at $\beta t = 6$.*

d-wave super-conductivity in the Hubbard model

6

The physics of the high-temperature superconductors (HTSC) represents, on a microscopic level, a still unsolved mystery. Many experiments, i.e. angle resolved photoemission experiments [86], on doped superconducting cuprates reveal curious properties. A $d-$wave anisotropy of the superconducting state and pseudogap denote a significant differentiation to the conventional BCS superconductors. The pseudogap persists even in the normal state and is believed to cause the unusual non-Fermi liquid behaviour above the superconducting transition temperature. In the last years, several attempts have been made to explain the pairing mechanism of the Cooper pairs in the superconducting phase. Due to the existence of antiferromagnetic ordering in addition to a superconducting phase, one widely believes that short ranged antiferromagnetic correlations are responsible for the pairing of the electrons in the cuprates. In section 4, we have shown that the motion of a hole in an antiferromagnetic background leads to a string of broken antiferromagnetic bonds. In this picture, the magnetic frustration due to the broken bonds can be avoided by a second hole which travels with the first one through the lattice. This mechanism leads to an attractive potential for the electrons which can then form cooper pairs [87]. A second idea to describe superconductivity goes back to Anderson. He considered a spin-charge separated resonating valence bond (RVB) picture where spins pair into short-ranged singlets due to strong antiferromagnetic correlations [88, 89]. The elementary excitations of this states are spin 1/2 charge neutral fermions (spinons) and spin 0 bosons (holons) which recombine under the superconducting transition temperature to Cooper pairs [90].

The challenge of a detailed study of the HTSC is based on the complex interplay of the electrons on several energy scales. This requires a technique which incorporates the strong Coulomb interaction of the electrons but also enable calculations at sufficiently low temperatures in order to take the quantum nature of the spins into account. A state of the art technique in order to investigate superconductivity in systems of strongly correlated electrons, i.e. Hubbard model, is the Dynamical Cluster Approximation (DCA) (see section 2.1 and Refs. [8, 91, 92, 11]). In the following paragraph, we apply the DCA to the

Hubbard model and allow an instability to a superconducting phase.

6.1 DCA and superconducting phase

The technical implementation of the superconductivity within the DCA approximation is presented in section 2.9. Hereby, we accommodate the U(1) symmetry breaking by introducing additional anomalous Green functions. A particle-hole transformation (see Eq. (2.104)) transforms the anomalous Green functions into spin-flip Green functions. As we mentioned in section 4, one expects the order parameter of a possible superconducting phase to have d-wave symmetry. Therefore, we consider an $N_c = 4$ cluster which represents the smallest cluster to incorporate nearest neighbour interaction. A sketch of the coarse-grained cells and the d-wave order parameter is depicted in Fig. 6.1. Due to the symmetry of the pairing mechanism, we expect that the order parameter vanishes at the zone center and the point (π, π). A systematic study of the cluster size dependence of the
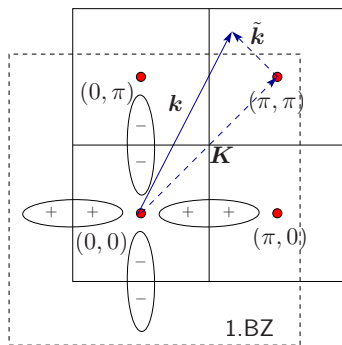
Figure 6.1 *Coarse-grained cells of the $N_c = 4$ cluster with the cluster momentum vectors (shown by red points) and a sketch of the $d - wave$ symmetry of the order parameter.*

superconductivity in the conventional Hubbard model was systematically performed by Jarrell et al. [11]. They showed that due to the non-locality of the d-wave superconducting order parameter, large finite size and geometry effects lead to inconclusive results. The calculations were carried out from the smallest cluster ($N_c = 4$) which can incorporate a $d-$wave superconducting instability to a $N_c = 26$ cluster. The superconducting transition temperature is dramatically dependent on the cluster size and geometry. In this respect, an important quantity is the (in)completeness of neighbouring shells of the clusters compared to the finite lattice [10]. Thus, the $N_c = 4$ cluster can contain only one Cooper pair and reveals the highest transition temperature because no superconducting phase fluctuations are included. On larger clusters (e.g. $N_c = 8$), there is room for one more Cooper pair on an adjacent plaquette. Therefore, two Cooper pairs interact with each other in such a way, that phase fluctuations can be replicated and hence overestimated. Jarrell et al. showed that the transition temperature of the $N_c = 8, 18$ clusters are negative and become slightly positive on larger clusters [11]. These considerations compel us to consider only the $N_c = 4$ cluster which exhibits the highest transition temperature. Calculations at low
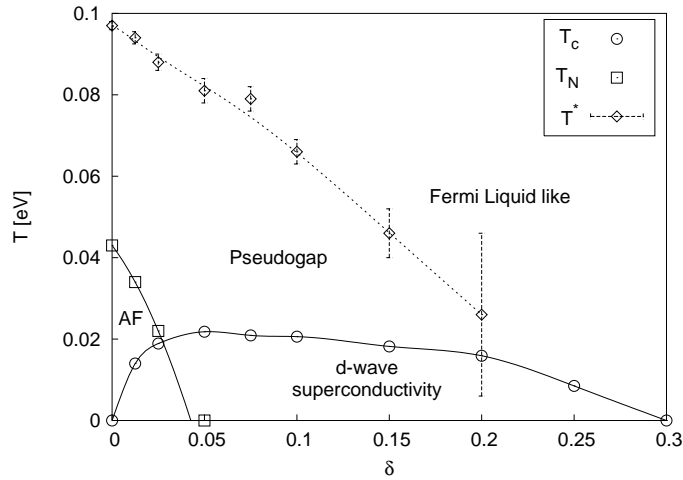
Figure 6.2 *Temperature-doping phase diagram of the 2D Hubbard model when the Coulomb repulsion is equal to the bandwidth $U = W = 8t$ for the DCA cluster size $N_c = 4$. The energy scale is given by $t = 0.25$ eV. Regions of antiferromagnetism, d-wave superconductivity and pseudogap behaviour are seen. The figure is taken from Jarrell et al. [8].*

temperatures would suffer from the severe minus-sign problem which would constrict a reliable investigation of the correlation physics in close proximity to the superconducting transition temperature.

Our first calculation serves as a test case. We consider the conventional Hubbard model with nearest neighbour hopping and a Coulomb interaction which is set to $U/t = 8$. First, we calculate the s- and d-wave order parameter within our Monte Carlo procedure with reference to the expressions in Eqs. (2.112) and (2.113) and compare it to a DCA calculation where the superconducting instability is estimated by the divergence of the pair-field susceptibility [8].

The DCA phase diagram of the Hubbard model in the strong coupling regime $U/t = 8$ is depicted in Fig. 6.2. The antiferromagnetic and superconducting phase transitions are determined by the divergence of the corresponding susceptibilities. In our calculation, we neglect a possible coexistence of the antiferromagnetic and the superconducting phase because this approach would require an 8×8 matrix representation of the Green functions in order to take both phases into account which would represent an immense computational effort. Our results for the d-wave order parameter as a function of temperature is shown in Fig. 6.3 for the 2D Hubbard model at $U/t = 8$ for three different dopings: $\delta = 5.2$ %, 15.5 % and 22.5 %. A comparison shows a good agreement of our results with the transition temperatures calculated by the divergence of the pair-field susceptibility in Fig. 6.2. The d-wave order parameters in Fig. 6.3 are calculated within the Monte Carlo procedure on
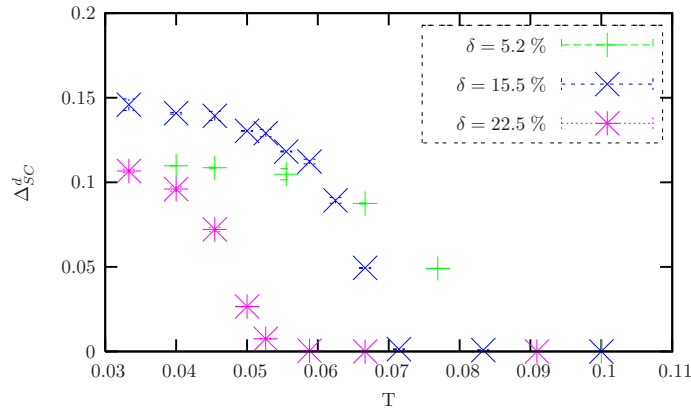
Figure 6.3 *d-wave order parameters Δ_{SC}^d of the 2D Hubbard model at $U/t = 8$ for different temperatures and different fillings: $\delta = 5.2$ %, 15.5 % and 22.5 %. The calculations are carried out on the $N_c = 4$ cluster. The next-nearest neighbour hopping amplitude is set to zero.*

the finite cluster and, therefore, their absolute value can slightly differ from the lattice quantity due to the non-local character of the order parameter. The calculation of the *s*-wave order parameter shows no indication of *s*-wave pairing in the repulsive Hubbard model. In the next step, we add a next-nearest hopping amplitude $t' = -0.3t$ to the above discussed conventional Hubbard model which brings the model closer to the physics of the high-temperature superconductors [93]:

$$H = -t \sum_{\langle ij \rangle \sigma} c_{i\sigma}^\dagger c_{j\sigma} - t' \sum_{\langle\langle ij \rangle\rangle \sigma} c_{i\sigma}^\dagger c_{j\sigma} + U \sum_i n_{i\uparrow} n_{i\downarrow} - \mu \sum_{i,\sigma} n_{i\sigma}, \qquad (6.1)$$

whereat the expressions $\langle ij \rangle$ and $\langle\langle ij \rangle\rangle$ indicate the summation over nearest and next-nearest neighbours, respectively, and μ represents the chemical potential. The resulting *d*-wave order parameters as a function of temperature are presented in Fig. 6.4 for three different hole dopings: $\delta = 4.7$ %, 7.0 % and 15.5 %. At the critical temperature, the estimation of the order parameter becomes pretty difficult because the convergence in the self-consistent steps in the DCA approach is extremely poor near the phase transition. For $\delta = 7.0$ %, we find a critical temperature T_c of $0.071t$ ($\beta t = 14$) $< T_c < 0.077t$ ($\beta t = 13$). The corresponding density of states (DOS) of the single-band Hubbard model with $t' = -0.3t$ at $U/t = 8$ is depicted in Fig. 6.5 for various temperatures. The red curve shows the DOS at a temperature $T \approx 2.5 T_c$. Clearly, no indications of a superconducting or pseudogap are visible in the spectrum. The line shape is almost flat. By decreasing the temperature to slightly above the critical superconducting temperature ($T = 0.083t$), a suppression of the local spectral function becomes visible which has to be interpreted as the occurrence of the pseudogap. The pseudogap changes at a temperature below T_c into a superconducting gap which becomes clearly visible at $T = 0.056t$ ($\beta t = 18$). The
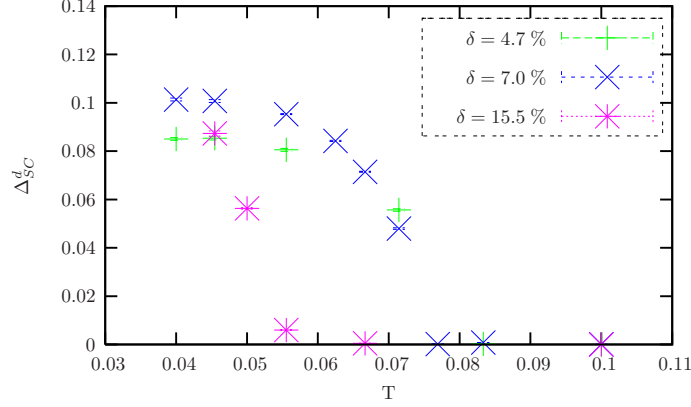
Figure 6.4 *d-wave order parameters Δ_{SC}^d of the 2D Hubbard model with nearest and next-nearest neighbour hopping amplitude ($t' = -0.3t$) at $U/t = 8$ for different temperatures and different hole dopings: $\delta = 4.7$ %, 7.0 % and 15.5 %. The calculations are carried out on the $N_c = 4$ cluster.*

evolution is accompanied by the formation of coherence peaks at $|\omega|/t \approx 0.3$ which are already known from the BCS theory.

In summary, our results concerning the superconducting transition temperature for $t' = 0$ are in good agreement with previous DCA calculations from Jarrell et al. [92] where they have investigated the 2D Hubbard model with $t' = 0$ in the strong coupling regime $U/t = 8$. In a second step, we have introduced a next-nearest neighbour hopping term $t' = -0.3t$ in our calculation. We discover that the overall evolution of the pseudo- and superconducting gap at $\omega = 0$ confirms previous DCA calculations performed by Jarrell et al. who could also demonstrate the creation of a coherence peak at small energies in agreement with our
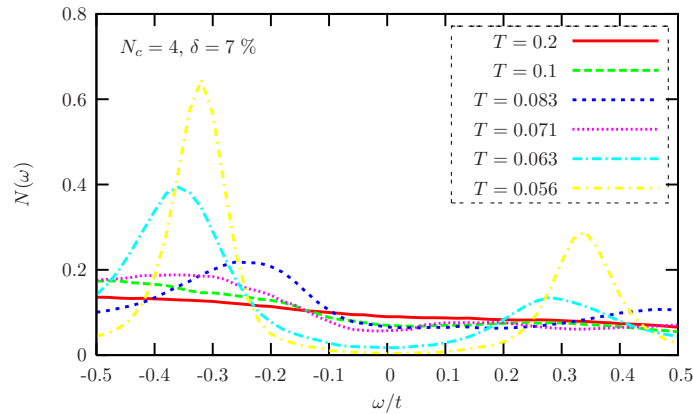
Figure 6.5 *Density of states of the 2D Hubbard model at $U/t = 8$ at different temperatures and at $\delta = 7$ % doping. The superconducting temperature lies in the interval $0.071t < T_c < 0.077t$.*

calculation [92].

6.2 Angle-resolved spectral function

To investigate the evolution of the superconducting gap in detail, we consider the momentum resolved one-particle spectral function. We remind the reader, that our calculations are carried out on the smallest cluster ($N_c = 4$) which can incorporate a non-local interaction of the electrons in two dimensions. Hence, we can only estimate the self-energy on four different momentum vectors which reveals a poor resolution in momentum space. Additionally, symmetry considerations reduce further the information content of the self-energy.

An interpolation scheme is used in order to translate the irreducible cluster quantities, i.e. the self-energy, to the infinite lattice. The idea is very similar to the approach which was presented by Eq. (5.27). Hereby, we consider the elements of the Nambu-matrix $\Sigma_c(\boldsymbol{K}, i\omega)$ where the diagonal elements describe the quasiparticle renormalisations and the off-diagonal elements contains the information about the $\boldsymbol{K}$- and frequency dependencies of the pairing state:

$$\Sigma_c(\boldsymbol{K}, i\omega_m) = \begin{pmatrix} \Sigma_{11}(\boldsymbol{K}, i\omega_m) & \Delta_{12}(\boldsymbol{K}, i\omega_m) \\ \Delta_{21}(\boldsymbol{K}, i\omega_m) & \Sigma_{22}(\boldsymbol{K}, i\omega_m) \end{pmatrix}. \tag{6.2}$$

In the following, we prescribe a series expansion (equivalent to Eq. (5.27)) in order to interpolate the self-energy. Hereby, we focus only on the off-diagonal elements of the self-energy:

$$\begin{aligned} -\Delta(\boldsymbol{k}, i\omega_m) &= \Delta_0(i\omega_m) + 2\Delta_1(i\omega_m)\left(\cos(k_x) + \cos(k_y)\right) \\ &+ 2\Delta_2(i\omega_m)\left(\cos(k_x) - \cos(k_y)\right) \\ &+ 2\Delta_3(i\omega_m)\left(\cos(k_x + k_y) + \cos(k_x - k_y)\right). \end{aligned} \tag{6.3}$$

For fixed Matsubara frequency $i\omega_m$ and for a given set of $\Delta(\boldsymbol{K}, i\omega_m)$ with cluster momenta $\boldsymbol{K}$, Eq. (6.3) represents a set of equations which uniquely determines $\Delta_i(i\omega_m)$, whereby $i = 0, \ldots, N_c - 1$. If the coefficients are determined, the self-energy can be estimated for every lattice momentum vector $\boldsymbol{k}$. The reader should note, that the momentum dependence of the self-energy is encoded in the pre-factors $\Delta_{i=0,\ldots,N_c-1}$ and the interpolation has to be performed for the real as well as for the imaginary part of Δ_{12}. The pre-factors $\Delta_{i=0,\ldots,N_c-1}$ are depicted in Fig. 6.6 for a simulation at $T = 0.056t$ ($\beta t = 18$) below T_c and at $\delta \approx 7\,\%$ hole doping. The results in Fig. 6.6 are restricted to the real part of $\Delta_{i=0,\ldots,N_c-1}$ which provides the most important contributions to $\Sigma_c(\boldsymbol{K}, i\omega_m)$. Evidently, the d-wave symmetry order parameter is one magnitude larger than the other contributions which are specified by Eq. (6.3) and, hence, confirms the d-wave symmetry of the pairing interaction. The
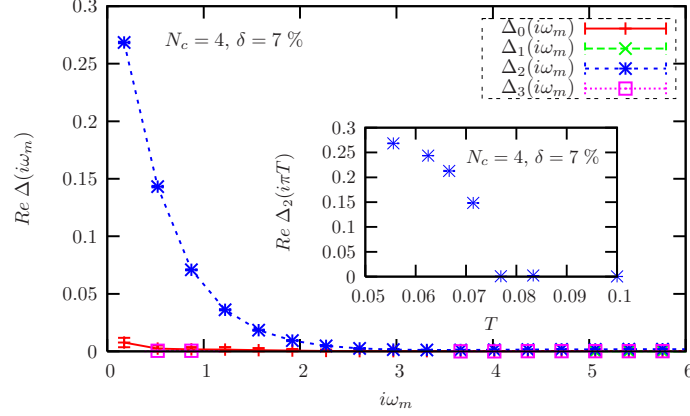
Figure 6.6 *Real part of the expansion coefficients $\Delta(i\Omega_m)$ which are defined by Eq. (6.3) of the Hubbard model at $U/t = 8$, $\delta = 7\ \%$, and $T = 0.056t$ ($\beta t = 18$). Inset: real part of the expansion coefficient $\Delta_2(i\Omega_m)$ at the Matsubara frequency $i\omega_m = i\pi T$ for the above parameters but at different temperatures. The calculations are carried out on the $N_c = 4$ cluster.*

frequency dependence of the d-wave order parameter is evident in Fig. (6.3) and it shows that, as opposed to the static mean-field BCS theory, retardation effects are taken into account. The inset of Fig. 6.6 exhibits the coefficient Δ_2 at the Matsubara frequency $i\omega_m = i\pi T$. The simulation is carried out at $\delta \approx 7\ \%$ hole doping. The coefficient Δ_2 is zero above the superconducting transition temperature and it monotonically increases below T_c. The temperature at which the phase transition takes place is in astonishingly
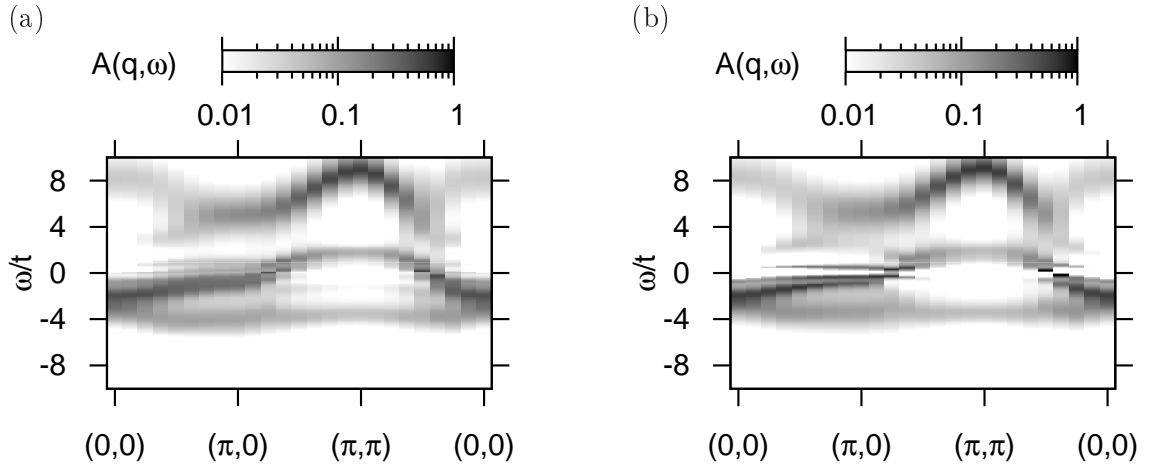
Figure 6.7 *Angle-resolved spectral function $A(\boldsymbol{q},\omega)$ for $\delta = 7\ \%$ hole doping. The calculations are carried out on the $N_c = 4$ cluster at $T = 0.1t$ ($\beta t = 10$) (a) and at $T = 0.056t$ ($\beta t = 18$) (b).*
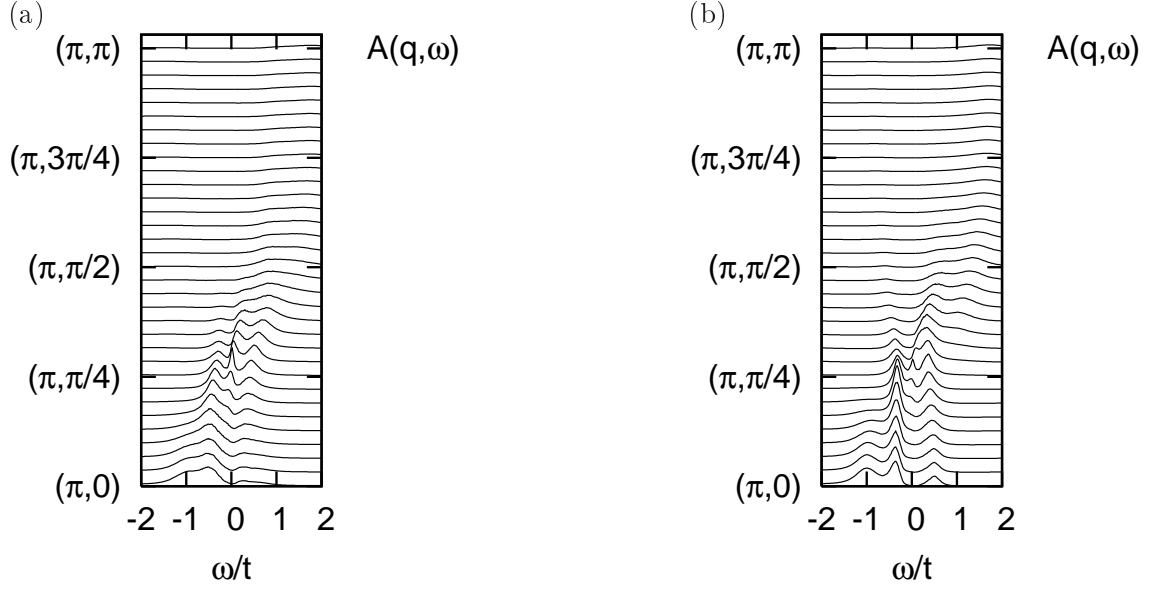
Figure 6.8 *Angle-resolved spectral function $A(\boldsymbol{q},\omega)$ for $\delta = 7$ % hole doping. The calculations are carried on the $N_c = 4$ cluster at $T = 0.071t$ $(\beta t = 14)$ (a) and at $T = 0.063t$ $(\beta t = 16)$ (b).*

good agreement with T_c which was estimated in Fig. 6.3. As mentioned previously, due to the non-local character of the d-wave order parameter, the absolute value of Δ_{SC}^d can deviate from the corresponding lattice quantity. On the other hand, Δ_2 is evaluated at the Matsubara frequency $i\omega_m = i\pi T$ which complicates a direct comparison with Δ_{SC}^d.

In the next paragraph we focus on the angle-resolved spectral function of the Hubbard model at $\delta = 7$ % hole doping on the $N_c = 4$ cluster. Fig. 6.7 (a) shows the one-particle spectrum at $T = 0.1t$ above the superconducting transition temperature where we can distinguish three different features. The spectrum is dominated by an upper Hubbard band $(\omega/t \approx 8)$ and a lower Hubbard band which are separated due to the Coulomb interaction. A coherent quasiparticle band around the Fermi surface describes the low energy excitations of the system. It crosses the Fermi surface around the momentum vectors $(\pi, \pi/4)$ and $(\pi/2, \pi/2)$. The quasiparticle band can be described by the dressing of a hole with a cloud of spin-excitations to allow for a coherent motion through an antiferromagnetic ordered background (see sections 4.1 and 5.2). By lowering the temperature below the critical superconducting temperature T_c the changes in the single-particle spectral function are accompanied by a formation of three peaks close to the Fermi energy around $(\pi, \pi/4)$. The center peak disappears with lowering temperature whereas the outer peaks become the coherence peaks which we have previously shown in the density of states. The angle-resolved spectral functions at $\delta = 7$ % hole doping and at $T = 0.071t$ and $T = 0.063t$ are depicted in Fig. 6.8 (a) and (b) respectively. The complete opening of the superconducting
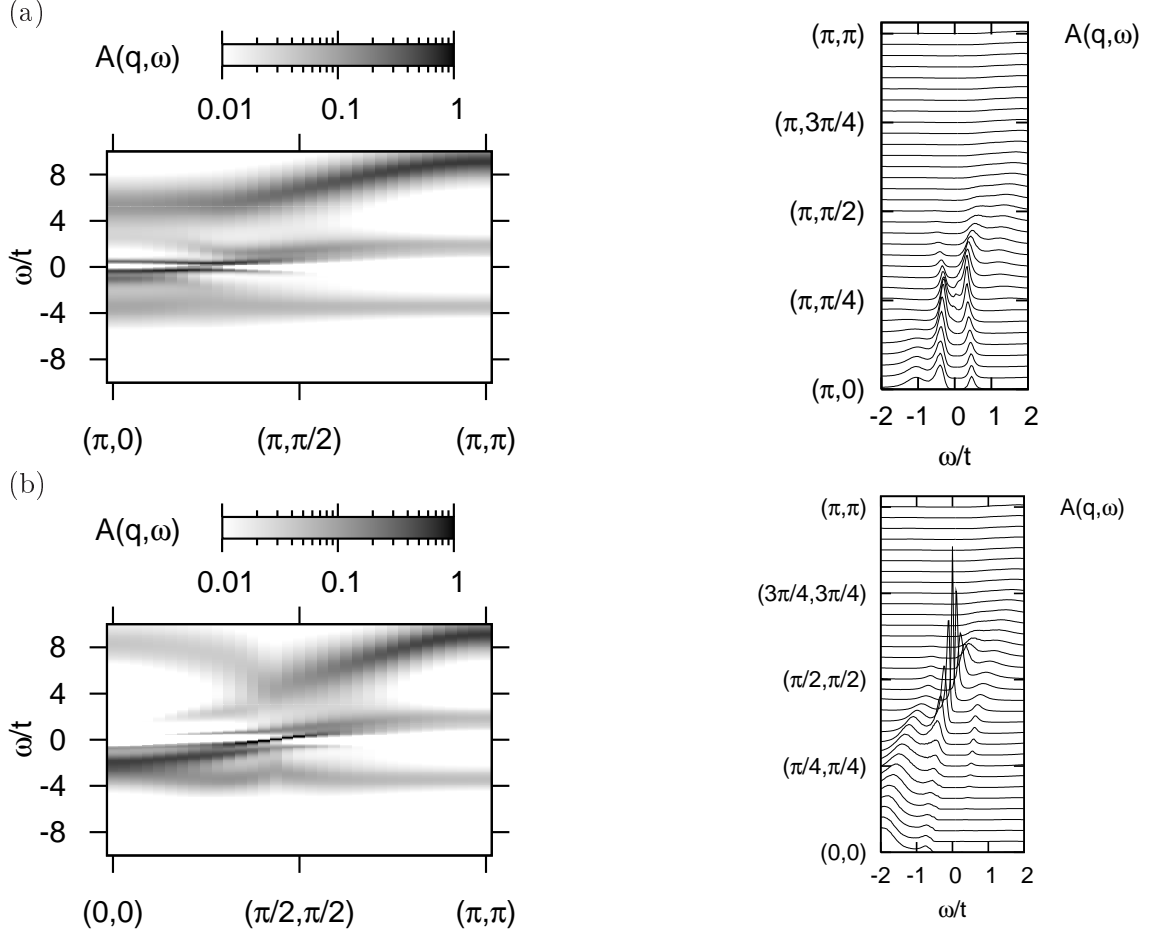
(a)

(b)

Figure 6.9 *Improved momentum resolution of the angle-resolved spectral function $A(\boldsymbol{q},\omega)$ of Fig. 6.7 (b) for different paths: $X \to M$ (a) and $\Gamma \to M$ (b). The calculations are carried out on the $N_c = 4$ cluster at $T = 0.056t$ ($\beta t = 18$) and for $\delta = 7\%$ hole doping.*

gap is first achieved at $T = 0.056t$ ($\beta t = 18$). The corresponding spectral function is shown in Fig. 6.7 (b) and Fig. 6.9 where we enhance the resolution in momentum space. The previously mentioned coherence peaks close to the superconducting gap slightly extend above und below the Fermi energy. The superconducting gap can be explained by an additional energy cost which is necessary to break up a Cooper pair in order to transfer an electron from close below to close above the Fermi energy.

We have already seen in Fig. 6.6 that the pairing interaction of the Hubbard model underlies a d-wave symmetry. The single-particle spectral functions in Fig. 6.9 (a) and (b) confirm the d-wave symmetry of the superconducting order parameter. The gap vanishes in nodal direction.

The suppression of spectral weight, even above the superconducting transition temperature,

was visible in the density of states in Fig. 6.5 which we have identified as the opening of a pseudogap. The investigation of the pseudogap is continued by a detailed study of
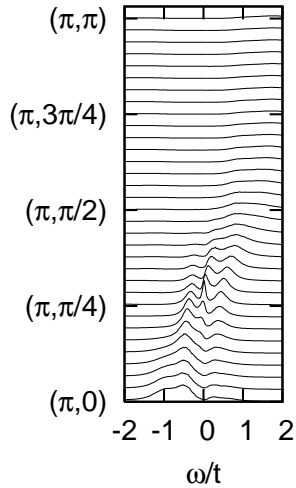
Figure 6.10 *Angle-resolved spectral function $A(\boldsymbol{q}, \omega)$ of the Hubbard model for $\delta = 7$ % hole doping. The calculation is carried out on the $N_c = 4$ cluster at $T = 0.083t$ $(\beta t = 12)$ slightly above the superconducting transition temperature T_c.*

the angle-resolved spectral function. Hereby, we plot $A(\boldsymbol{q}, \omega)$ of the Hubbard model for $\delta = 7$ % hole doping at $T = 0.083t$ $(\beta t = 12)$ in Fig. 6.10. The spectrum does not exhibit a precursor of a gap around the momentum vector $(\pi, \pi/4)$ where at lower temperatures the superconducting gap will open. Obviously, the information about the pseudogap must be encoded in the self-energy which is originally given only at the cluster momenta. The interpolation scheme (see Eq. (6.3)) cannot properly transfer such delicate information content, i.e. information about the pseudogap, to the intermediate lattice momenta.

Nevertheless, information about the opening of the superconducting gap and the formation of coherence bands close to the superconducting gap can be clearly reproduced in the single-particle spectrum at the intermediate lattice momenta and at sufficiently low temperature. In order to achieve a deeper insight into the physics of the pseudogap and superconducting state of the Hubbard model, one has to consider larger clusters. Firstly, calculations on larger systems repress the strong finite size effects and, secondly, the transfer of the irreducible quantities from the finite cluster to the infinite lattice becomes more independent from the interpolation scheme. The enhancement of the cluster size has the consequence, that the usual Hirsch-Fye quantum Monte Carlo cluster solver has to be replaced by a more efficient algorithm. Such a development is beyond the scope of this thesis and represents a great challenge for the next several years.

Summary

This thesis has been devoted to a study of a strongly correlated electron system. Using the Dynamical Cluster Approximation (DCA), we investigate the two-dimensional Hubbard model in the strong coupling regime $U = 8t$ (energy scale $t = 1$). In the DCA, the original lattice problem is mapped to a self-consistently embedded cluster of size $N_c = L_c \times L_c$. The correlations up to a range of $\xi \lesssim L_c$ are treated accurately, while the physics on longer lengthscales are described at the mean-field level. The cluster problem generated by the DCA is solved by the Hirsch-Fye quantum Monte Carlo technique.

The cluster irreducible self-energy, $\Sigma(\underline{K})$, and two-particle vertex, $\Gamma_{\underline{K}',\underline{K}''}$ serve as an approximation of their corresponding lattice quantities and they can be used to calculate the lattice single-particle and lattice two-particle correlations functions, respectively. The technical implementation is readily carried out for the single-particle properties. However, from a numerical point of view the calculation of the dynamical two-particle correlation functions, i.e. vertex function, within the DCA is much more involved.

The complexity of the cluster vertex function $\Gamma_{\underline{K}',\underline{K}''}$ can be reduced by averaging the $\underline{K}'$ and $\underline{K}''$ dependencies. Hence, we introduce an effective vertex function which depends only on the center of mass momentum und frequency, $\underline{Q} = (\boldsymbol{Q}, i\Omega_m)$:

$$\frac{1}{\beta L} U_{eff}(\underline{Q}) = \langle \Gamma_{\underline{K}',\underline{K}''}(\underline{Q}) \rangle.$$

With the effective vertex function $U_{eff}(\underline{Q})$ and the bubble $\chi_0(\underline{q})$, which is generated by the dressed Green functions,

momentum space
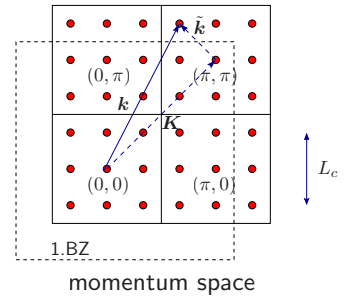
*DCA coarse-grained cells*
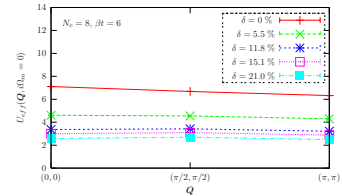
Effective particle-hole vertex

the lattice susceptibility reads:

$$\chi(\underline{q}) = \frac{\chi_0(\underline{q})}{1 - \alpha \cdot U_{eff}(\underline{q}) \cdot \chi_0(\underline{q})},$$

where α is estimated in a self-consistent manner and serves as a controlling parameter.

A comparison of our approach with a SU(2) symmetry broken DCA calculation on an $N_c = 8$ cluster serves as a test case. By evaluating the lattice spin susceptibility, a divergence would indicate a magnetic phase transition which can be compared with the Néel temperature, as obtained from the SU(2) symmetry broken algorithm. The resulting magnetic phase diagram from the SU(2) symmetry broken calculation corresponds to the *exact* DCA result where no approximation -apart from coarse graining- is made on the particle-hole irreducible vertex. At half-filling the phase diagram exhibits magnetism below $T \simeq 0.4t$ which persists up to approximately 15 % doping. A good agreement of both methods can be achieved at $\delta \gtrsim 10$ %. At smaller doping, the $\underline{K}'$ and $\underline{K}''$ play an important role in the determination of the Néel temperature and cannot be neglected. In a further test, we compare the spin $S(\boldsymbol{q}, \omega)$- and charge $C(\boldsymbol{q}, \omega)$-dynamical structure factors with *exact* auxiliary Blankenbecler-Scalapino-Sugar(BSS) QMC results at $\beta t = 3$, $\delta \approx 14$ %, and $U/t = 8$. The analytical continuation from the imaginary time axis to real frequencies is performed by a stochastic version of the maximum entropy method. The spectrum in the spin channel exhibits two branches at $\omega \approx J$ and $2J$, whereat $J = \frac{4t^2}{U}$ represents the usual exchange coupling. The DCA overestimates the spectral weight at $\boldsymbol{q} = (\pi, \pi)$ but does very well away from the AF wave vector. At lower temperatures $(\beta t = 6)$ a clear spin wave feature is indeed observable: a peak maximum at $\boldsymbol{q} = (\pi, \pi)$ is present and at $\boldsymbol{q} = (\pi, 0)$ the correct energy scale of $2J$ is recovered.
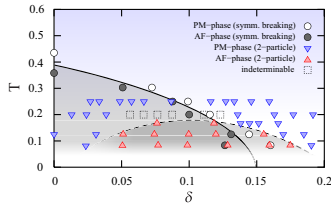
Magnetic phase diagram
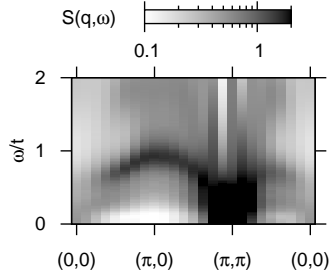
Spin dynamical structure factor
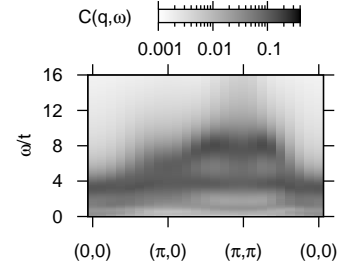
($\beta t = 6$ and $\delta \approx 14$ %)

The DCA dynamical charge correlation functions can reproduce the basic characteristics of the BSS charge excitation spectrum. Excitations at $\omega \approx U$ are set by the remnants of the Mott-Hubbard gap.

The investigation of the spin and charge responses at $\beta t = 6$ on the DCA $N_c = 8$ cluster exhibits a strong doping dependence. At $\delta = 27$ % the spin wave dispersion is no longer sharply peaked around $\boldsymbol{q} = (\pi, \pi)$. The excitations broaden up and change their energy scale from $J = \frac{4t^2}{U}$ to an energy scale set by the non-interacting bandwidth. The changes become more evident at higher dopings ($\delta = 32$ %). The charge response shows a reduction of spectral weight at high energies which can be explained by the loss of weight in the upper Hubbard band with increasing doping.

The single-particle spectrum ($\beta t = 6$, $\delta = 14$ %, and $N_c = 8$) exhibits three distinguishing features: an upper Hubbard band ($\omega/t \approx 8$) and a lower Hubbard band which represent the incoherent background. A quasiparticle band with energy J represents the low energy excitations of the system and results from a dressing of a hole with a cloud of spin-excitations to allow for a coherent motion through an antiferromagnetic ordered background. The occurrence of the spin-polaron is accompanied by the existence of the spin wave features in the spin response.

At higher dopings ($\delta \approx 32$ %) the upper Hubbard band loses spectral weight and the bandwidth of the quasiparticles changes from J to the free bandwidth and, therefore, corresponds to the changes in the two-particle spectra.

In the second part of the thesis, we study the superconductivity in the conventional Hubbard model ($t = 1$, $t' = -0.3t$, and $U/t = 8$) within the Dynamical Cluster Approximation. The anomalous Green functions are incorporated in terms of the Nambu representation. The diagonal elements of the Nambu matrix $\Sigma_c(\boldsymbol{K}, i\omega_m)$ represent the quasiparticle renormalisations and the off-diagonal parts contain information about the $\boldsymbol{K}$- and frequency dependence of the pairing state.
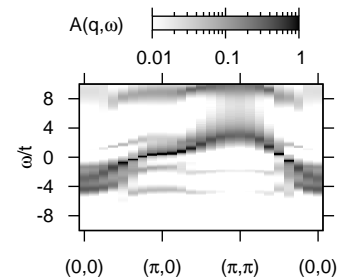

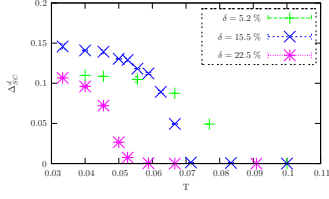*Charge dynamical structure factor ($\beta t = 6$ and $\delta \approx 14$ %)*
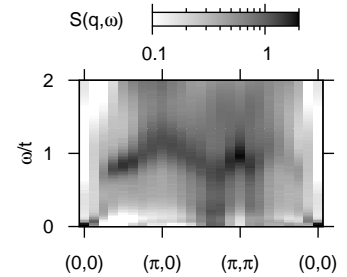
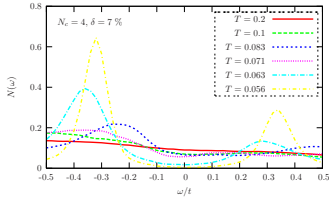*Spin dynamical structure factor ($\beta t = 6$ and $\delta \approx 32$ %)*
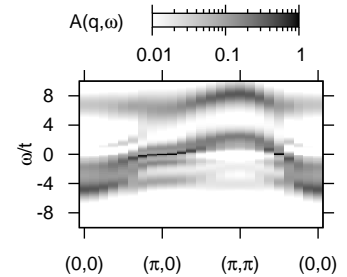
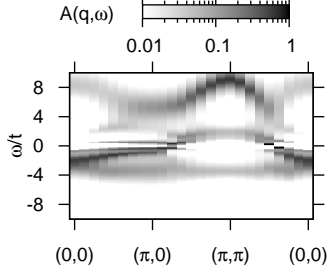*Spectral function ($\beta t = 6$ and $\delta \approx 14$ %)*

Spectral function ($\beta t = 6$ and $\delta \approx 32$ %)

d-wave order parameter (t′ = 0)

Density of states

Angle-resolved spectral function (βt = 18 and δ ≈ 7 %)

In a first test case, we compare the superconducting transition temperature, indicated by a non-vanishing order parameter, with a superconducting phase diagram of the conventional Hubbard model (for the test case: $t' = 0$), where the phase boundary is estimated by the divergence of the pair field susceptibility. Our calculations show a good agreement between both methods at three different dopings: $\delta = 5.2$ %, 15.5 %, and 22.5 %. The pairing state clearly exhibits a pure d-wave symmetry.

The density of states of the Hubbard model is studied for $\delta = 7$ % doping at different temperatures on the $N_c = 4$ cluster. An opening of a pseudogap is indicated by a slight suppression of spectral weight at $\omega = 0$ in the local spectral function above the superconducting transition temperature T_c. The formation of the superconducting gap below T_c is accompanied by the occurrence of coherence bands at $|\omega|/t \approx 0.3$.

A detailed study of the angle-resolved spectral function exhibits a delayed opening of the superconducting gap at $q \approx (\pi/4, \pi)$ while decreasing the temperature and shows no indication of a gap in nodal directions which confirms the d-wave symmetry of the superconducting order parameter. A precursor of the pseudogap at $q \approx (\pi/4, \pi)$ above the superconducting transition temperature cannot be resolved. The reason for this is given by the poor momentum resolution of the self-energy on the $N_c = 4$ DCA cluster. The interpolation scheme utilised for the self-energy cannot properly transfer the information about the pseudogap to the intermediate lattice momentum vectors.

Bibliography

[1] W. Metzner and D. Vollhardt, Phys. Rev. Lett. **62**, 324 (1989). 2

[2] E. Müller-Hartmann, Z. Phys. B **74**, 507 (1989). 2

[3] A. Georges, G. Kotliar, W. Krauth, and M. J. Rozenberg, Rev. Mod. Phys. **68**, 13 (1996). 2, 2

[4] P. Fazekas, B. Menge, and E. Müller-Hartmann, Z. Phys. B **42**, 187 (1995). 2

[5] J. Ward, Phys. Rev. **78**, 182 (1950). 2

[6] G. Baym, Phys. Rev. **127**, 1391 (1962). 2, 5

[7] M. H. Hettler, A. N. Tahvildar-Zadeh, M. Jarrell, T. Pruschke, and H. R. Krishnamurthy, Phys. Rev. B **58**, R7475 (1998). 2.1, 5

[8] T. Maier, M. Jarrell, T. Pruschke, and M. H. Hettler, Rev. Mod. Phys. **77**, 1027 (2005). 2.1, 5, 5, 6, 6.2, 6.1

[9] W. Nolting, *Grundkurs Theoretische Physik, 7. Viel-Teilchen-Theorie* (Vieweg, Braunschweig, 1997). 2.2

[10] D. Betts, H. Lin, and J. Flynn, Can. J. Phys. **77**, 353 (1999). 2.3, 5, 6.1

[11] T. Maier, M. Jarrell, T. Schulthess, P. Kent, and J. White, Phys. Rev. Lett. **95**, 237001 (2005). 2.3, 4, 5, 6, 6.1

[12] J. E. Hirsch and R. M. Fye, Phys. Rev. Lett. **56**, 2521 (1986). 2.7

[13] N. E. Bickers, D. J. Scalapino, and S. R. White, Phys. Rev. Lett. **62**, 961 (1989). 2.7

[14] N. E. Bickers, D. L. Cox, and J. W. Wilkins, Phys. Rev. B **36**, 2036 (1987). 2.7

[15] R. Blankenbecler, D. Scalapino, and R. Sugar, Phys. Rev. D **24**, 2278 (1981). 2.7

[16] S. R. White, D. J. Scalapino, R. L. Sugar, E. Y. Loh, J. E. Gubernatis, and R. T. Scalettar, Phys. Rev. B **40**, 506 (1989). 2.7

[17] M. Ferrero, L. D. Leo, P. Lecheminant, and M. Fabrizio, Journal of Physics: Condensed Matter **19**, 433201 (2007). 2.7.1, 2.7.1

[18] A. C. Hewson, *The Kondo Problem to Heavy Fermions* (Cambridge University Press, Cambridge, 1993). 2.7.1

[19] J. E. Hirsch, Phys. Rev. B **28**, 4059 (1983). 2.7.1

[20] H. Fehske, R. Schneider, and A. Weiße, *Computational Many-Particle Physics* (Springer, Heidelberg, 2008), p. 780. 2.7.2, 2.7.2

[21] L. C. Martin, Dynamic Mean Field Theory and a Projective Quantum Monte Carlo Method, Diploma thesis, Univ. Würzburg, (2004). 2.7.2

[22] F. F. Assaad and M. Imada, J. Phys. Soc. Jpn. **65**, 189 (1996). 2.7.2

[23] R. Preuss, W. Hanke, C. Gröber, and H. G. Evertz, Phys. Rev. Lett. **79**, 1122 (1997). 2.7.2, 4.1, 5, 5.2, 5.2, 5.2

[24] R. N. Silver, D. S. Sivia, and J. E. Gubernatis, Phys. Rev. B **41**, 2380 (1990). 2.7.2, 3.2

[25] K. S. D. Beach, 2004, arXiv:cond-mat/0403055. 2.7.2, 3.2, 3.2.1, 5.2

[26] F. F. Assaad, private communication. 2.8

[27] G. D. Mahan, *Many-Particle Physics* (Plenum, New York, 1990). 2.9

[28] H. Bruus and K. Flensberg, *Many-body Quantum Theory in Condensed Matter Physics* (Oxford University Press, Oxford, 2007). 2.9

[29] A. L. Fetter and J. D. Walecka, *Quantum Theory of Many-Particle Systems* (McGraw-Hill, New York, 1971). 2.9

[30] E. Freitag and R. Busam, *Funktionentheorie* (Springer, Heidelberg, 1991). 3.1

[31] J. E. Gubernatis, M. Jarrell, R. N. Silver, and D. S. Sivia, Phys. Rev. B **44**, 6011 (1991). 3.2

[32] S. F. Gull and J. Skilling, IEEE Proc **131**, 646 (1984). 3.2

[33] J. Skilling, *Maximum Entropy and Bayesian Methods* (Kluwer Academic, Dordrecht, 1989). 3.2, 3.2, 3.2

[34] A. Sandvik, Phys. Rev. B **57**, 10287 (1998). 3.2, 5.2

[35] S. R. White, Phys. Rev. B **44**, 4670 (1991). 3.2

[36] S. R. White, Phys. Rev. B **46**, 5678 (1992). 3.2

[37] M. Vekić and S. R. White, Phys. Rev. B **47**, 1160 (1993). 3.2

[38] N. Bulut, D. Scalapino, and S. White, Phys. Rev. B **50**, 7215 (1994). 3.2

[39] N. Bulut, D. J. Scalapino, and S. R. White, Phys. Rev. Lett. **73**, 748 (1994). 3.2

[40] N. Bulut, D. J. Scalapino, and S. R. White, Phys. Rev. Lett. **72**, 705 (1994). 3.2

[41] R. N. Silver, J. E. Gubernatis, D. S. Sivia, and M. Jarrell, Phys. Rev. Lett. **65**, 496 (1990). 3.2

[42] J. Deisz, M. Jarrell, and D. L. Cox, Phys. Rev. B **42**, 4869 (1990). 3.2

[43] M. Makivić and M. Jarrell, Phys. Rev. Lett. **68**, 1770 (1992). 3.2

[44] E. T. Jaynes, Probability Theory: The Logic of Science, 1995, available via ftp from bayes.wustl.edu, directory /pub/jaynes.book. 3.2

[45] F. F. Assaad, The Maximum Entropy Method, (unpublished). 3.2

[46] M. Jarrell and J. E. Gubernatis, Phys. Rep. **269**, 133 (1996). 3.2

[47] R. Preuss, Dynamik von Hubbard-Modellen, Dissertation, Univ. Würzburg, (1996). 3.2

[48] M. Imada and Y. Hatasugai, J. Phys. Soc. Jpn. **58**, 3752 (1989). 3.2.1

[49] E. Marinari, 1996, arXiv:cond-mat/9612010. 3.2.1

[50] J. Hubbard, Proc. R. Soc. London A **276**, 238 (1963). 4

[51] M. C. Gutzwiller, Phys. Rev. Lett. **10**, 159 (1963). 4

[52] J. Kanamori, Prog. Theor. Phys. (Kyoto) **30**, 275 (1963). 4, 5

[53] Y. Nagaoka, Phys. Rev. **147**, 392 (1966). 4

[54] J. G. Bednorz and K. A. Müller, Z. Phys. B **64**, 189 (1986). 4

[55] S. Martin, A. T. Fiory, R. M. Fleming, L. F. Schneemeyer, and J. V. Waszczak, Phys. Rev. Lett. **60**, 2194 (1988). 4

[56] F. C. Zhang and T. M. Rice, Phys. Rev. B **37**, 3759 (1988). 4.3, 4

[57] V. J. Emery, Phys. Rev. Lett. **58**, 2794 (1987). 4

[58] A. Macridin, M. Jarrell, T. Maier, and G. A. Sawatzky, Phys. Rev. B **71**, 134527 (2005). 4

[59] E. H. Lieb and F. Y. Wu, Phys. Rev. Lett. **20**, 1445 (1968). 4

[60] N. D. Mermin and H. Wagner, Phys. Rev. Lett. **17**, 1133 (1966). 4.1

[61] P. Horsch, W. H. Stephan, K. v. Szczepanski, M. Ziegler, and W. von der Linden, Physica C **162**, 783 (1989). 4.1

[62] K. J. von Szczepanski, P. Horsch, W. Stephan, and M. Ziegler, Phys. Rev. B **41**, 2017 (1990). 4.1

[63] E. Dagotto, R. Joynt, A. Moreo, S. Bacci, and E. Gagliano, Phys. Rev. B **41**, 9049 (1990). 4.1

[64] E. Dagotto, A. Nazarenko, and M. Boninsegni, Phys. Rev. Lett. **73**, 728 (1994). 4.1

[65] E. Dagotto, F. Ortolani, and D. Scalapino, Phys. Rev. B **46**, 3183 (1992). 4.1

[66] R. Preuss, W. Hanke, and W. von der Linden, Phys. Rev. Lett. **75**, 1344 (1995). 4.1, 5, 5.2, 5.2

[67] G. Martinez and P. Horsch, Phys. Rev. B **44**, 317 (1991). 4.1

[68] A. Ramšak and P. Horsch, Phys. Rev. B **48**, 10559 (1993). 4.1

[69] A. Ramšak and P. Horsch, Phys. Rev. B **57**, 4308 (1998). 4.1

[70] L. N. Bulaevskii, N. E. L., and D. I. Khomskii, Sov. Phys. JETP **27**, 638 (1967). 4.1

[71] R. Eder, Numerical Studies of strongly correlated electrons, Habilitationsschrift, Univ. Würzburg, (1998). 4.1, 4.4, 4.1

[72] J. R. Schrieffer, X.-G. Wen, and S.-C. Zhang, Phys. Rev. Lett. **60**, 944 (1988). 4.1

[73] J. R. Schrieffer, X. G. Wen, and S. C. Zhang, Phys. Rev. B **39**, 11663 (1989). 4.1, 4.1

[74] C. Gröber, Dynamic Porperties of Strongly Correlated Electron Systems, Dissertation, Univ. Würzburg, (1999). 4.1, 4.6, 4.7, 4.1

[75] A. Damascelli, Z. Hussain, and Z.-X. Shen, Rev. Mod. Phys. **75**, 473 (2003). 4.1

[76] P. A. Lee, N. Nagaosa, and X.-G. Wen, Reviews of Modern Physics **78**, 17 (2006). 4.1

[77] S. Hochkeppel, F. F. Assaad, and W. Hanke, Phys. Rev. B **77**, 205103 (2008). 4.1

[78] A. Damascelli, Z. Hussain, and Z.-X. Shen, Rev. Mod. Phys. **75**, 473 (2003). 5

[79] M. Imada, A. Fujimori, and Y. Tokura, Rev. Mod. Phys. **70**, 1039 (1998). 5, 5.2

[80] G. Baym and L. P. Kadanoff, Phys. Rev. **124**, 287 (1961). 5

[81] M. Jarrell, T. Maier, C. Huscroft, and S. Moukouri, Phys. Rev. B **64**, 195130 (2001). 5, 5

[82] N. Bulut, D. J. Scalapino, and S. R. White, Physica C **246**, 85 (1995). 5

[83] Y. Vilk and A.-M. Tremblay, J. de Physique **7**, 1309 (1997). 5

[84] Y. M. Vilk, L. Chen, and A.-M. S. Tremblay, Phys. Rev. B **49**, 13267 (1994). 5

[85] A. F. Veilleux, A.-M. Daré, L. Chen, Y. M. Vilk, and A.-M. S. Tremblay, Phys. Rev. B **52**, 16255 (1995). 5

[86] H. Ding and et al., Nature (London) **382**, 51 (1996). 6

[87] J. E. Hirsch, Science **295**, 2226 (2002). 6

[88] P. W. Anderson, Science **235**, 1196 (1987). 6

[89] P. W. Anderson, Science **268**, 1154 (1995). 6

[90] Z. Zou and P. W. Anderson, Phys. Rev. B **37**, 627 (1988). 6

[91] T. Maier, M. Jarrell, T. Pruschke, and J. Keller, Phys. Rev. Lett. **85**, 1524 (2000). 6

[92] T. A. Maier, M. Jarrell, A. Macridin, and C. Slezak, Phys. Rev. Lett. **92**, 027005 (2004). 6, 6.1

[93] O. K. Andersen, A. I. Liechtenstein, O. Jepsen, and F. Paulsen, J. Phys. Chem. Solids **56**, 1573 (1995). 6.1

Publications

- S. Hochkeppel and W. Hanke
  Understanding High-Temperature Superconductivity
  inSiDE - Innovatives Supercomputing in Deutschland, Vol. 4 No. 2 (2006)

- S. Hochkeppel, T. C. Lang, C. Brünger, F. F. Assaad and W. Hanke
  Quantum Monte Carlo Studies of Strongly Correlated Electron Systems
  in *High Performance Computing in Science and Engineering, Garching 2007*
  in press (Springer-Verlag, 2007)

- S. Hochkeppel, F. F. Assaad and W. Hanke
  A Dynamical Quantum Cluster Approach to Two-Particle Correlation Functions in the Hubbard Model
  Physical Review B **77**, 205103 (2008)

Lebenslauf

Persönliche Daten

Name   Stephan Hochkeppel

Geburtsdatum/-ort   13. September 1977 in Haan, NRW

Familienstand   ledig

Staatsangehörigkeit   deutsch

Schulbildung

08/1984 - 07/1988   **Grundschule**, GS Bollenberg in Haan

08/1988 - 06/1994   **Realschule**, Emil-Barth-Realschule in Haan

08/1994 - 06/1997   **Gymnasium**, Gewerbliche Schulen I in Wuppertal

Wehrdienst

07/1997 - 04/1998   Offiziersausbildung Teil I und Wehrdienst in Bayreuth
                         und Fürstenfeldbruck

Studium und Promotion

10/1998 - 12/2003   **Diplom-Studium der Physik** an der Universität Bonn

12/2003   **Diplomarbeit**:
                         Untersuchung zur Bestimmung der CP-Natur neutraler Higgs-
                         Bosonen im Prozess ttH bei ATLAS am LHC

seit 03/2004	**Promotion in Physik** an der Universität Würzburg
	Dissertation:
	One- and Two-Particle Correlation Functions in the Dynamical Quantum Cluster Approach

Anstellungen

10/2001 - 10/2003	**Studentische Hilfskraft** an der Universität Bonn
03/2004 - 06/2008	**Wissenschaftlicher Mitarbeiter** an der Universität Würzburg

Danksagung

Mein aufrichtiger Dank richtet sich an erster Stelle an Herrn Professor Dr. W. Hanke, der mir als Seiteneinsteiger die Möglichkeit an der Mitarbeit an einem attraktiven und interessanten Forschungsgebiet ermöglicht hat. Seine vielen Hilfestellungen in der physikalischen Interpretation meiner Ergebnisse trugen maßgeblich zum Fortschritt dieser Arbeit bei.

Mein ganz besonderer Dank gilt Herrn Professor Dr. F. F. Assaad für seine unermüdliche Unterstützung im Bereich der numerischen Umsetzung meiner Arbeit. Zahlreiche Diskussionen haben erheblich am Erfolg dieser Arbeit beigetragen.

Zusammenfassend möchte ich mich bei allen anderen Mitarbeitern am Lehrstuhl für Theoretische Physik I für die freundliche Zusammenarbeit bedanken. Namentlich möchte ich an dieser Stelle Prof. Dr. Michael Potthoff, Matthias Balzer, Sascha Brehm, Dr. Markus Aichhorn, Dr. Andrzej Fleszar, Christine Schmeisser, Bettina Spiegel und Judith Stahl hervorheben.

Besonderer Dank gilt Lee Martin für das sorgfältige Korrekturlesen dieser Arbeit.

Thomas Lang danke ich für die Hilfestellung bei der Illustration des Phasendiagramms in Fig. 5.8.

Desweiteren gilt mein Dank dem Leibniz Rechenzentrum in München für die großzügige Rechenzeitausstattung. Dem dortigen Support-Team danke ich für die kompetente Hilfe bei den aufgetretenen technischen Problemen.

Herzlich möchte ich mich auch bei meiner Freundin Christine Negrini und meiner Familie für die Liebe und aufgebrachte Unterstützung bedanken.

Versicherung an Eides statt

Hiermit versichere ich, Stephan Hochkeppel geboren am 13. September 1977 in Haan, an Eides statt, dass ich die vorliegende Arbeit eigenständig, d.h. insbesondere ohne Hilfe eines kommerziellen Promotionsberaters angefertigt habe. Es wurden keine anderen als in der Arbeit angegebenen Quellen und Hilfsmittel benutzt. Diese Arbeit liegt nicht in gleicher oder anderer Form in einem anderen Prüfungsfach vor.

Würzburg, am 2. September 2008

Stephan Hochkeppel